






Universitat Autònoma de Barcelona

ADVERTIMENT. L'accés als continguts d'aquesta tesi queda condicionat a l'acceptació de les condicions d'ús establertes per la següent llicència Creative Commons:  http://cat.creativecommons.org/?page_id=184

ADVERTENCIA. El acceso a los contenidos de esta tesis queda condicionado a la aceptación de las condiciones de uso establecidas por la siguiente licencia Creative Commons:  <http://es.creativecommons.org/blog/licencias/>

WARNING. The access to the contents of this doctoral thesis it is limited to the acceptance of the use conditions set by the following Creative Commons license:  <https://creativecommons.org/licenses/?lang=en>

UNIVERSITAT AUTÒNOMA DE BARCELONA

DOCTORAL THESIS

**Advanced laser deposition of
nanocarbon-based supercapacitor
electrodes**

Author:

Pablo GARCÍA LEBIÈRE

Supervisors:

Dr. Ángel PÉREZ DEL PINO

Dr. Enikő GYÖRGY

Tutor:

Dr. Aitor LOPEANDIA

*A thesis submitted in fulfilment of the requirements
for the degree of Doctor of Philosophy in Materials Science*

in the

Laser Processing Group

Institut de Ciència de Materials de Barcelona (ICMAB-CSIC)

UAB
Universitat Autònoma
de Barcelona

ICMAB  EXCELENCIA
SIVERO
OCHOA
INSTITUT DE CIÈNCIA DE MATERIALS DE BARCELONA

 **CSIC**
CONSEJO SUPERIOR DE INVESTIGACIONES CIENTÍFICAS

September, 2022

Declaration of Authorship

Dr. Ángel Pérez del Pino, researcher at CSIC, and **Dr. Enikő György**, researcher at CSIC, both at the Institut de Ciència de Materials de Barcelona and **Dr. Aitor Lopeandia**, associate professor at the Universitat Autònoma de Barcelona

CERTIFY

that **Pablo García Lebière**, carried out under their supervision the research work entitled “Advanced laser deposition of nanocarbon-based supercapacitor electrodes”. This work has been developed within a PhD program in Material Science at the department of physics of the Universitat Autònoma de Barcelona.

For that record, they sign the certificate

Dr. Ángel Pérez del Pino

Dr. Enikő György

Dr. Aitor Lopeandia

Pablo García Lebière

Bellaterra, September 2022

“El universo es la hostia.”

Dicho popular

UNIVERSITAT AUTÒNOMA DE BARCELONA

Abstract

Institut de Ciència de Materials de Barcelona (ICMAB-CSIC)

Doctor of Philosophy in Materials Science

Advanced laser deposition of nanocarbon-based supercapacitor electrodes

by Pablo GARCÍA LEBIÈRE

Supercapacitors or electrochemical capacitors are devices capable to store and release energy in a short time, being crucial for high power electric systems. The development of supercapacitors with higher capability to store energy is key for the advance to a sustainable electrified society. Thus, new high-performance electrode materials as well as innovative fabrication technologies need to be developed. The research of this thesis is focused on the synthesis of composite electrodes constituted by carbon-based materials decorated with metal oxide nanostructures. The fabrication was performed through the reactive inverse matrix assisted pulsed laser evaporation (RIMAPLE) technique, a single-step laser deposition technique with high potential for the synthesis of complex nanocomposites. Multicomponent electrodes based on reduced graphene oxide, multiwall carbon nanotubes and nickel oxides nanoparticles were produced. The nitrogen-doping of the carbon nanomaterials was accomplished by using different precursors, leading to an enhancement of the performance of the electrodes. Furthermore, the alternative use of different types of nanoparticles was tested. Electrodes composed of carbon-based materials decorated with cerium oxide nanostructures disclosed promising performance. Different synthesis paths were followed for their improvement, obtaining synergistic effects with the co-synthesis of manganese oxide nanostructures. Functional devices were also fabricated demonstrating the practical use of the synthesized electrodes.

Acknowledgements

First of all, I would like to express my deepest gratitude to my supervisors, Dr. Ángel Pérez del Pino and Dr. Enikő György for their invaluable advice, knowledge shared, continuous support and for given me the opportunity to complete this journey.

This thesis have been developed under the financial support of the Spanish Ministry of Science and Innovation with the grant BES-2017-081652 for the predoctoral contract for the formation of PhD within the project SEV-2015-0496-17-1. Additional funding were acquired from the project “Advanced fabrication of hybrid nanocarbon-based electrodes for supercapacitor applications” (ENE2017-89210-C2-1-R) and from the project “Advanced functionalization of carbon nanomaterials through intense laser radiation” (PID2020-116612RB-C31) both from the Spanish Ministry of Science and Innovation and coordinated by Dr. Enikő György and Dr. Ángel Pérez del Pino. I would like to thank the *Consejo Superior de Investigaciones Científicas* (CSIC) for the institutional support and the infrastructures.

I would like to express my sincere gratitude to Prof. Andrea Balducci from the Center for Energy and Environmental Chemistry (CEEC) in Jena, for giving me the opportunity to work in his group during a short three-months stay. I would like to thank all of them for the warm welcome and all the teachings and help given.

To Constantin Logofatu from the National Institute of Materials Physics, Măgurele, for the acquisition of the XPS measurements and his help in the analyses of the spectra.

Particular thanks should be given to all the *Institute de Ciència de Materials de Barcelona* (ICMAB-CSIC) scientific-technical services and to the *Institut Català de Nanociència i Nanotecnologia* (ICN2) electron microscopy unit for the SEM and TEM images, whom efficient work beats expectations. Special thanks to the people from administration at the ICMAB without whom I would not have been able to fulfil all paperwork.

I would also like to thank all the colleagues from the laser processing group, past and present. To all the bachelor, master, PhD students and doctors who helped me in many experiments, for all their help and teachings.

To all my colleagues from the ICMAB, from the ext. 269 “los apaños” to “Comemos?”. A group where all small departments could meet. For all the enjoying during all this years, with many lunch breaks outside, coffee breaks and funny moments.

I would also like to thank to my friends, for all the boardgaming afternoons, the barbecues, the scape rooms, the padel matches, the dinners, and all the moments to disconnect.

To my family, to my brother, to my father and my mother, for all the support given and for inspiring me and help me to get where I am.

To my cats, for their comfort and company. And last but not least, to Carls, for reading all this thesis searching for the most common word in each page, for helping and supporting me, for our travels, for our time together, but basically, for everything, thank you.

Contents

Declaration of Authorship	iii
Abstract	vii
Acknowledgements	ix
List of Publications	xxix
1 Introduction	1
1.1 Energy Storage	1
1.2 Supercapacitors	2
1.2.1 Electric Double Layer Capacitors	4
1.2.2 Pseudocapacitors	6
1.3 Supercapacitor Electrode Materials	8
1.3.1 Carbon-based materials	8
1.3.2 Conducting polymers	11
1.3.3 Metal-based materials	12
1.3.4 Composite materials	12
1.4 Fabrication methods	13
1.4.1 Laser fabrication for supercapacitors	15
1.4.2 Pulsed Laser Deposition	17
1.4.3 Matrix Assisted Pulsed Laser Evaporation	18
1.4.4 Reactive Inverse MAPLE	20
1.5 Outline of the thesis	21
2 Experimental Methods	23
2.1 Laser Deposition Technique	23

2.2	Morphological and Compositional Characterization	27
2.2.1	Scanning Electron Microscopy (SEM)	27
2.2.2	Transmission Electron Microscopy (TEM)	28
2.2.3	Small Angle X-ray Scattering (SAXS)	29
2.2.4	X-ray Photoelectron Spectroscopy (XPS)	32
2.2.5	Fourier-transform Infrared Spectroscopy (FTIR)	33
2.2.6	Raman Spectroscopy	33
2.3	Electrochemical Characterization	34
2.3.1	Cyclic Voltammetry (CV)	36
2.3.2	Galvanostatic Charge-Discharge (GCD)	37
2.3.3	Electrochemical Impedance Spectroscopy (EIS)	39
2.3.4	Step Potential Electrochemical Spectroscopy (SPECS)	40
3	Nanocarbon-based electrodes with NiO	43
3.1	Electrodes composed of rGO and NiO NPs	43
3.1.1	Morphological characterization	46
3.1.2	Electrochemical characterization	48
3.2	Nitrogen-doping of rGO and rGO-NiO electrodes	51
3.2.1	Morphological characterization	52
3.2.2	Compositional characterization	53
3.2.3	Electrochemical characterization	57
3.2.4	Device fabrication and performance study	62
3.3	Addition of MWCNT to the rGO-NiO composite	65
3.3.1	Morphological characterization	66
3.3.2	Compositional characterization	71
3.3.3	Electrochemical characterization	79
3.4	Conclusions	90
4	Nanocarbon-based electrodes with CeO₂	91
4.1	Electrodes composed of rGO, MWCNT and CeO _x	91
4.1.1	Morphological characterization	94
4.1.2	Compositional characterization	97
4.1.3	Electrochemical characterization	101

4.2	Increase of electrochemical performance through combination of metal oxides	106
4.2.1	Manganese acetate reaction with H ₂ O ₂ for target preparation	106
4.2.1.1	Morphological characterization	108
4.2.1.2	Compositional characterization	109
4.2.1.3	Electrochemical characterization	112
4.2.2	Electrodes prepared from GO platelets, MWCNT, CeO ₂ NPs and manganese acetate target solutions	115
4.2.2.1	Morphological characterization	116
4.2.2.2	Compositional characterization	118
4.2.2.3	Electrochemical characterization	120
4.2.2.4	Device fabrication and performance study	124
4.3	Organic electrolyte for energy increase	127
4.4	Conclusions	131
5	General Conclusions	133
A	COMSOL simulation and material properties	137
A.1	COMSOL simulation	137
A.2	Optical and thermophysical properties	141
B	Assignment of FTIR bands	145
	Bibliography	149

List of Figures

1.1	Ragone plot of different energy storage devices [4].	2
1.2	Physical models for the electric double layer at a positively charged surface: (a) The Helmholtz model, (b) the Gouy-Chapman model, and (c) the Stern model, combining both. .	5
1.3	(a) Schematic diagram of charge storage mechanism of electrical double-layer capacitors. (b) CV and (c) GCD electrochemical signatures of EDLCs.	7
1.4	(a) Schematic diagram of charge storage mechanism of pseudocapacitors. (b) CV and (c) GCD electrochemical signatures of pseudocapacitors.	7
1.5	3D model of (a) a single-wall carbon nanotube and (b) a graphene monolayer.	10
1.6	Molecular structure of (a) graphene oxide (GO) and (b) reduced graphene oxide (rGO).	11
1.7	Schematic diagram of a typical pulsed laser deposition (PLD) set-up.	18
2.1	Diagram of RIMAPLE deposition steps followed for the fabrication of electrodes.	24
2.2	RIMAPLE deposition vacuum chamber with laser path depicted for better interpretation.	25
2.3	RIMAPLE deposition equipment with laser path depicted for better interpretation.	26
2.4	(a) Schematic diagram of RIMAPLE deposition mechanisms and (b) experimental plume formed during deposition process.	26

2.5	Schematic diagram of the SAXS geometry.	30
2.6	Diagram of the electrochemical cell used for the analyses with aqueous electrolyte.	35
2.7	Example of voltage steps performed for a SPECS measurement and depiction of a current response of one of the steps.	41
3.1	(a) Simulated temperature of a NiO NP and carbon nanostructures during laser irradiation at $0.4 J cm^{-2}$ laser fluence and (b) temperature map of single NP at $5 ns$ from the start of the laser pulse.	44
3.2	Electrode layer deposited over PP film coated with sputtered Au/Cr.	46
3.3	XHRSEM images of (a) GO9% and (b) GO5% – NiO5% electrodes.	47
3.4	HRTEM images of electrode (a) GO9% and (b), (c) and (d) of GO5% – NiO5% in different regions.	47
3.5	CV of the electrodes (a) GO9% and (b) GO5% – NiO5% at $100 mV s^{-1}$ with surface capacitance contribution highlighted in blue; (c) CV curves of sample GO5% – NiO5% at sweep rate range of $10 mV s^{-1}$ – $150 mV s^{-1}$ (arrow indicates the increasing sweep rate); (d) areal capacitance <i>vs.</i> sweep rate of the fabricated electrodes.	49
3.6	(a) TEM image of GO-imi sample; (b) TEM and (c) corresponding HAADF-STEM images of the same location in the GO-NiO-imi sample.	52
3.7	(a) Wide XPS spectra of electrode GO-NiO-imi, (b) reduction degree and (c) nitrogen doping degree of all fabricated electrodes. In (b), open bars are directly obtained from measurements, whereas filled bars correspond to the calculated concentration by subtraction of NiO contribution.	55

3.8	Deconvolution of high resolution C 1 s XPS spectra of (a) raw GO and (b) GO-NiO-imi sample; (c) deconvoluted N 1 s spectrum of GO-NiO-imi sample; and (d) ratio of N 1 s components of the fabricated samples.	56
3.9	CV curves at sweep rate range $10\text{ mV s}^{-1} - 150\text{ mV s}^{-1}$ of sample (a) GO-imi and (b) GO-NiO-imi (arrow indicates the increasing sweep rate). CV of the electrodes (c) GO-imi and (d) GO-NiO-imi at 100 mV s^{-1} with surface capacitance contribution highlighted in blue.	58
3.10	(a) Areal capacitance <i>vs.</i> sweep rate of the fabricated electrodes with imidazole precursor comparing with previous GO5% and GO5% – NiO5% (open symbols). (b) Corresponding volumetric capacitance <i>vs.</i> sweep rate of the N-doped electrodes.	59
3.11	Galvanostatic charge–discharge data of (a) GO-imi and (b) GO-NiO-imi for different applied currents; (b) volumetric capacitance <i>vs.</i> applied current density of GO-imi and GO-NiO-imi.	61
3.12	(a) Nyquist plot of the EIS measurement (points) and simulated data from the equivalent circuit (lines) of fabricated electrodes containing imidazole precursor (the arrow indicates the direction of increasing frequency). Inset details the high frequency range. (b) Equivalent circuit for data fitting.	62

- 3.13 (a) Image of an assembled SC device. (b) CV curves at sweep rate range $10 - 150 \text{ mV s}^{-1}$ (arrow indicates the increasing sweep rate) and (c) GCD measurement of GO-NiO-imi SC device. (d) Volumetric capacitance *vs.* applied current of symmetric device GO-imi and GO-NiO-imi. (e) Capacitance retention and coulombic efficiency (inset) of both devices fabricated. (f) Ragone plot of the fabricated SC device compared with commercially available energy storage systems. Data for the lithium battery, $3.5 \text{ V} / 25 \text{ mF}$ supercapacitor (SC) and $6.3 \text{ V} / 220 \mu\text{F}$ electrolytic capacitor [171] and data for the $2.75 \text{ V} / 44 \text{ mF}$ activated carbon supercapacitor (AC-SC) [79]. 64
- 3.14 XHRSEM images of (a) GO-CNT-NiO-505, and (b) GO-CNT-NiO-515. 66
- 3.15 HAADF-STEM images of (a) GO flake and (b) MWCNT in sample GO-CNT-NiO-515. (c) HRTEM of sample GO-CNT-NiO-515; (d) zoomed-in area indicated in (c) with FFT of the area indicated by the rectangle. TEM images of (e) GO-CNT-NiO-515-M and (f) GO-CNT-NiO-515-A. Circles indicate the formation of nanometre-sized holes. 67
- 3.16 HRTEM image of GO-CNT-NiO-515-M and selected area filtered through FFT showing atomic planes of (1 1 1) NiO with arrows indicating dislocations. 68
- 3.17 (a) In-plane GISAXS intensity profiles of all the samples. The q -range below 0.16 nm^{-1} is the beamstop area. The origin of the peak at *ca.* 4 nm^{-1} is from kapton window. (b) Temporal evolution of correlation length at low ($< 3.14 \text{ nm}^{-1}$) and high ($> 3.14 \text{ nm}^{-1}$) q -ranges. 69
- 3.18 (a) Reduction degree and (b) nitrogen doping degree of fabricated electrodes. In (a), open bars are directly obtained from measurements, whereas filled bars correspond to the calculated concentration by subtraction of NiO contribution. 72

3.19	Deconvolution of high resolution (a) C 1 s and (b) N 1 s of GO-CNT-NiO-A sample. Areal percentage of the XPS deconvoluted components of the (c) C 1 s and (d) N 1 s peaks of the fabricated samples GO-CNT-NiO.	73
3.20	High resolution (a) O 1 s and (b) Ni 2 p spectra of the GO-CNT-NiO-515-U sample.	74
3.21	Characteristic FTIRM normalized spectra of raw GO, MW-CNT, urea and melamine powders as well as deposited samples GO-CNT-NiO-515, GO-CNT-NiO-515-A, GO-CNT-NiO-515-U and GO-CNT-NiO-515-M.	75
3.22	(a) Raman spectra acquired for representative films and (b) deconvolution of the Raman spectrum of film GO-CNT-NiO-515-A.	76
3.23	(a) Box plot of the measured D/G intensity ratios and (b) D/G intensity ratio <i>vs.</i> $FWHM(G)$ of representative samples, including linear fits.	77
3.24	(a) Calculated mean distance between defects (L_D) and corresponding density of defects (n_D). (b) Box plot of the D/D' intensity ratio for the deposited samples.	78
3.25	CV curves at sweep rate range $10\text{--}150\text{ mV s}^{-1}$ of (a) GO-CNT-NiO-515 and (b) GO-CNT-NiO-515-U (arrow indicates the increasing sweep rate). CV of (c) GO-CNT-NiO-515 and (d) GO-CNT-NiO-515-U electrodes at 100 mV s^{-1} with surface capacitance contribution highlighted in blue. Volumetric capacitance <i>vs.</i> sweep rate of (e) GO-CNT-NiO electrodes and (f) N-doped electrodes.	80
3.26	(a) Galvanostatic charge-discharge data of electrode GO-CNT-NiO-515-U and (b) volumetric capacitance <i>vs.</i> applied current density of GO-CNT-NiO samples.	83

3.27	(a) Nyquist plot of the EIS measurement (points) and simulated data from equivalent circuit (lines) of GO-CNT-NiO samples (the arrow indicates the direction of increasing frequency). Inset details the high frequency range. (b) Equivalent circuit for data fitting.	83
3.28	(a) Example of applied voltage steps and corresponding current evolution with acquisition time in SPECS experiment. (b) Fitting of a typical measured current curve (i_{meas}) considering the capacitive (i_{cap}), diffusional (i_{diff}) and residual (i_{res}) components, and $i_{Tot} = i_{cap} + i_{diff} + i_{res}$	85
3.29	Results obtained from fitting SPECS current curves for each measurement step: (a) C_C , (b) R_S , (c) B and (d) i_{res} parameters.	86
3.30	(a) Typical voltammogram generated from SPECS data, corresponding to GO-CNT-NiO-5151-U electrode at 86.7 mV s^{-1} sweep rate (i_{Tot}), together with the calculated current generated from the capacitive processes (i_{cap}). (b) Percentage of the capacitive charge for the analysed electrodes. (c) Typical linear fitting of $i_{Tot} v^{-1/2}$ vs. $v^{-1/2}$ for GO-CNT-NiO-5151-U and GO-CNT-NiO-5151-A electrodes. (d) Coefficient of determination (R^2) of the linear fitting as a function of voltage (up and down) for the GO-CNT-NiO-5151-U electrode. . . .	87
4.1	(a) Simulated temperature of CeO ₂ NPs and carbon nanostructures during laser irradiation and (b) temperature map (K) of an aggregate of 50 nm radius composed of 6 NPs surrounding a single one at the end of the laser pulse.	92
4.2	Electrode layer deposited over stainless steel substrate. . . .	94
4.3	XHRSEM images of (a) GO-Ce, (b) CNT-Ce and (c) GO-CNT-Ce-515 samples.	94
4.4	XHRSEM images of (a) GO-CNT-Ce-515, and (b) GO-CNT-Ce-525. Regions with agglomerated MWCNT are indicated.	95

4.5	XHRSEM images of (a) CNT-Ce electrode with magnified region on the right and (b) GO-Ce layer. HRTEM images of (c) CNT-Ce and (d) GO-CNT-Ce-515.	96
4.6	(a) Wide XPS spectra and fitting curves of high-resolution (b) C 1s and (c) O 1s spectra of the sample GO-CNT-Ce-515.	98
4.7	Ce $3d_{3/2}$ and Ce $3d_{5/2}$ high resolution XPS of GO-CNT-Ce-515 and CeO ₂ -raw NPs.	99
4.8	SR-FTIRM spectra of samples MWCNT-raw, GO-raw and GO-CNT-Ce 515.	100
4.9	CV of the samples (a) GO-Ce, (b) CNT-Ce and (c) GO-CNT-Ce-515 at 100 mV s^{-1} with surface capacitance contribution highlighted in blue; (d) percentage of surface contribution in capacitance of the fabricated electrodes at 100 mV s^{-1} ; (e) CV curves of the sample GO-CNT-Ce-515 at sweep rate range $10\text{ mV s}^{-1} - 150\text{ mV s}^{-1}$ (arrow indicates the increasing sweep rate); (f) volumetric capacitance <i>vs.</i> sweep rate of the fabricated electrodes.	102
4.10	(a) Galvanostatic charge–discharge data of GO- CNT-Ce-515 for different applied currents; (b) volumetric capacitance <i>vs.</i> applied current density of all the fabricated electrodes.	103
4.11	(a) Nyquist plot of the EIS measurement (points) and simulated data from the equivalent circuit (lines) of all the fabricated samples (the arrow indicates the direction of increasing frequency). Inset details the high frequency range; (b) equivalent circuit for data fitting.	104
4.12	(a) HRTEM image of the crystals obtained as product of reaction of manganese acetate with H ₂ O ₂ and (b) FFT of the selected region in (a).	107
4.13	XHRSEM images of GO-CNT-Ce-Mn-5152-H2O2 electrode with magnified region on the right.	108
4.14	HRTEM images of GO-CNT-Ce-Mn-5152-H2O2 electrode and FFT patterns of the marked regions.	109

4.15	(a) Wide XPS spectra; (b) C 1 s and (c) O 1 s high resolution XPS peaks of the GO-CNT-Ce-Mn-5152-H ₂ O ₂ electrode. . .	110
4.16	(a) Ce 3 d and (b) Mn 2 p high resolution XPS peaks of the GO-CNT-Ce-Mn-5152-H ₂ O ₂ electrode.	111
4.17	(a) CV curves of film GO-CNT-Ce-Mn-5155-H ₂ O ₂ at sweep rate range 10 – 150 $mV s^{-1}$ (the arrow indicates the increasing sweep rate); (b) volumetric capacitance <i>vs.</i> sweep rate of the electrodes GO-CNT-Ce-Mn-5152-H ₂ O ₂ and GO-CNT-Ce-Mn-5155-H ₂ O ₂ with sample GO-CNT-Ce-515 for comparison; (c) GCD data of GO-CNT-Ce-Mn-5155-H ₂ O ₂ ; and (d) Nyquist plot of EIS measurement (points) and simulated from equivalent circuit (lines) of the electrodes (the arrow indicates the direction of increasing frequency. Inset details the high frequency range).	113
4.18	(a) XHRSEM images of GO-CNT-Ce-Mn-5152 with magnified region on the right; (b) HAADF-STEM image of a nanotube in GO-CNT-Ce-Mn-5152 with EDX spectra of the depicted regions.	117
4.19	HRTEM image of GO-CNT-Ce-Mn-5155 with FFT and filtered lattices of the specified regions.	118
4.20	(a) C 1 s, (b) O 1 s, (c) Ce 3 d and (d) Mn 2 p high resolution XPS peaks of the GO-CNT-Ce-Mn-5152 electrode.	119
4.21	(a) CV curves of GO-CNT-Ce-Mn-5152 electrode at sweep rate range 10 – 150 $mV s^{-1}$ (the arrow indicates the increasing sweep rate); (b) CV curve at 100 $mV s^{-1}$ with highlighted surface capacitance contribution; (c) percentage of surface capacitance contribution at 100 $mV s^{-1}$; and (d) volumetric capacitance <i>vs.</i> sweep rate of the electrodes. (e) CV curves of GO-CNT-Ce-Mn-5155 electrode at sweep rate range 10 – 150 $mV s^{-1}$ with corresponding R^2 of the linear fit $i(v, V)/v^{1/2}$ <i>vs.</i> $v^{1/2}$ at each voltage value. The fitting at 0.3475V is used as an example of the non-linearity of this fitting.	121

- 4.22 (a) Volumetric capacitance *vs.* sweep rate of GO-CNT-Ce-Mn-5152 for diverse thicknesses and (b) volumetric capacitance *vs.* thickness for different sweep rates. 122
- 4.23 (a) GCD data of GO-CNT-Ce-Mn-5152; and (b) Nyquist plot from EIS measurements (points) and simulated from equivalent circuit (lines) of the electrodes (the arrow indicates the direction of increasing frequency. Inset details the high frequency range). 123
- 4.24 (a) CV curves at sweep rate range $10 - 150 \text{ mV s}^{-1}$ (arrow indicates the increasing sweep rate), (b) volumetric capacitance *vs.* sweep rate and (c) volumetric capacitance *vs.* applied current of a symmetric device GO-CNT-Ce-Mn-5152. (d) Ragone plot of the fabricated SC device compared with commercially available energy storage systems. Data for Li battery, $3.5 \text{ V}/25 \text{ mF}$ supercapacitor (SC) and $6.3 \text{ V}/220 \mu\text{F}$ electrolytic capacitor [171], data for the $2.75 \text{ V}/44 \text{ mF}$ activated carbon supercapacitor (AC-SC) [79] and GO-NiO-imi and GO-imi symmetric devices from Chapter 3. (e) Capacitance retention with charge-discharge zoomed regions (superior insets) and coulombic efficiency (inferior inset). 126
- 4.25 (a) CV curves of electrode at sweep rate range $5 \text{ mV s}^{-1} - 150 \text{ mV s}^{-1}$ (arrow indicates the increasing sweep rate) and (b) CV curve at 100 mV s^{-1} with highlighted surface capacitance contribution of GO-CNT-Ce-Mn-5152 with 1 M TEABF_4 dissolved in ACN. (c) Volumetric capacitance *vs.* sweep rate of GO-CNT-Ce-Mn-5152 electrode with aqueous and organic electrolyte. 128
- 4.26 GCD measurement of electrode GO-CNT-Ce-Mn-5152 with organic electrolyte. In left plot a zoomed region of shorter charge-discharge cycles is depicted for better visualization. 129

- 4.27 (a) GCD measurements and (b) calculated volumetric capacitance and coulombic efficiency of each cycle at different applied current densities of symmetric GO-CNT-Ce-Mn-5152 device with TEABF₄/ACN electrolyte. (c) Ragone plot of the fabricated GO-CNT-Ce-Mn-5152 device with TEABF₄/ACN electrolyte compared with commercially available energy storage systems and GO-NiO-imi, GO-imi and GO-CNT-Ce-Mn-5152 symmetric devices with aqueous electrolyte. (d) Capacitance and coulombic efficiency calculated during the float test of the device under study. 130
- A.1 Zoomed region of the 2D temperature map, in *K*, of single squared NiO NP of 50 *nm* lateral size (white square) at 5 ns from the start of the laser pulse. The discretization triangular elements where the PDE are solved is also included. . . . 139
- A.2 Skewness quality measure 2D map and corresponding histogram of (a) GO, (b) NiONP and (c) CeO₂ NPs aggregate simulations with COMSOL. 140

List of Tables

3.1	Relative concentration of precursors in the aqueous dispersions for RIMAPLE targets composed of GO and NiO NPs.	45
3.2	Relative concentration of GO, NiO NPs and imidazole precursors in the aqueous dispersions used in the RIMAPLE targets.	51
3.3	Fitting values for the elements of the equivalent circuit for electrodes with imidazole precursor.	62
3.4	Relative concentration of precursors in the aqueous dispersions for RIMAPLE targets composed of GO, MWCNT and NiO NPs.	65
3.5	Fitting values for the elements of the equivalent circuit for GO-CNT-NiO electrodes.	84
4.1	Relative concentration of precursors in the aqueous dispersions for RIMAPLE targets composed of GO, MWCNT and CeO ₂ NPs.	93
4.2	Fitting values for the elements of the equivalent circuit.	105
4.3	Fitting values for the elements of the equivalent circuit with the addition of manganese acetate and H ₂ O ₂	114
4.4	Relative concentration of precursors in the aqueous dispersions for RIMAPLE targets composed of of GO, MWCNT, CeO ₂ NPs and Mn(CH ₃ COO) ₂	116
4.5	Fitting values for the elements of the equivalent circuit with the addition of manganese acetate as metal organic precursor	124

A.1	Density (ρ), specific heat (C_p), thermal conductivity (k_{th}), reflectance (R) and absorption coefficient (α) of the materials used for simulation.	141
A.2	Temperature dependence of specific heat (C_p) of NiO used for simulation.	142
A.3	Temperature dependence of thermal conductivity (k_{th}) of NiO used for simulation.	142
A.4	Temperature dependence of thermophysical properties of CeO ₂ used for simulation.	143
B.1	Assignments of bands appearing in samples GO-CNT-NiO-515, GO-CNT-NiO-515-A, GO-CNT-NiO-515-U and GO-CNT-NiO-515-M.	145

List of Abbreviations

AC	Activated Carbon
ACN	Acetonitrile
BSE	Backscattered electrons
CP	Conducting Polymer
CPE	Constant Phase Element
CNT	Carbon Nanotubes
CV	Cyclic Voltammetry
CVD	Chemical Vapour Deposition
EC	Electrochemical Capacitor
EDL	Electric Double Layer
EDLC	Electric Double Layer Capacitors
EDX	Energy Dispersive X-ray Spectroscopy
EIS	Electrochemical Impedance Spectroscopy
ESR	Equivalent Series Resistance
FEM	Finite Element Method
FESEM	Field Emission Scanning Electron Microscopy
FTIR	Fourier-transform Infrared Spectroscopy
GCD	Galvanostatic Charge-Discharge
GISAXS	Grazing-incidence Small-angle X-ray Scattering
GO	Graphene Oxide
HAADF	High Angle Annular Dark-field
HRTEM	High Resolution Transmission Electron Microscopy
LIG	Laser-induced Graphene
MAPLE	Matrix Assisted Pulsed Laser Evaporation
MCT	Mercury Cadmium Telluride
MOF	Metal-Organic Frameworks
MWCNT	Multiwall Carbon Nanotubes
PANI	Polyaniline
PDE	Partial Differential Equations
PLD	Pulsed Laser Deposition
PMMA	Polymethylmethacrylate
PP	Polypropylene

PPy	Polypyrrole
PTFE	Polytetrafluoroethylen
RIMAPLE	Reactive Inverse MAPLE
RIR-MAPLE	Resonant Infrared MAPLE
rGO	Reduced Graphene Oxide
SAED	Selected-Area Electron Diffraction
SAXS	Small Angle X-ray Scattering
SC	Supercapacitor
SE	Secondary Electron
SEM	Scanning Electron Microscopy
SPECS	Step Potential Electrochemical Spectroscopy
SR-FTIRM	Synchrotron-based FTIR Microspectroscopy
STEM	Scanning Transmission Electron Microscopy
SWCNT	Single-wall Carbon Nanotubes
TEABF₄	Tetraethylammonium tetrafluoroborate
TEM	Transmission Electron Microscopy
TGS	Triglycine Sulfate
TMO	Transition Metal Oxide
XHRSEM	Extreme High-Resolution SEM
XPS	X-ray Photoelectron Spectroscopy

List of Publications

The work developed in this thesis led to the publication of the following articles:

1. Pérez del Pino, Á. et al. Fabrication of graphene-based electrochemical capacitors through reactive inverse matrix assisted pulsed laser evaporation. *Appl. Surf. Sci.* 484, 245–256 (2019).
2. Pérez Del Pino, Á. et al. Enhancement of the supercapacitive properties of laser deposited graphene-based electrodes through carbon nanotube loading and nitrogen doping. *Phys. Chem. Chem. Phys.* 21, 25175–25186 (2019).
3. García Lebière, P. et al. Laser fabrication of hybrid electrodes composed of nanocarbons mixed with cerium and manganese oxides for supercapacitive energy storage. *J. Mater. Chem. A* 9, 1192–1206 (2021).
4. Lebière, P. G. et al. Unravelling the origin of the capacitance in nanostructured nitrogen-doped carbon - NiO hybrid electrodes deposited with laser. *Ceram. Int.* 48, 15877–15888 (2022).

*To Carls,
so that you might hear me*

Chapter 1

Introduction

This chapter provides a comprehensive overview of the importance of the energy storage field and, in particular, supercapacitor devices. The energy storage mechanisms of supercapacitors as well as the typical materials used for the electrodes fabrication will be described. Following, different methods for the fabrication of electrodes will be introduced, focusing especially on laser processing techniques and their advantages. To conclude, an outline of the thesis will be presented.

1.1 Energy Storage

Nowadays, research strategies are moving towards the use of sustainable and renewable resources along with an increasing focus on energy production due to climate change and the decreasing use of fossil fuels, aiming to reduce pollution. Considering that renewable energy production does not always reach the population demands, energy storage systems play a major role [1]. As electricity is becoming the main power source of energy usage, the development of portable consumer electronics, medical devices, electric vehicles, smart electric grids, and the emerging of the Internet of Things has converted the storage of energy and its controlled release a crucial technology. The aforementioned technologies as well as the storage of energy harvested by wind power generators, heat sources or solar panels, requires improvements and diversification of the energy storage devices [2].

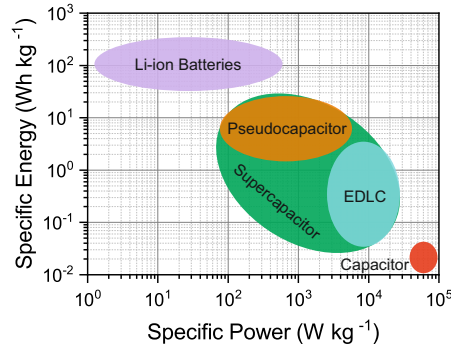


FIGURE 1.1: Ragone plot of different energy storage devices [4].

The performance of electrical energy storage systems determines their efficiency as well as their cost of operation for a specific application. Various types of storage systems are being investigated with the goal to reduce costs, ensure long term cyclability and to avoid a detrimental environmental impact. These storage systems can be classified as mechanical, such as pumped hydro storage, compressed air or flywheel energy storage; electrochemical, including batteries, capacitors and electromagnetic energy storage; chemical, as hydrogen storage or biofuel; and thermal storage systems, such as sensible heat or latent heat storage [3].

1.2 Supercapacitors

The Ragone plot showing specific energy *vs.* specific power among different electrochemical storage systems (Fig. 1.1) [4], clearly reveals that supercapacitors (SCs), also known as electrochemical capacitors (ECs) or ultracapacitors, are characterized by high specific power and relatively high specific energy. Additionally, SCs have attracted attention from both industry and academia due to their superior rate capability, fast and reversible use of energy, rapid charge-discharge rate, long life expectancy, wide range of operating temperatures, low maintenance cost, and environment-friendly nature [5–7]. Despite all the advantages, some challenges should be

faced to improve this technology, such as the low energy density compared with batteries or the high cost of the raw materials and manufacturing [5].

SCs are utilised for high power applications, including power buffer and power saving units, but are also of great importance for energy recovery applications [1]. SCs are employed in seaport cranes to load and unload container ships. Using energy that would otherwise be lost as heat during the repetitive movement is crucial for this application. Another significant purpose of the system is to allow size reduction in the power source. SCs are also assembled in heavy hybrid vehicles, which are ideal for trash and delivery trucks as well as city transit buses with stop-and-go driving. Additionally, it has been proposed that SCs could be applied to store off-peak electricity from the utility grid at night, when it is low cost and abundant, for usage during the day, when it may be more expensive and in short supply. SCs are also employed for power tools, namely cordless electric screwdrivers or power tubing cutters, capable of being charged for short times and deliver high power [8].

A SC is a device that stores energy at the interface between an electronic conductor and an electrolytic solution. The fundamental component of the device consists of two electrodes, an electrolyte, and a separator that acts as a physical barrier between the positive and negative electrodes while remaining permeable to ions in order to prevent electrical shorting [9]. The electrolyte provides pure ionic conductivity between the positive and negative electrodes, where the negative electrode, or negatrod, releases electrons and the positive electrode, or positrod, gains them. The electrolyte requires high electrochemical stability, wide voltage window, high ionic concentration and low solvated ionic radius, low resistivity, low viscosity, low volatility, low toxicity, low cost and high purity for best performance in the SC device. These electrolytes can be divided into aqueous, organic and ionic liquids. Aqueous electrolytes, for instance H_2SO_4 , KOH , Na_2SO_4 and NH_4Cl aqueous solutions, contribute with lower resistance and higher ionic concentration. However, these electrolytes are limited with a small

voltage window. Organic electrolytes can provide higher voltage window. These electrolytes consist on different salts, including tetraethylammonium tetrafluoroborate (TEABF₄) or tetraethylphosphonium tetrafluoroborat, dissolved in diverse solvents, for instance acetonitrile (ACN) and propylene carbonate. Finally, ionic liquids are composed of melted salts and are solvent-free adding low vapour pressure, high thermal and chemical stability, low flammability and wide electrochemical stability window as main properties [5].

SCs are essentially based on two different types of capacitive behaviour: i) one associated with the denominated Electric Double Layer (EDL) and ii) the other one associated with pseudocapacitance.

1.2.1 Electric Double Layer Capacitors

In 1957, Becker used a metallic current collector coated with high specific area carbon in a sulphuric acid solution to create the first electrochemical capacitor [10]. Electric double-layer Capacitors (EDLC) are electrochemical capacitors that store charge electrostatically using reversible adsorption of ions of the electrolyte onto the active surface of the material. During discharge process, the ions return back to the electrolyte solution [1]. Supercapacitors based on EDL mechanism store significantly more energy than conventional capacitors due to the large interfacial area and the atomic range of charge separation distances.

A model for the EDL mechanism was first developed by von Helmholtz investigating the distribution of opposite charges at the interface of colloidal particles, as illustrated in Fig. 1.2a [11]. Helmholtz EDL model states that two electrodes of opposite charge form a condensed layer at the electrode/electrolyte interface and are separated by atomic distances, in the order of 0.5 nm . This simple model is only valid for high concentration electrolyte solutions, without considering the diffusion of ions in the solution and the interaction between the dipole moment of the solvent and the electrolyte. Considering this limitation, the transition will not be so abrupt in more diluted solutions, hence increasing the thickness of the double layer, as shown in Fig. 1.2b. This modification of the previous

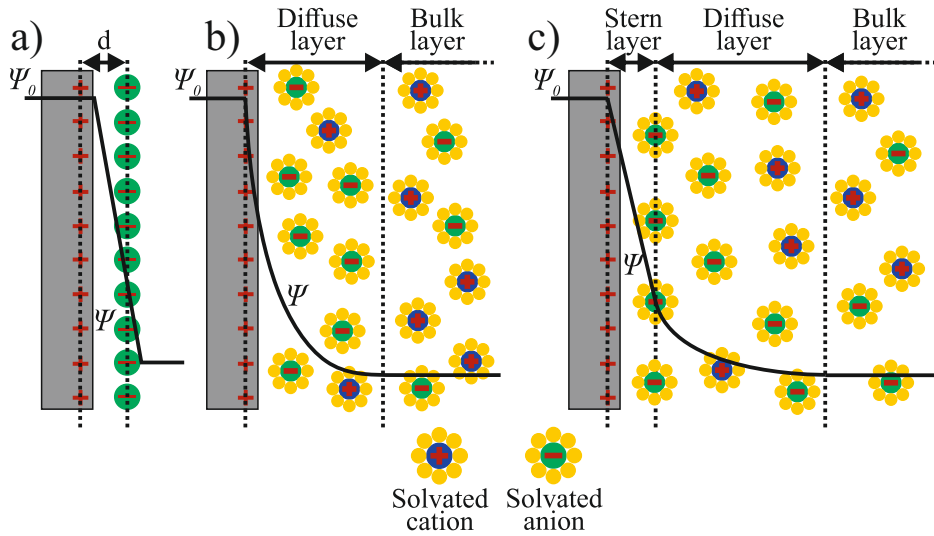


FIGURE 1.2: Physical models for the electric double layer at a positively charged surface: (a) The Helmholtz model, (b) the Gouy-Chapman model, and (c) the Stern model, combining both.

model was introduced by Guoy and Chapman. The thickness of the EDL, commonly referred to as diffuse layer, is related to the distance from the charged surface at which the ions can escape to the bulk by thermal motion. However, the Gouy-Chapman model overestimates the EDL capacitance and it is insufficient for highly charged double-layers. Subsequently, Stern combined the two models to identify two regions of ion distribution: i) the inner region called the compact layer or Stern layer, where the ion distribution can be treated as an adsorption process; and ii) the diffuse layer of Guoy-Chapman, where the hydrodynamic motion of the ionic species is considered, as depicted in Fig. 1.2c. The capacitance can be treated as a combination of capacitance from the two regions, avoiding the problem of high capacitance that arises in the Gouy-Chapman treatment [11, 12]. Considering that these two layers can be treated as two capacitors in series, C_H (Helmholtz layer) and C_{diff} (diffuse layer), the total capacitance (C_{dl}) can be expressed as

$$\frac{1}{C_{dl}} = \frac{1}{C_H} + \frac{1}{C_{diff}} \quad (1.1)$$

Grahame developed the four regions-based electrical double layers theory. It consists on dividing the adjacent region to the surface into the inner Helmholtz plane in front of the electrode with small molecular distances and the outer Helmholtz plane, comprising the Helmholtz layers. Besides these regions described, it also encompasses the diffusion region and the bulk region suggested by Stern. This theory includes the specific adsorption of negative ions on the surface via chemical interaction. Bockris, Devanathan, and Müller expanded the theory of EDL with the predominance of solvent molecules around the interface. In this approach, both the charge separation and diffusion layers were considered and is suitable for the explanation of high-current-power EDLCs [13].

As a result of the energy stored through electrostatic accumulation of charges, there is no faradaic (redox) reaction at EDLC electrodes, as a major difference from batteries (Fig. 1.3a). Hence, the cyclic voltammetry (CV) signature should show quasi-rectangular behaviour (Fig. 1.3b) and the galvanostatic charge-discharge (GCD) should display a triangular-shape (Fig. 1.3c) accounting for the linear response of voltage with time. This surface storage mechanism allows fast charge-discharge processes, large amount of cycling (up to millions) and superior power performance [1].

1.2.2 Pseudocapacitors

A new type of electrochemical capacitance, referred to as pseudocapacitance, was discovered in 1971 using RuO_2 [14]. Pseudocapacitive materials base their charge storage mechanism on fast and reversible redox reactions between the electrolyte and their active surface (Fig. 1.4a). Therefore, this mechanism is considered faradaic in origin as compared with EDL [11]. Although the charge storage is based on redox processes implying similar behaviour as batteries, the rapid faradaic reactions are not limited by diffusion and, subsequently, reflect electrochemical signatures similar

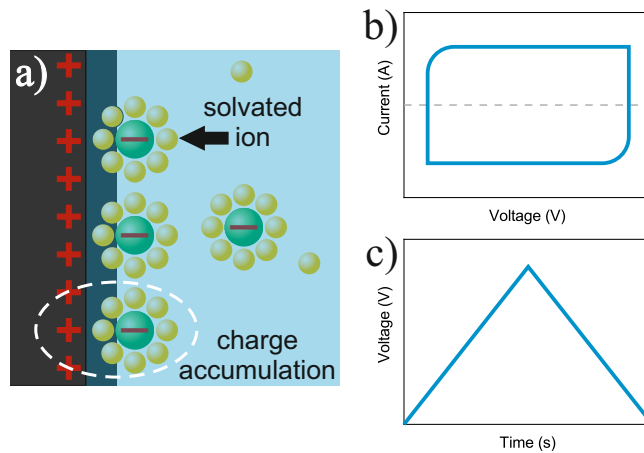


FIGURE 1.3: (a) Schematic diagram of charge storage mechanism of electrical double-layer capacitors. (b) CV and (c) GCD electrochemical signatures of EDLCs.

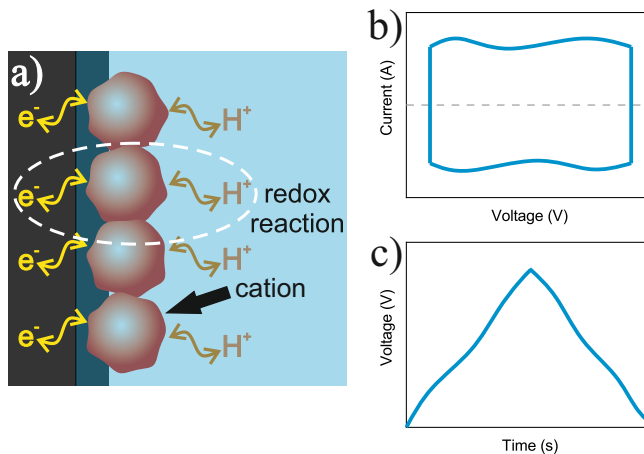


FIGURE 1.4: (a) Schematic diagram of charge storage mechanism of pseudocapacitors. (b) CV and (c) GCD electrochemical signatures of pseudocapacitors.

to EDLCs [4]. Hence, pseudocapacitive materials should show approximately rectangular CV (Fig. 1.4b) and, accordingly, the GCD curve should present almost linear voltage response with time (Fig. 1.4c). Additionally, some battery-like materials, also known as extrinsic pseudocapacitive materials, exhibit pseudocapacitive signatures or fast charging with good capacitance retention after nanosizing [15–18]. Therefore, the definition of pseudocapacitive materials should be ascribed to the electrochemical behaviour rather than the material definition itself.

1.3 Supercapacitor Electrode Materials

The capacitance and charge storage of SCs depend largely on the electrode materials used. Therefore, new materials need to be investigated and synthesised in order to obtain better capacitance and improved performance [19].

The materials suitable to reach high capacitance by EDL mechanism should have high specific surface area and electronic conductivity. In general, electrode materials for SCs can be classified in three types: (i) carbon-based materials with high specific surface area [20–23], (ii) conducting polymers [24–28], and (iii) metal-based materials [23, 29, 30]. Moreover, combination of these types of materials could develop composites with enhanced properties [31].

1.3.1 Carbon-based materials

Carbon is one of the most abundant materials, with a wide variety of structures and morphologies. Most EDLCs use porous carbons as active electrode material [12]. The interest in carbon-based materials arises from the unique combination of chemical and physical properties, which include high conductivity, good corrosion resistance, high temperature stability, flexibility and compatibility to process composite materials as well as relative low cost [32].

A wide range of natural materials can be used as precursor of carbon-based materials, such as coal, crude oil or biomass. Additionally, sizing

these materials to the nanoscale, changes greatly their properties. Consequently, zero-dimensional (0D), one-dimensional (1D), two-dimensional (2D) as well as three-dimensional (3D) carbon materials present different outcomes and performances. 0D carbon materials refer to sphere-shaped particles. Activated carbon (AC), carbon nanospheres, and mesoporous carbon are the main examples of these materials. Large specific surface area is obtained for 0D carbon materials with controllable pore size and distribution [33]. Ideal porous structures should contain macropores ($> 50\text{ nm}$) allowing infiltration of electrolyte, mesopores ($2\text{--}50\text{ nm}$) as the place for ion transport, and micropores ($< 2\text{ nm}$) for charge storage [34]. These materials are produced from carbon-rich precursors through physical activation at high temperatures ($700\text{--}1200^\circ\text{C}$) with H_2O , CO_2 and air, or chemical activation at lower temperatures ($600\text{--}800^\circ\text{C}$) with, for example, H_3PO_4 , KOH or ZnCl_2 [35]. Previous reports published AC electrodes displaying specific capacitance of $100\text{--}300\text{ F g}^{-1}$ [36–40].

In contrast with 0D materials where electrons are transported via hopping between trap states or via diffusion, 1D nanostructured electrodes form a continuous network, favourable for charge transport [41]. The most characteristic 1D carbon materials are carbon nanotubes (CNT), which exhibit much higher conductivity than AC (Fig. 1.5a). CNT can be categorized to single-wall carbon nanotubes (SWCNT) or multiwall carbon nanotubes (MWCNT) and can be fabricated by different techniques, such as arc-discharge method, chemical vapour deposition (CVD), plasma enhanced CVD, pyrolysis of hydrocarbons and pulsed laser vaporization [32, 42]. Pure CNT are reported to possess specific capacitance in the range of $20\text{--}100\text{ F g}^{-1}$ in aqueous electrolyte [43–46]. The relatively low capacitance may be ascribed to limited surface area and to their hydrophobic property.

The most common 2D carbon material is graphene, a flat monolayer of sp^2 -bonded carbon atoms packed into a 2D honeycomb lattice (Fig. 1.5b) [47]. Due to its unique structure, graphene has prominent intrinsic chemical and physical features, such as strong mechanical strength, high electrical and thermal conductivity as well as large surface area [48]. These outstanding properties make graphene suitable for energy storage devices,

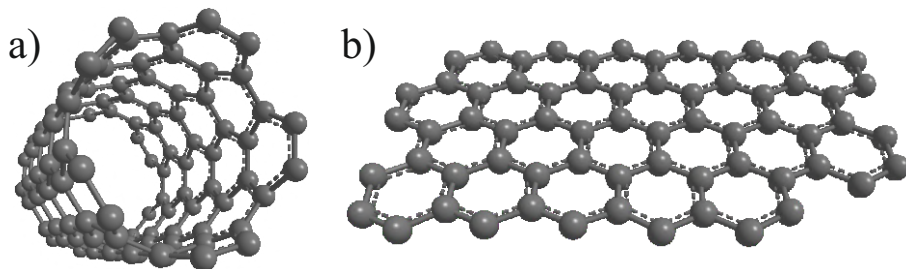


FIGURE 1.5: 3D model of (a) a single-wall carbon nanotube and (b) a graphene monolayer.

among other applications [49, 50]. Different approaches have been followed to synthesize graphene-based materials, including epitaxial growth, CVD, micromechanical exfoliation of graphite, solvent exfoliation, solvent free gas-phase microwave plasma reactor synthesis, arc-discharge synthesis, and reduction of graphene oxide (GO) [48]. GO can be considered as a monomolecular graphite-like layer highly functionalized with oxygen and hydrogen-containing groups and it is synthesized by either the Brodie, Staudenmaier or Hummers methods. GO is an electrically insulating material, although the restoring of the π -network of the disrupted sp^2 -bonding structure can recover the electrical conductivity through its reduction. The product of this reaction results in a material similar to pristine graphene, called reduced graphene oxide or rGO (Fig. 1.6) [51]. The theoretical specific capacitance of graphene when the entire surface is fully covered, is $\sim 550 F g^{-1}$. However, the measured capacitance of graphene is lower due to agglomeration during preparation and application processes. Practical specific capacitances are in the range of $100\text{--}350 F g^{-1}$ [52]. Furthermore, the doping of heteroatoms to the lattice of the pristine graphene structure leads to a change in chemical activity, improves wettability and induces pseudocapacitance. The most used doping atoms include boron, nitrogen, sulfur or phosphorus [53]

In 3D structures, more percentage of active surface is exposed in the electrolyte, which will effectively improve electrochemical properties. A 3D microstructure composed of well-interconnected small and large pores

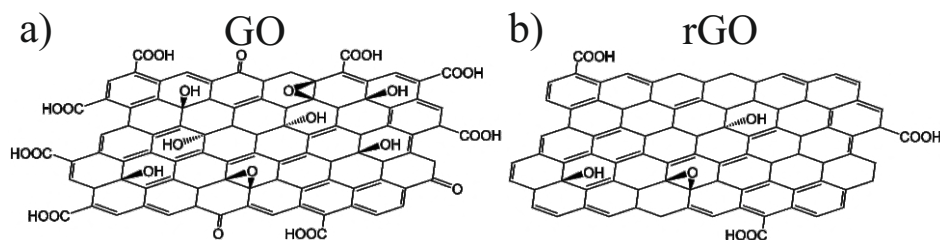


FIGURE 1.6: Molecular structure of (a) graphene oxide (GO) and (b) reduced graphene oxide (rGO).

provides a continuous electron pathway for good electrical conductivity and contributes to the acceleration of ion transfer by reducing the diffusion pathways [54]. A common strategy for building 3D electrodes is the direct growth of free-standing electrodes with high electrical conductivity on the current collector to achieve homogeneous electrodes. Alternatively, a thin layer of the material can be deposited over a nanostructured current collector [55]. Different hierarchical 3D structures can reach capacitances up to 350 F g^{-1} [54].

1.3.2 Conducting polymers

Conducting polymers (CPs) constituted by a conjugated bond matrix are used in various SC applications due to their higher energy density than metal oxides, low cost, limited environmental impact, high voltage window and reversible faradaic redox capabilities [5, 31]. CPs, such as polypyrrole (PPy), polyaniline (PANI), or polythiophene (PTh), accumulate and release charges through redox processes associated with π -conjugated polymer chains [12]. CPs are synthesized by means of chemical or electrochemical oxidation/reduction of the monomers [56]. Doping of CPs is obtained during oxidation/reduction of the monomers with the insertion of counter ions [57]. Reported specific capacitance of different CPs are in the range of $100\text{--}500 \text{ F g}^{-1}$ [58].

1.3.3 Metal-based materials

Electrochemical capacitors based on pseudocapacitive metal oxides or hydroxides can provide higher specific capacitance than conventional carbon-based materials and better electrochemical stability than CPs [59, 60]. The general requirements for these compounds for SC applications are: (i) the oxide should be electronically conductive, (ii) the metal can exist in two or more oxidation states able to coexist with no phase changes involving irreversible modifications, and (iii) protons can be freely intercalated into the lattice on reduction [11].

Many transition metal oxides (TMO) have been reported as either intrinsic or extrinsic pseudocapacitive materials, such as ruthenium oxide (RuO_2), manganese dioxide (MnO_2), nickel oxide (NiO), iron (II,III) oxide (Fe_3O_4) or vanadium (V) oxide (V_2O_5) [23, 29, 30]. The redox behaviour of these oxides relates to the multivalent nature of the TMO. Most of these metals are able to change their oxidation states as a result of the reversible interaction with proton and/or hydroxide anions and the corresponding redox reactions take place either at the surface or at the bulk of the oxides. Despite their great specific capacitance, most of the metal oxides suffer from low conductivity, poor stability and poor rate capability and durability upon charge/discharge cycling [23].

1.3.4 Composite materials

As previously stated, despite the fact that their specific capacitance is not high enough, carbon-based materials are frequently used as electrode materials in commercial SCs. As compared to these materials, TMO and CPs present higher energy storage capabilities. However, their main drawbacks of low cyclic stability during charge/discharge and high resistance hinder their practical use for SC applications. These challenges can be overcome by using composite materials as electrodes with high energy and power densities [31].

Regarding conductive polymers, for example PANI-graphene nanocomposites have been successfully developed preserving the good conductivity, stability of physicochemical properties and long cycle life of graphene, adding the pseudocapacitance from CPs. Moreover, the inclusion of CPs improves the wetting between graphene and electrolyte due to their hydrophilic nature [61]. The integration of nanoscale TMO into carbon materials may generate composite electrodes in which a conductive backbone (carbon) supports the high capacitance TMO nanostructures. Several studies have proven the high potential of carbon-TMO composites as electrode materials for SCs due to their improved electrochemical performance through synergistic effect of EDL and pseudocapacitance, avoiding the drawbacks from TMO as low conductivity, poor stability and poor rate capability, and maintaining the advantages of carbon-based materials arising from their good electrical conductivity [62–64].

1.4 Fabrication methods

Considering the critical role of the electrode material and that the output is influenced by the fabrication method, different approaches are being investigated for the synthesis of new nanostructured materials with enhanced performance [5, 65, 66]. Innovative techniques shall be investigated to overcome the limitations of conventional methods as hydrothermal combined with thermal annealing, sol-gel, electrochemical deposition or chemical precipitation [67–69]. The main disadvantages of these conventional techniques are that they use multi-step processes, many chemical products and high temperature processing steps. The chemical reactions often use hazardous precursors or reveal chemical incompatibilities. In addition, the thermally-activated processes need prolonged use of high temperatures, impeding the use of temperature-sensitive substrates.

Laser-based techniques are being employed as an alternative to conventional methods and are revealing high potential for the fast and versatile fabrication of SC electrodes and devices [70–73]. Lasers are powerful tools utilised for various applications in industry, medicine, science and

material processing [74]. Materials processed with laser techniques benefit from the characteristics of laser light, including strong localized heat or photo-treatment with high spatial resolution, time-controlled processing as well as control of depth of heat treatment or selective non-thermal excitation [75]. These treatments of the materials are highly dependent on the laser characteristics, the system set-up, the optical components and the environmental conditions. These variables include the wavelength, power, pulse width, energy profile and the pulse repetition rate. One of the most essential elements is the wavelength of the radiation, considering that determines the percentage of reflected, absorbed and transmitted light by the material, as well as the type of interaction in the target. Laser power is directly associated to the amount of energy transferred to the material as a function of time. This parameter is time averaged, hence it is highly related to the next variable: the pulse width which is the amount of time of interaction between the beam and the material. The outcome of a laser treatment is a direct consequence of this parameter, since the variation of time scale of interactions affects the different arising phenomena. Since the energy of a laser beam is not constant throughout its cross-section, the description of the profile is crucial. Most laser present a circular cross-section and a Gaussian beam energy profile. In order to increase the energy density, lenses could be used to focus the laser beam [76].

Besides the dependences outlined, the interaction mechanisms between laser light and the material depend on the physical and chemical properties of the material involved. The laser light excites the electrons causing the dissipation of this excitation energy into heat within the material in a short time through electron-electron and/or electron-phonon scattering. The laser beam can be considered as a heat source which induces a temperature rise on the surface or bulk of the material, depending on its absorption coefficient. The laser-material interactions can also be non-thermal

(photochemical), causing the photoactivation of chemical reactions. Therefore, the laser-induced reactions could be activated thermally, if the thermalization of the laser excitation energy is fast compared to any other process; photochemically, if the first reaction step is faster than the thermalization of the excitation energy; or by combination of both [75]. The result of these types of interactions is the structural-compositional modification of the irradiated material in a straightforward way.

Laser techniques offer great experimental versatility and fast fabrication avoiding lasting high-temperature conditions and the usage of toxic chemicals [72, 73]. Specifically, the heating and photolysis of the irradiated material during the action of short laser pulses, in the *ns* time scale, produce interactions out of the thermodynamic equilibrium opening up new possibilities in the synthesis and deposition of materials in form of thin films. As a consequence, laser-based methods allow for [75]:

- Selective heating and photochemical reactivity
- Ultrafast phase changes (recrystallization, melting, vaporization, plasma formation) besides complex coupling between physical-chemical processes
- Synthesis of metastable materials that cannot be produced by other conventional techniques
- Single-step deposition of complex multicomponent materials, highly crystalline heterostructures and composite films

1.4.1 Laser fabrication for supercapacitors

Laser-based methodologies are applicable for synthesis, reduction, modification and assembly of carbon-based materials for energy storage electrodes and devices. One of the most employed methods for the fabrication of graphene-based materials is the laser reduction of GO films through a scanned laser beam, since GO films are electrically insulating. When subjected to laser radiation, GO can lose most of its oxygen-containing groups,

resulting in the formation of rGO, with high conductivity and excellent electrochemical performance [77, 78].

The direct laser reduction of free-standing GO films for the fabrication of SCs has been mainly accomplished processing GO with CO₂ laser systems. In these devices, conductive rGO can be combined with non-irradiated GO working as solid electrolyte [70]. Low cost production of SCs have been performed irradiating a GO/polymer film by means of a DVD writing technology [79]. By using an intensity-modulated line beam CO₂ laser under a nitrogen flow, high-throughput reduction of GO paper has been achieved. Sweeping a wide beam in a large area, GO is directly converted to highly porous and conductive rGO. This method has been successfully implemented in sandwich-type SC devices [80]. Electrodes displaying high specific capacitance, high energy and power densities and high stability under cycling have been fabricated combining femtosecond laser radiation with precise transfer of electrolyte [71]. The direct pattern and transfer of GO on flexible substrates can be achieved by the laser welding technique. The laser-induced localized heat on the carbon-material is able to melt PET by heat conduction, followed by a welding after cooling. The laser pattern can be completely transferred to the PET flexible substrate by a straightforward detachment process [81]. Furthermore, SC electrodes have been improved by synthesizing rGO containing electrochemically active functional groups. The combination of graphene with metal-organic frameworks (MOF) as highly porous and high surface area materials develops a unique 3D structure for high performing SCs. This method employs a CO₂ laser to simultaneously reduce GO and carbonized the MOF material [82]. Different studies report the promising outcome of the fabrication of electrodes composed of rGO decorated with pseudocapacitive oxide nanostructures, using RuO₂, MnO₂ and oxygen-deficient TiO₂ nanoparticles [83–85]. SCs can be also synthesized using pulsed laser ablation in liquids. Electrodes with anchored WO₃ NPs in rGO sheets present attractive electrochemical and structural characteristics, enhancing the capacitance of the supercapacitor, compared to pure WO₃ [86].

Furthermore, laser-induced graphene (LIG) is the material obtained from the laser graphitization of carbon-containing materials (polymers, biomaterials) and it is suitable for the fabrication of flexible devices based on graphene-like materials. LIG includes a series of 3D porous materials with exceptional conductivity, high surface area and great thermal stability [87].

Given all the examples of laser techniques applied to the development of SC electrodes and devices is clear that great progress in the energy storage field has been accomplished. However, further research in novel techniques, new combinations of materials and different ways to enhance the electrochemical properties need to be addressed. In this thesis, a laser technique was used for the deposition of thin film electrodes. Multicomponent target dispersions were submitted to laser radiation and the evaporated material was collected onto a solid substrate surface. The technique employed is similar to Pulsed Laser Deposition (PLD), with the exception of target preparation and applied laser fluence values.

1.4.2 Pulsed Laser Deposition

Pulsed laser deposition (PLD) is a physical vapour deposition process. A pulsed laser beam is focused onto a solid target of the material to be deposited. Each laser pulse with laser energy density surpassing the vaporization threshold vaporizes or ablates a small amount of the material creating a highly forward-directed plasma plume. The evaporated material is deposited onto a substrate surface placed plan-parallel to the irradiated target (Fig. 1.7) [88].

PLD is particularly suitable for the deposition of highly crystalline complex materials, through the irradiation of multicomponent targets. Under optimized irradiation conditions, this technique allows a congruent material transfer from the target to the substrate, which is commonly heated to high temperatures during the deposition process. Moreover, the generated plasma promotes chemical reactions between the evaporated material and ambient gas molecules when the irradiations are conducted in reactive atmosphere. The technique allows also the growth of multilayered

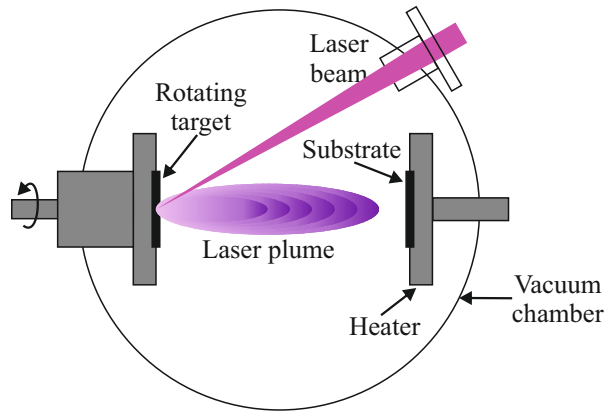


FIGURE 1.7: Schematic diagram of a typical pulsed laser deposition (PLD) set-up.

epitaxial heterostructures during the same irradiation process through the successive irradiation of targets with different composition [89]. Concerning functional properties, studies are focused on the growth of new complex oxide superconductors, semiconductors or magnetic films, group III nitrides which are promising materials for light-emitting devices, carbon based films, such as diamond, graphene, SiC and metal carbides for technological applications such as high-power and high frequency electronic devices, light emitting devices, hard coatings and sensors as well as metal thin films, including refractory and rare earth metals [90].

1.4.3 Matrix Assisted Pulsed Laser Evaporation

Besides inorganic materials, PLD technique can also be used for the growth of organic thin films. However, the intense laser pulses generally decompose the organic molecules. Only a few types of polymers, for instance polymethylmethacrylate (PMMA) or polytetrafluoroethylen (PTFE or Teflon) have been successfully deposited with this technique using UV laser radiation. Different approaches can be followed to solve this limitation [91]. Matrix-assisted pulsed laser evaporation (MAPLE) technique was

developed in the late 1990s as a modification of the PLD method for addressing this issue [92]. Conventional MAPLE consists on the irradiation of a frozen target by intense laser pulses. The target is composed of organic or inorganic compounds dissolved or dispersed in a volatile organic solvent with high absorption at the wavelength of the incident laser radiation. The choice of the highly absorbent solvent is critical to protect the material to be deposited from the direct action of the laser pulses. The solvent concentration should represent a low weight percentage to produce a homogeneous solution. The liquid target is frozen in liquid nitrogen, until its solidification, forming the target to be irradiated. Thus, the laser pulses produce a rapid photothermal heating of the solvent up to its spinodal point, leading to its explosive boiling. The generated vapour transports the organic molecules towards the facing substrate where the thin film grows under the action of subsequent laser pulses [88, 93].

The primary benefits of MAPLE technique are that it is a relatively straightforward process, has good control over the film thickness, a variety of independent deposition parameters, uniform deposition on non-planar substrates and the ability to produce multilayer and composite films. However, UV-MAPLE method has a series of limitations, including high roughness values in the deposited films, low UV laser deposition rates and the possibility for reactive radical formation from the organic solvents under the action of the UV laser pulses [94]. The technique has been used for the deposition of functional polymers [95–98], biomaterials [99, 100], colloidal nanoparticles and quantum dots [101, 102], carbon nanoparticles and nanotubes [103–106]. In the most reported UV-MAPLE experiments toluene has been used as solvent matrix for their good UV absorption and low vaporization laser fluence threshold. However, UV laser radiation could produce the photolysis and further polymerization of toluene, leading to the co-deposition of polymeric by-product materials [104, 105]. Moreover, the UV laser radiation can be absorbed also by the dissolved molecules and the photochemical reactions lead to the decomposition of the irradiated material.

One novel approach to the fabrication of composite layers is the Resonant Infrared MAPLE (RIR-MAPLE). This method is especially suitable for the deposition of composites of inorganic/organic films, organic materials and nanoparticles avoiding damage in the target materials since uses low-energy sources and allows using water ice as the target matrix [107]. Taking into consideration that the maximum absorption coefficient of the water ice matrix is comparable to that of liquid water [108], the technique uses a low-energy Er:YAG ($\lambda = 2940 \text{ nm}$) laser to irradiate the frozen target solution. The target matrix (or solvent) can be different than water, but it must include hydroxyl bonds which are resonant with the laser wavelength. Then, the matrix is evaporated releasing and transferring the target material to the substrate. RIR-MAPLE has been implemented in the fabrication of SC electrodes developing composites where 2D $\text{Ti}_3\text{C}_2\text{T}_x$ flakes were embedded in a polyfluorene matrix. The resulting highly transparent electrodes have a high areal capacitance [107].

1.4.4 Reactive Inverse MAPLE

For the deposition of complex nanocomposite films through UV laser radiation without the presence of by-product materials, Reactive Inverse Matrix-Assisted Pulsed Laser Evaporation (RIMAPLE) method was recently developed by the Laser Processing Research group of ICMAE. This technique combines the inverse MAPLE and the reactive MAPLE methods. The use of water as matrix solvent avoids completely the co-deposition of organic by-products, besides being non-toxic. The composite deposition is achieved at room temperature and without substrate heating. Thus, even polymeric substrate can be used. The absorption of the laser radiation occurs in the solute nanoentities instead of the solvent molecules, inducing a rapid heating of the solute, which subsequently leads to fast vaporization of the surrounding solvent through heat transfer. The amount of deposited material over the substrate can be controlled with the solute concentration and the number of applied pulses to the target. A further advantage of the technique consists in the possibility of the addition of reactive precursor molecules to the target dispersions. Novel nanocomposite thin films can

be obtained this way, through the simultaneous deposition and chemical reactions between the components of the target dispersions [109]. Even though this method is still in its initial steps towards being established as a prevailing technology, it has high potential due to its high versatility, straightforward route for the fabrication of carbon-based electrodes for energy storage and great flexibility in the synthesis of complex compounds.

1.5 Outline of the thesis

The development of new electrode materials for supercapacitor devices with enhanced performance is a major topic in the energy storage field that still needs to be addressed.

Laser-based fabrication methods were used for the synthesis of composite materials containing carbon-based materials and metal oxides. The Chapter 2 of this thesis is centred in the presentation of the electrodes' synthesis technique and the different characterization techniques used for the study of their morphological, compositional and electrochemical properties. Chapter 3 is focused on the fabrication of electrodes composed of carbon-based materials, such as rGO and MWCNT, and NiO nanoparticles. Different precursors are added to the target composition for obtaining nitrogen-doping of the carbon materials with the aim to enhance their electrochemical properties. In Chapter 4, the results related to composites consisting of carbon-based materials and CeO_x nanoparticles are presented. The electrochemical properties of these composites are significantly improved after the addition of manganese oxides (MnO_x). Different experimental procedures are followed to obtain the binary oxide $\text{CeO}_x/\text{MnO}_x$ composite. Finally, a functional device is fabricated using the electrodes exhibiting the best electrochemical performances. To conclude this chapter, the aqueous electrolyte is changed by an organic one, increasing considerably the voltage window, and it is tested in the rGO, MWCNT, CeO_x and MnO_x electrodes. A considerable increase in energy is observed maintaining a high power density. Finally, in Chapter 5, the thesis is concluded with the general conclusions obtained, limitations and potential future research.

Chapter 2

Experimental Methods

In this chapter, the laser-based deposition technique used for the fabrication of the electrode materials will be described and the general experimental conditions will be specified. Afterwards, an overview of the characterization techniques applied for the investigation of the surface morphology, chemical composition as well as functional energy storage performance will be detailed.

The characterization techniques included Scanning Electron Microscopy (SEM), Transmission Electron Microscopy (TEM) and Small Angle X-ray Scattering (SAXS) for the investigations of structure and morphology, and X-ray Photoelectron Spectroscopy (XPS), Fourier-transform Infrared Spectroscopy (FTIR) and Raman Spectroscopy for the identification of chemical composition and chemical bonding states present in the materials. Electrochemical techniques as Cyclic Voltammetry (CV), Galvanostatic Charge-Discharge (GCD), Electrochemical Impedance Spectroscopy (EIS) and Step Potential Electrochemical Spectroscopy (SPECS) were used for the investigations of the storage performance of the electrodes.

2.1 Laser Deposition Technique

RIMAPLE laser technique was chosen for the deposition of composite thin film electrodes. Distilled water with low absorption of the incident UV laser radiation, 266 nm, was used as solvent material. The RIMAPLE process diagram is depicted in Fig. 2.1. As a first step, aqueous dispersions

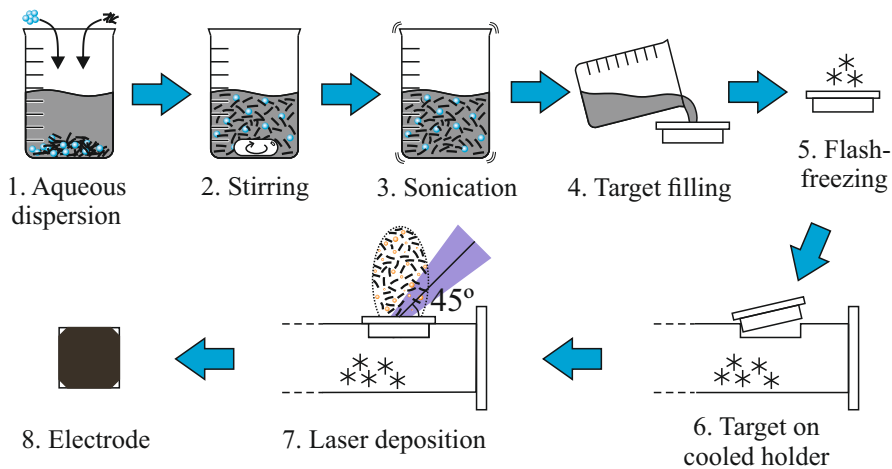


FIGURE 2.1: Diagram of RIMAPLE deposition steps followed for the fabrication of electrodes.

containing the materials of interest, nanocarbon-based compounds and metal oxide nanoparticles, as well as organic/inorganic precursors were prepared. The dispersion was stirred for an hour and sonicated for 1 *min* prior to the filling of the target holder. When different compounds were dispersed in the same solution, all the powders were added simultaneously. If a compound was soluble in water, it was dissolved previously to the addition of other materials. The nanocarbon-based compounds selected for the preparation of target dispersions were graphene oxide (GO) powder (Nano-Innova Technologies) composed of 1 - 15 layers thick flakes around $1 \mu\text{m}^2$ in area, and multiwall carbon nanotubes (MWCNT) from Sigma-Aldrich, with diameters of about 10 *nm* and lengths of up to 1.5 μm , doped with carboxylic groups in order to enhance their dispersibility. Cerium (IV) oxide nanopowder (Sigma-Aldrich) of about 25 *nm* in diameter, and NiO nanopowder (Sigma-Aldrich) about 50 *nm* in diameter and 99.8% purity were also used as nanoparticles for the preparation of target dispersions. Manganese (II) acetate (Sigma-Aldrich) and nitrogen containing precursor molecules as ammonia, urea, melamine and imidazole (Sigma-Aldrich) were added to the dispersions.

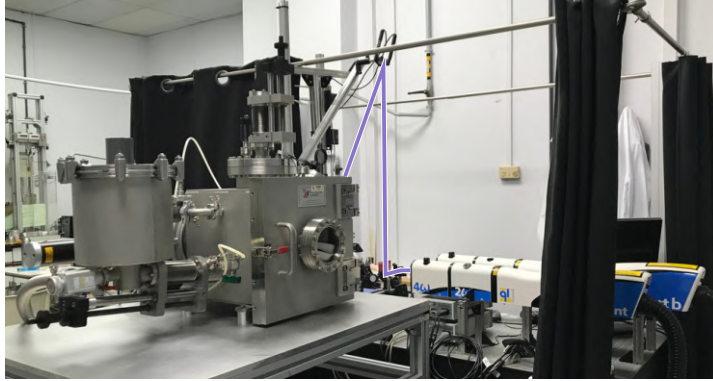


FIGURE 2.2: RIMAPLE deposition vacuum chamber with laser path depicted for better interpretation.

After sonication, the target dispersions were subjected to a flash-freezing process in liquid nitrogen to ensure the homogeneity of the target. After solidification, the targets were placed onto a liquid nitrogen cooled holder inside a vacuum chamber, shown in Fig. 2.2. All the deposition process is carried out at room temperature in $20 Pa$ N_2 background gas environment. The vacuum chamber was evacuated previously to a residual pressure of $0.1 Pa$. The N_2 background gas is essential to ensure the confinement of the laser plasma for the controlled growth of the thin films. The films were deposited by accumulation of UV laser pulses ($266 nm$ wavelength, $\approx 4 ns$ pulsed duration, $10 Hz$ repetition rate) with the aid of a Quantel Brilliant B Nd:YAG laser system, presented in Figs. 2.2 and 2.3. The laser fluence directed to the frozen target was set at $0.4 J cm^{-2}$. During the deposition, the laser beam scans the target surface with an incident angle of 45° . A plasma plume is generated under the action of the laser pulses, as outlined in Fig. 2.4a and the experimental plume obtained is presented in Fig. 2.4b. Flexible and conducting $1 \times 1 cm^2$ substrates were placed in front of the target at a separation distance of $4 cm$. $0.1 mm$ thick polypropylene (PP) films coated with sputtered Au ($20 nm$)/Cr ($5 nm$) as well as $0.5 mm$ thick copper and $0.1 mm$ thick stainless steel AISI 316L were used as substrate materials.

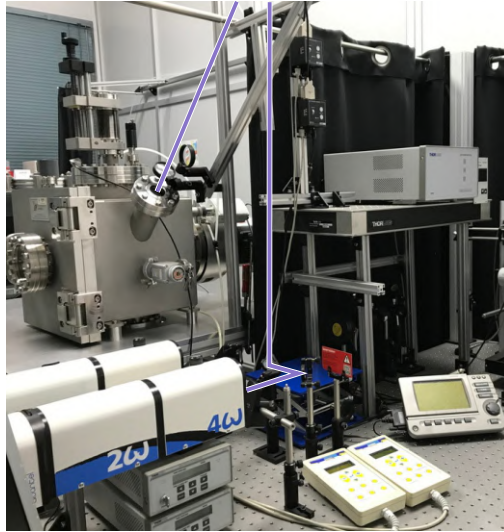


FIGURE 2.3: RIMAPLE deposition equipment with laser path depicted for better interpretation.

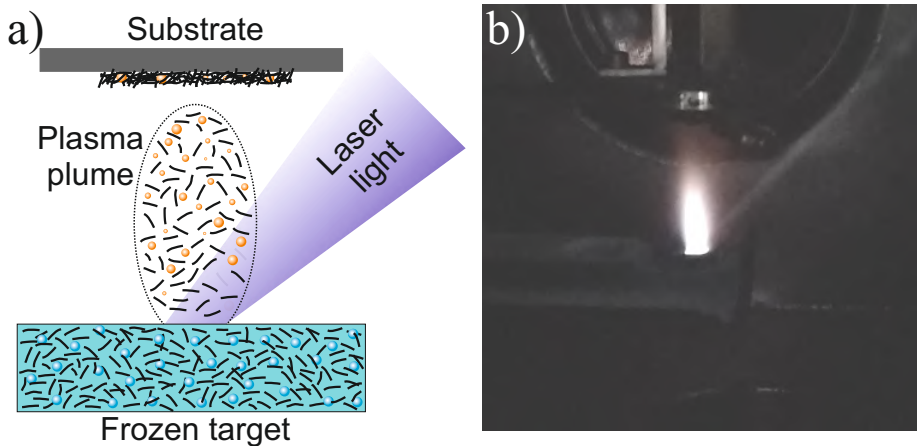


FIGURE 2.4: (a) Schematic diagram of RIMAPLE deposition mechanisms and (b) experimental plume formed during deposition process.

2.2 Morphological and Compositional Characterization

2.2.1 Scanning Electron Microscopy (SEM)

Scanning Electron Microscopy (SEM) is an imaging technique providing microscopic-scale information on the topography and composition of a specimen. To this aim, the sample surface is scanned by a finely focused electron beam usually released from a hot filament. However, in Field Emission SEM (FESEM) a cold cathode is used, emitting electrons under the application of a very high electric field, providing better resolution as compared to conventional SEM [110]. The energy of the electrons is in the range $0.1 - 30 \text{ keV}$. The electrons are subsequently accelerated, being modified by different apertures, magnetic and electrostatic lenses as well as electromagnetic coils. Those modifications produce the successive reduction of the beam diameter allowing the scanning of discrete locations on the sample surface. At each one of these locations, the interaction between the electron beam and the sample generates electron products, backscattered electrons (BSE) and secondary electrons (SE), that are collected by different detectors, allowing image formation. This operation takes place under high vacuum conditions ($< 10^{-4} \text{ Pa}$) to reduce the unwanted scattering of beam electrons, BSE and SE from residual molecules and atoms. Samples should have a conducting grounding path in order to avoid the accumulation of electric charge [111].

FESEM images were obtained using a FEI Quanta 200 FEG-ESEM electron microscope, located at ICMAB, primarily for the measurement of the thickness of samples through the investigation of samples' cross-section. Extreme high-resolution SEM (XHRSEM) images were also obtained with a Magellan 400L microscope (FEI) located at the Catalan Institute of Nanoscience and Nanotechnology (ICN2) facilities.

2.2.2 Transmission Electron Microscopy (TEM)

Transmission Electron Microscopy (TEM) principle is similar to that of the optical microscope, using electrons and magnetic lenses instead of light and glass lenses, respectively. Electrons are emitted from a source and subsequently accelerated and focused into a small, uniform beam using a condenser lens. In the path of the electrons, a small condenser aperture is placed to exclude the ones travelling at large angles to the optical axis. Then, the beam passes through the sample at normal incidence. The samples are placed in a holder that can be tilted in one or two directions and even rotated if needed. The transmitted beam is focused by the objective lens to form an image or a diffraction pattern on an imaging system [112, 113].

A variety of imaging modes can be applied such as bright-field contrast images, crystallographic dark-field images, selected-area electron diffraction (SAED), micro- and nano-diffraction or high resolution TEM (HRTEM) images. It can also be used to perform point chemical analysis using X-rays (Energy-dispersive X-ray spectroscopy or EDX) or inelastic Electron Energy Loss Spectroscopy (EELS). Another mode of operation, called Scanning TEM (STEM) is based on the demagnification of a small bright electron beam and its scanning over the specimen in a two-dimensional raster. Depending on the position of the detector and its detection angle, bright-field or annular dark field images can be formed, specifically High-Angle Annular Dark Field (HAADF) images which allows for high-resolution Z-contrast chemical imaging [112].

The specimen needs to be thin enough, of the order of a few *nm* to transmit electrons with sufficient energy [114]. Consequently, the pristine fabricated electrodes cannot be analysed and a sample preparation is required. In our particular studies, a copper grid was lightly scratched over the electrode surface and placed it on the TEM specimen holder for analysis. For the structural characterization at the nanoscale, HRTEM images were acquired using the FEI Tecnai G^2 F20 equipment located at ICN2 facilities. The particle size analysis was performed through HAADF-STEM and the elemental composition by EDX spectroscopy, using the same equipment.

Furthermore, HRTEM and SAED images were obtained using a JEOL 2010 UHR field emission gun microscope operated at 200 kV with a measured spherical aberration coefficient of 0.47 ± 0.01 at the Consiglio Nazionale delle Ricerche - Istituto Officina dei Materiali (CNR-IOM) in Trieste (Italy) in the frame of a NFFA-Europe project.

2.2.3 Small Angle X-ray Scattering (SAXS)

A scattering experiment consist on the interaction of a planar wave characterized by a defined direction of incidence \vec{k}_0 with the object's electron or nucleus that becomes a source of spherical waves by itself [115]. Then, the experimentally observed scattered intensity describes the constructive interference between the waves scattered by atoms as a function of angle, defined by \vec{k} . The scattering vector is defined as a change in the momentum transfer ($\vec{q} = \vec{k} - \vec{k}_0$) mapping out all scattering into reciprocal space. The magnitude of \vec{q} is

$$|\vec{q}| = 4\pi/\lambda \sin(\theta/2) \quad (2.1)$$

where λ is the wavelength of the incident wave and θ is the scattering angle [116]. If there are nanoscale regions or particles embedded in a sample with different electron density from the matrix, the X-ray scattering from these regions will locate at small angle extent, usually within 5° around the incident beam. This technique is called Small Angle X-ray Scattering (SAXS) and it is depicted in Fig. 2.5 [117].

With the application of synchrotron radiation sources, SAXS has become a powerful tool to study nanostructure systems, such as biological macromolecules, phospholipids, polymer and related materials, nanomaterials, and superlattices. The main application of SAXS techniques on nanomaterials include the investigations of superlattice structures of nanoparticles, their size and distribution, as well as nucleation and growth process, besides porosity [117, 118].

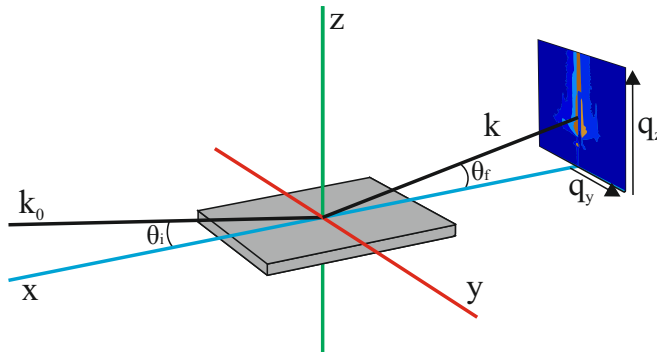


FIGURE 2.5: Schematic diagram of the SAXS geometry.

According to the experimental set-up, SAXS measurements are classified into two basic types: the transmission SAXS mode and the reflection mode. The reflection mode technique includes the Grazing Incidence SAXS (GISAXS), and it is suitable for films supported by a substrate where transmission mode cannot be applied to detect the nanoscale density correlations and the shape of the scatters due to restrictions imposed by the thickness of the substrate material [117].

The analysis of particle morphology usually begins with an inspection of the asymptotic behaviour of the SAXS spectrum. The Guinier approximation describes the asymptotic behaviour in the small q region, and approximates any form factor function as a Gaussian function in the small angle limit. This small q values must meet the requirement $q < 1/R_g$, where R_g , the radius of gyration, is the root-mean-square (RMS) of the scattering length density weighted distances from the center of mass to each atom of the particle. In addition, it requires scattering data that contains no structure factor, condition only met for dilute solutions. The Porod approximation describes the asymptotic behaviour at high q , satisfying $q \gg \pi/R_g$. When particles are randomly oriented 3D solid objects with sharp interfaces, the intensity in this region follow a power law decay of q^{-4} , also known as Porod's law [119].

For many of the well-defined particles with simple geometric shape, as spheres (three dimensional), thin disks (two dimensional) or thin rods (one

dimensional), it is possible to calculate the intensity curve for the whole range of q without making any approximations. For very small q , the three intensity curves merge together, despite the large differences in the shape of the particles, which is the basis for the Guinier law. At large q , the intensity can be represented by

$$I(q) \propto q^{-\alpha} \quad (2.2)$$

Determining the slope of $\log(I)$ vs. $\log(q)$, the value of α reveals the structure of the system, where $\alpha = 1, 2$, and 4 corresponds to an infinitely thin rod, an infinitely thin disk and a sphere with sharp interfaces (Porod's law), respectively [120].

These GISAXS measurements were performed at 8 keV of photon energy on electrodes deposited on Si substrates. The beam size was set to $1.5 \times 0.2\text{ mm}^2$ (horizontal \times vertical). The detector used was a Pilatus 1 M Dectris, and the distance between it and the sample was adjusted to 711 mm , calibrated with silver behenate (AgBH) as a reference pattern. First, the measurements were carried out with 60 s exposure time at 15% humidity. The incident angle was set at 0.2° in order to satisfy surface sensitive conditions. SAXSDOG software was used to perform horizontal (in-plane) cuts at the location of the Yoneda wing (located at the critical angle of the material under investigation) to convert the experimentally captured 2D patterns into 1D $I(q)$ patterns [121]. GISAXS measurements were also carried out in controlled relative humidity environment to further explore the pore structure of the composite. These experiments were performed recording scattering patterns continuously (every 30 s with 10 s exposure time) during 200 min while applying increasing and decreasing humidity ramps in the range of $15 - 90\%$ of humidity. All of these measurements were performed at the Austrian SAXS beamline at Elettra synchrotron facility (Trieste, Italy) [122] in the frame of a NFFA-Europe project.

2.2.4 X-ray Photoelectron Spectroscopy (XPS)

X-ray Photoelectron Spectroscopy (XPS) is a surface analysis technique utilised for the identification of existing elements on the surface of the studied material, as well as their chemical states. It involves the irradiation of the investigated material with monoenergetic soft X-rays and subsequent analysis of the photoemitted electrons. A spectrum is obtained plotting the number of detected electrons versus their kinetic or binding energies. Taking into account that every element has unique binding energy values, the spectrum of a composite material is constituted by the peaks belonging to the constituent elements [123]. Generally, a wide XPS scan is used for qualitative analysis to identify the elements present in the sample as well as for the calculation of their relative concentrations. High resolution scans are acquired to obtain accurate peak positions, chemical bonds and peak areas for quantification of chemical bonding states [124]. An important advantage of XPS is the ability to determine the chemical environment of the atoms present in a sample. This environment, including factors like nearest neighbours and the oxidation state of the element, affects the binding energy of the photoelectron peaks [125].

In our studies, the chemical composition of the fabricated electrodes was investigated using a Phoibos 150 electron energy analyser from SPECS operated in a constant energy mode. The system used the aluminium anode (Al $K\alpha$ 1486.74 eV) as a monochromatic X-ray source. The measurements were performed in ultra-high vacuum ($\approx 10^{-7}$ Pa). Typically, wide spectra over 1500 eV binding energies were acquired using 50 eV analyser pass energy. High resolution spectra were commonly recorded over 20 eV ranges at 10 eV pass energy with an energy resolution of 0.7 eV. The measurements were carried out in the National Institute of Materials Physics in Măgurele (Romania).

2.2.5 Fourier-transform Infrared Spectroscopy (FTIR)

Fourier-transform Infrared Spectroscopy (FTIR) is a technique that studies the interaction of infrared radiation with matter. In particular, this technique is used to identify chemical bonding states and functional groups of the materials. The infrared spectra are the result of the transition between molecular quantized vibrational energy states such as stretching, rotation and bending. Different materials containing covalent bonds absorb electromagnetic radiation in the IR region. However, for the determination of functional groups, the materials need to be IR active, containing molecules with net dipole moment. When this radiation interacts with covalent bonds the molecule absorbs energy and the bond starts oscillating, each bond having its particular natural vibrational frequency [126, 127].

Due to the scarce quantity of material deposited on the substrates surface, conventional FTIR systems did not allow to obtain intense high signal to noise spectra. Thus, Synchrotron-based Fourier-transform Infrared Microspectroscopy (SR-FTIRM) was used to study the chemical composition of the layers. These analyses were performed at the IR beamline MIRAS of ALBA Synchrotron using a Hyperion 3000 microscope coupled to a Vertex 70 spectrometer (Bruker, Germany). The microscope was equipped with a liquid nitrogen cooled $50\ \mu\text{m}$ mercury cadmium telluride (MCT) detector. A $36\times$ Schwarzschild objective ($NA = 0.52$) was used and all the spectra were collected in the trans-reflection mode using a single masking aperture with a size of $10 \times 10\ \mu\text{m}^2$. The spectra were registered in the $4000 - 600\ \text{cm}^{-1}$ spectral range at $4\ \text{cm}^{-1}$ spectral resolution with 1024 scans per spectrum.

2.2.6 Raman Spectroscopy

Raman spectroscopy is an alternative to FTIR technique and a complementary way to measure vibrational states of the materials. In this technique the sample is illuminated with a monochromatic radiation. The interaction of the photons with the sample causes the molecule potential energy to increase to a virtual state above the ground one. Most molecules return

rapidly to their ground state emitting a photon of the same wavelength as the incident photon. This elastic scattering is referred as *Rayleigh scattering*. However, a small fraction of the excited molecules returns to a different excited vibrational state than the ground, emitting a photon with different wavenumber, by inelastic scattering. This process is known as *Stokes Raman scattering*. Moreover, some molecules in an excited vibrational state can be elevated to a virtual level and returned to the ground state, resulting in Raman bands at wavelength higher than that of the laser. These processes, much weaker than Stokes scattering, are known as *anti-Stokes scattering*. The recording of the Raman spectrum over a wavenumber range allows for the investigation of all Raman-active vibrational bands of the molecules [126].

The Raman spectroscopy measurements were performed in air with a home-built optical set-up consisting of a 532 nm wavelength DPSS laser with 2 MHz linewidth (Cobolt - Samba), which is focused on the sample through a microscope objective (Olympus MPLFLN-BD, $\times 50$, $NA = 0.8$) to a spot smaller than 1 μm . The spectra were acquired in backscattering configuration using a 750 mm spectrometer equipped with 600 lines per mm gratings (Shamrock SR-750), and a EM CCD (Andor Newton) at the Consiglio Nazionale delle Ricerche - Istituto Officina dei Materiali (CNR-IOM) in Trieste (Italy) in the frame of a NFFA-Europe project.

2.3 Electrochemical Characterization

Several techniques have been applied to characterize the electrochemical performance of the fabricated electrodes. These techniques are based on three fundamental parameters (voltage, current and time), allowing the estimation of other metrics, such as capacitance, equivalent series resistance, time constant as well as energy and power densities. In addition, these methods can be used also to identify the storage mechanisms of the materials.

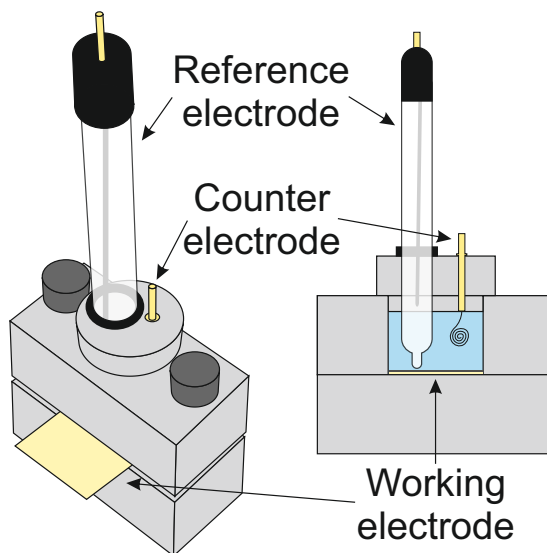


FIGURE 2.6: Diagram of the electrochemical cell used for the analyses with aqueous electrolyte.

For this purpose, the samples deposited over stainless steel or Au-coated polypropylene (PP) were used as working electrodes in a three-electrode configuration test cell. It is crucial the selection of a non-reactive substrate for these tests to avoid its electrolysis. The electrochemical analyses were performed over a sample area of 0.5 cm^2 using a plate material electrochemical cell from BioLogic, and Ag/AgCl reference electrode (3M KCl internal solution), a Pt wire counter electrode and 1M Na_2SO_4 aqueous solution as electrolyte at room temperature, as it is outlined in Fig. 2.6. The symmetric devices assembled were tested in a two-electrode configuration without using a reference electrode. The electrodes were separated by glass microfiber filter paper (Prat Dumas) impregnated with the same electrolyte from the single electrode measurements. A few *cm* long copper contacts were attached to the current collector and the system was sealed with plastic film using an impulse heat sealer type IS300C (Pacplus). Cyclic voltammetry (CV), Galvanostatic Charge-Discharge (GCD)

and Step Potential Electrochemical Spectroscopy (SPECS) tests were performed using a Keithley 2450-EC Electrochemistry Lab System. Electrochemical Impedance Spectroscopy (EIS) measurements were carried out using a Hioki IM3590 chemical impedance analyser.

Additional electrochemical measurements were conducted with an organic electrolyte. The 99.8% pure acetonitrile (ACN) solvent was purchased from Sigma-Aldrich. A molecular sieve from CWK with a 3 Å pore size was added to reduce the water content down to 20 ppm. The tetraethylammonium tetrafluoroborate (TEABF₄) salt was supplied by IoLiTec (Germany) and dried in a vacuum glass oven at 120 °C and 1×10^{-2} mbar for 24 h before use. The study has been achieved using the electrolyte 1 M TEABF₄ in ACN, displaying a water content lower than 20 ppm. Electrodes with mass loading of the active material over 30 mg cm^{-2} were fabricated as self-standing electrodes for counter electrodes of the films under study. The electrodes were composed of active carbon (Supra DLC 50, 85 wt%) as active material, conductive agent (Super C65, Timcal, 10 wt%) and binder (Polytetrafluoroethylene, PTFE, Sigma Aldrich) [128].

These electrochemical investigations were performed using Swagelok-type cells with a two- or three-electrode set-up. In the three-electrode configuration, a Ag wire was used as reference electrode. The cells were assembled in a LABmaster pro glove box (MBRAUN) filled with Ar and a content of H₂O and O₂ below 1 ppm. The cells were assembled using either two identical electrodes (symmetrical cell) or with the electrode under study facing the AC electrode with high mass loading. A 520 μm Whatman glass fibre disk, soaked with 120 μL of electrolyte, was used as separator. The electrochemical measurements with the organic electrolyte were conducted with an Arbin LBT21084 and a BioLogic VMP-3 equipment located at the Center for Energy and Environmental Chemistry (CEEC) and the Friedrich-Schiller-Universität Jena (Germany).

2.3.1 Cyclic Voltammetry (CV)

CV test consists in the application of an electric potential linearly changing with time between reference and working electrodes for three-electrode

configuration and between positive and negative electrodes for a two-electrode system. The potential change is performed at a constant rate and it is designated as the sweep rate (or scan rate), v . The potential range where the test is executed is called potential window. Generally, a closed cycle between the initial and final potentials is carried out. During the test, the current is recorded for the electrochemical characterization. The data are plotted as current vs. potential, called *voltammograms* [129]. From the voltammograms, the capacitance at different scan rates can be calculated using

$$C = \frac{\oint_S I(V) dV}{2\Delta V v \Pi} \quad (2.3)$$

where the integral represents the area enclosed in the voltammogram (anodic-cathodic charges), ΔV is the potential window, v is the scan rate and Π represents the dimensional parameter for normalization, which could be the surface area, volume or mass of active material.

As previously mentioned, the material storage mechanism can be distinguished using the CV measurements data. In surface-dominant reactions, the response current varies linearly with v . By contrast, processes controlled by semi-infinite diffusion (bulk) are proportional to the square root of v [29]. Therefore, the current can be expressed as

$$i(v, V) = i_{cap} + i_{diff} = k_1 v + k_2 v^{1/2} \quad (2.4)$$

Taking this into account, k_1 and k_2 constants can be determined from the fitting of $i(v, V)/v^{1/2}$ vs. $v^{1/2}$, hence differentiating the capacitive current contribution from that of diffusion-controlled processes.

2.3.2 Galvanostatic Charge-Discharge (GCD)

In contrast with CV test, GCD measurement is based on holding the current constant at a determined value, recording the voltage change in time. It consists on consecutive charging and discharging cycles of the electrodes and SC devices. For the charging process, a constant current is applied until the maximum voltage is reached. Then, the current is reversed to

discharge the system until the minimum voltage. The maximum and minimum voltages correspond to the potential window applied to the electrochemical cell and depend on the structure and composition of both the electrode and electrolyte [11]. For SCs, the capacitance can be obtained from the GCD data using

$$C = \frac{i \Delta t_{disch}}{\Delta V \Pi} \quad (2.5)$$

where i is the applied current, Δt_{disch} is the discharge time, ΔV is the voltage window range and Π represents the dimensional parameter for normalization. The calculated capacitance values should be similar to the values obtained from the CV data for comparable current values applied.

Subsequent charge-discharge cycles can be applied to evaluate the real performance of the fabricated devices. Through the comparison of the capacitance values measured during subsequent cycles and the initial one, capacitance retention can be determined. The coulombic efficiency ($i \cdot \Delta t_{disch} / i \cdot \Delta t_{charge}$) gives information about leakage current changes upon cycling. The performance metrics most relevant for end applications are the energy and power densities. The energy density accounts for the amount of electrical energy stored, whereas power density is related to the charging/discharging rates, i.e. energy uptake and delivery [130]. These metrics can be calculated from the capacitance C , following

$$E = \frac{1}{2} C \Delta V^2 \quad (2.6)$$

$$P = \frac{E}{\Delta t_{disch}} \quad (2.7)$$

where E is the energy density in units of $Wh\ kg^{-1}$ or $Wh\ cm^{-3}$, ΔV is the potential window, P is the power density in units of $W\ kg^{-1}$ or $W\ cm^{-3}$ and Δt_{disch} the discharge time. It has to be taken into account that equation (2.6) should only be used when a nearly linear dependence of charge within the potential window is measured.

Additional investigation for the stability of the assembled cells was performed utilizing float test at room temperature for 180 h. The potential is maintained at the maximum of the voltage window for a determined time, followed by 50 charge/discharge cycles between 0 V and the applied float voltage using a constant applied current density.

2.3.3 Electrochemical Impedance Spectroscopy (EIS)

EIS test measures the impedance of the electrochemical cell or the supercapacitor device by the application of a low-amplitude alternating current signal (around 5 mV) in a range of frequencies. The data can be represented in a Nyquist plot where the real and imaginary parts of the impedance are expressed on the complex plane, or in a Bode plot to show the response of the phase or module in function of the frequency.

For extracting technical parameters of the device, an equivalent circuit that describes the behaviour of the impedance response can be fitted. For that, simple elements such as resistors, capacitors, inductances, Warburg elements and constant phase elements (CPE) are used. The main components used in SCs are described by the following equations,

$$Z_R(\omega) = R \quad (2.8)$$

$$Z_{CPE}(\omega) = \frac{1}{Y(j\omega)^n} \quad (2.9)$$

$$Z_W(\omega) = \frac{A_W}{\omega^{1/2}}(1 - j) \quad (2.10)$$

where ω is the angular frequency and j is the imaginary unit. The resistor R contributes to the real part of the impedance. CPE is an element used for modelling the response of non-homogeneous systems. It is determined by two parameters: Y and n . Y becomes equal to capacitance when $n = 1$ (ideal capacitor). These components are employed for representing moderately distorted capacitances. Warburg (W) element represents the

impedance of semi-infinite diffusion, where A_W is the Warburg coefficient ($\Omega s^{-1/2}$).

Through the combination of these elements, a large number of complex curves can be accurately fitted [131]. The equivalent circuit is used to elucidate the storage mechanisms, to estimate the equivalent series resistance (ESR) or the relaxation time constant [11].

2.3.4 Step Potential Electrochemical Spectroscopy (SPECS)

SPECS is an electrochemical method that involves the application of a sequence of small potential steps, E_S , over the potential window, ΔV , of the device under study. The application of each potential step is followed by a rest time, t , to allow the electrode to reach quasi-equilibrium, as it is depicted in Fig. 2.7. During this time, the flowing current is measured. The modelling of the data is employed to estimate the contribution of EDL and pseudocapacitance charge storage as well as bulk diffusion processes. In a typical i - t response, the current decays quickly to almost zero after reaching a maximum value, repeating this process for each potential step [132].

After an incremental change of the electrode's potential, different processes can occur at the electrode/electrolyte interface. The charge carriers accessing the electrode's surface from the electrolyte can either contribute to surface processes, both EDL and pseudocapacitance, or suffer redox processes along with diffusional processes [129]. In order to differentiate the contribution of each process, the SPECS data is fitted for each i - t response with the aid of a mathematical model.

EDL and pseudocapacitive materials charge is a fast process and decays quickly after an applied potential, E_S . The current response for this mechanism is given by [129, 132, 133]

$$i_{cap} = \frac{E_S}{R_S} \exp\left(-\frac{t}{R_S C_C}\right) \quad (2.11)$$

where R_S is the series resistance, C_C is the EDL capacitance and pseudocapacitance, and t is the time after the potential step. Moreover, diffusion limited processes are slower than EDL and pseudocapacitive mechanisms due

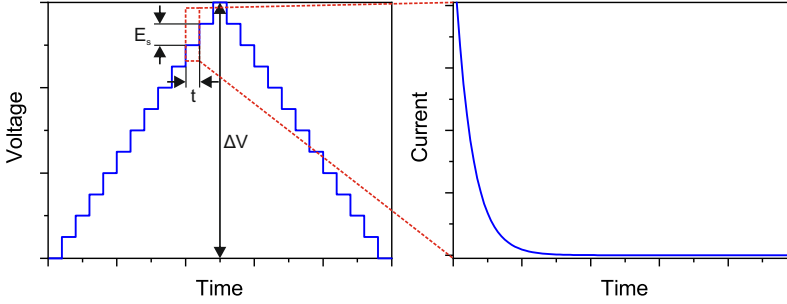


FIGURE 2.7: Example of voltage steps performed for a SPECS measurement and depiction of a current response of one of the steps.

to slower kinetics associated to bulk redox reactions [134]. Consequently, this current response can be modelled using the Cottrell equation for semi-infinite planar diffusion

$$i_{diff} = nFA\Delta C \left(\frac{D}{\pi t} \right)^{1/2} = \frac{B}{t^{1/2}} \quad (2.12)$$

where n is the number of electrons involved in an electrode reaction, F is the Faraday constant, A is the electrode area, D is the diffusion coefficient of the species, ΔC is the concentration change of the species intercalated into the host structure, and B is a proportionality constant [129].

Although the current is expected to reach zero to accomplish the equilibrium, this is not the real case scenario as a result of the existence of slow rate residual processes that do not reach equilibrium [133]. Hence, this residual current (leakages) should be added to the global SPECS model to represent the total current. Finally, the total current of SPECS data can be given by

$$i_T = i_{cap} + i_{diff} + i_{res} = \frac{E_S}{R_S} \exp\left(-\frac{t}{R_S C_C}\right) + \frac{B}{t^{1/2}} + G \quad (2.13)$$

where R_S , C_C , B and G are the fitting parameters, obtained by linear least squares regression.

Chapter 3

Nanocarbon-based electrodes with NiO

This chapter will be focused on the development of carbon-based electrodes fabricated with RIMAPLE technique. Electrodes composed of rGO as well as rGO and NiO nanoparticles will be studied by means of morphological, structural and electrochemical measurements. After this preliminary study, different pathways will be followed to enhance their electrochemical performance. Nitrogen-containing precursors will be added to the target dispersion containing GO platelets and NiO nanoparticles. The studies will be concluded with electrochemical capacitor devices fabrication. The addition of MWCNT to the rGO-NiO composite will be also investigated. The different mechanisms contributing to the capacitance increase by nitrogen-doping and MWCNT addition will be determined, based on morphological, compositional and electrochemical measurements.

3.1 Electrodes composed of rGO and NiO NPs

The targets for RIMAPLE deposition are composed of a dispersion of GO sheets and a mixture of GO sheets with NiO NPs homogeneously dispersed in distilled water. A liquid nitrogen cooled holder maintained the target dispersion frozen at a temperature of about 200 K. The solid ice water matrix is transparent to the incident laser radiation. Although the optical absorption is slightly higher in solid than in liquid water due to ice

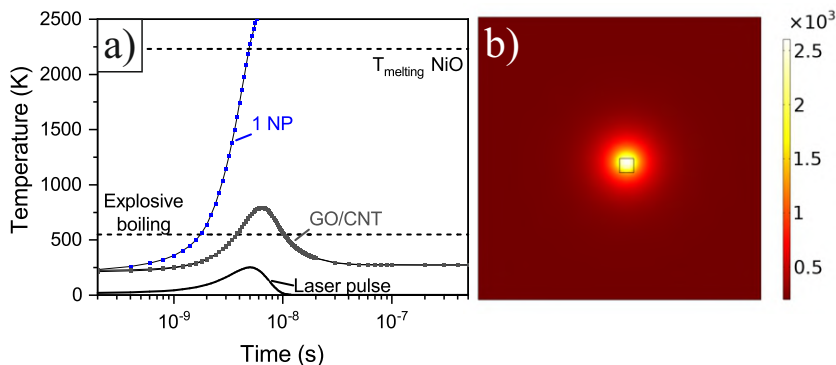


FIGURE 3.1: (a) Simulated temperature of a NiO NP and carbon nanostructures during laser irradiation at 0.4 J cm^{-2} laser fluence and (b) temperature map of single NP at 5 ns from the start of the laser pulse.

imperfections, entrapped air bubbles, cracks and other defect, the minor increment in absorption cannot explain the ablation process [108]. Therefore, the laser radiation is absorbed by the materials of interest dispersed in the ice matrix. Different mechanisms take place when the target is exposed to the laser light, including photochemical processes, which directly break chemical bonds, and photothermal interactions, which are brought on by the thermalization of excited electrons with longer interaction times than photochemical processes [135]. Previous research demonstrated that UV light can photochemically reduce GO solutions [77]. Considering that the threshold for GO photo-induced reduction was determined to be 3.2 eV [77], the use of 266 nm wavelength laser radiation, corresponding to 4.7 eV photon energy, is assumed to drive the photochemical GO reduction [136] even though photothermal processes also occur. Regarding the graphitic domains of GO, the main process is considered to be photothermal due to the lack of enough photonic energy to break $\text{C}=\text{C sp}^2$ bonds (6.4 eV) [137]. Both σ and π -bonded electrons, constituent of graphene structures, are excited by UV radiation, which causes their fast heating [138]. Furthermore,

TABLE 3.1: Relative concentration of precursors in the aqueous dispersions for RIMAPLE targets composed of GO and NiO NPs.

Target dispersion	Composition
GO5%	5 wt% GO
GO9%	9 wt% GO
GO5%-NiO2%	5 wt% GO, 2 wt% NiO NPs
GO5%-NiO5%	5 wt% GO, 5 wt% NiO NPs
GO9%-NiO9%	9 wt% GO, 9 wt% NiO NPs

the bandgap of 4.3 eV of the NiO NPs [139] allows the excitation of electrons to produce significant heating by electron-phonon scattering. Photochemical processes can also occur as there is enough energy for breaking the Ni – O bond [140].

Previous works thoroughly studied the mechanisms occurring during UV laser irradiation of GO, MWCNT and NiO NPs [109, 141]. Here, simple photothermal simulations were performed through numerical simulations using COMSOL Multiphysics to explain the processes involved during deposition (Appendix A). Considering the thermophysical and optical properties of GO [109] and NiO [142, 143] (Table A.1), the temperature evolution was simulated upon a single pulse irradiation with a pulse duration of 5 ns (Fig. 3.1a). As previously stated, water ice is transparent to UV radiation. Hence, the nanocarbon materials and the oxide NPs absorb all the radiation, being rapidly heated. As witnessed in Fig. 3.1a, the carbon nanomaterials and the NiO NPs irradiated with a 266 nm laser pulse with 0.4 J cm^{-2} laser fluence leads to a rapid temperature increase up to *ca.* 800 K in nanocarbons and beyond 2230 K (melting point) in NiO NPs in just a few *ns*. The heat released by these nanostructures leads to the explosive boiling of the surrounding water ice resulting in the deposition of material onto the facing substrate [109, 144]. The laser-induced chemical reactions will cause the reduction of GO to rGO [109], and the thermally-driven melting and resolidification of the NiO NPs, leading to their recrystallization to

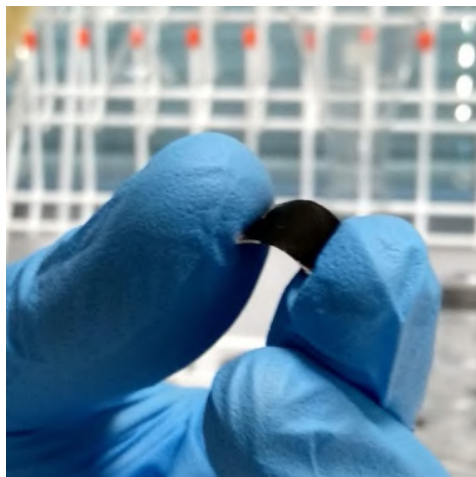


FIGURE 3.2: Electrode layer deposited over PP film coated with sputtered Au/Cr.

metal oxide nanostructures. Table 3.1 presents the different target dispersions containing GO powder and NiO NPs in various concentrations used for the preparation of the electrode layers. The electrodes were deposited after the accumulation of 6000 pulses (i.e. 10 minutes of irradiation time) under the experimental conditions described in Chapter 2.

3.1.1 Morphological characterization

The deposited films are adherent to the substrate, flexible and show homogeneous dark brown – black colour independently on the target composition (Fig. 3.2). The deposited rGO layers present a film thickness in the 100–500 *nm* range, whereas the rGO-NiO films are thicker, about 2.3–8.6 μm . The large difference of thickness between rGO and rGO-NiO films is due to the absorption of the laser radiation by the NiO NPs and subsequent heating of the surrounding water-ice matrix. This temperature rise leads to a more extensive vaporization of the matrix causing the deposition of a larger amount of material as compared to pure GO target, as deduced from the photothermal simulations (Fig. 3.1).

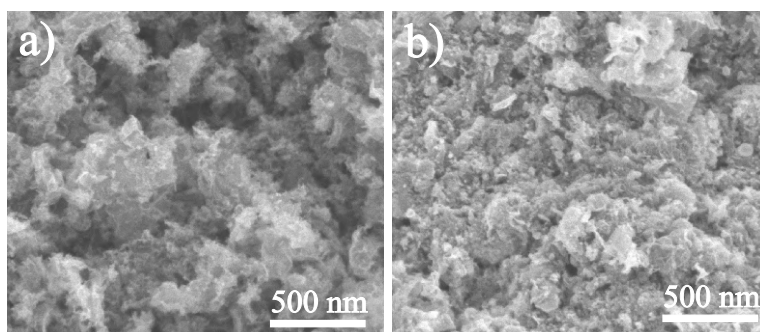


FIGURE 3.3: XHRSEM images of (a) GO9% and (b) GO5% - NiO5% electrodes.

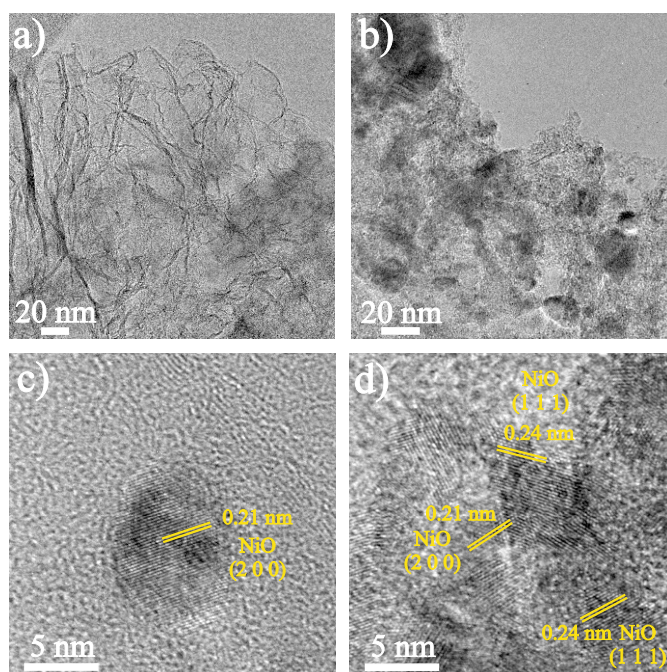


FIGURE 3.4: HRTEM images of electrode (a) GO9% and (b), (c) and (d) of GO5% - NiO5% in different regions.

Representative SEM images of the deposited films are shown in Fig. 3.3. The rGO films exhibit a rough surface morphology composed of an homogeneous distribution of irregular-shaped wrinkled rGO flakes (Fig. 3.3a). The formation of these wrinkles in rGO sheets after irradiation with nanosecond UV laser has been previously observed [145]. The origin of this deformation is attributed to the steady deformation of the GO sheets prompted by the creation of structural defects. The rGO-NiO films show a similar morphology with tens of nm-sized visible droplets (Fig. 3.3b). These particulates are not observed in rGO films, hence they may be ascribed to NiO nanostructures. HRTEM analyses of the deposited films reveal highly crumpled graphene oxide flakes with irregular edges (Fig. 3.4a). The analyses for the rGO-NiO films confirm the presence of nm sized round nanostructures over the wrinkled rGO flakes (Fig. 3.4b). Higher magnification images reveal nanostructures that are ascribed to cubic NiO (JCPDS 00-047-1049) showing domains with interplanar distances of 0.21 and 0.24 nm assigned to (200) and (111) crystallographic orientations, respectively.

3.1.2 Electrochemical characterization

The electrochemical properties of the rGO and rGO-NiO electrodes deposited on Au/Cr/PP substrate were studied by CV measurements in aqueous 1 M Na₂SO₄ electrolyte solution. Fig. 3.5a and b show the voltammograms at 100 mV s⁻¹ of GO9% and GO5% – NiO5%, respectively. Using equation (2.4), the capacitive contribution from the total current can be determined as highlighted in the figures. The peak recorded at the highest potential is caused by the oxygen-evolution reaction at the aqueous electrolyte. In general, the films deposited with NiO NPs reach current densities higher than those of the films composed of GO only in the target, independently on their relative concentration. As a representative electrode, voltammograms of the GO5% – NiO5% film at different sweep rates in the range 10 mV s⁻¹ – 150 mV s⁻¹ are presented in Fig. 3.5c. The rectangular-like shape without any redox peak together with the main contribution of capacitive current, points to the capacitive processes as main charge

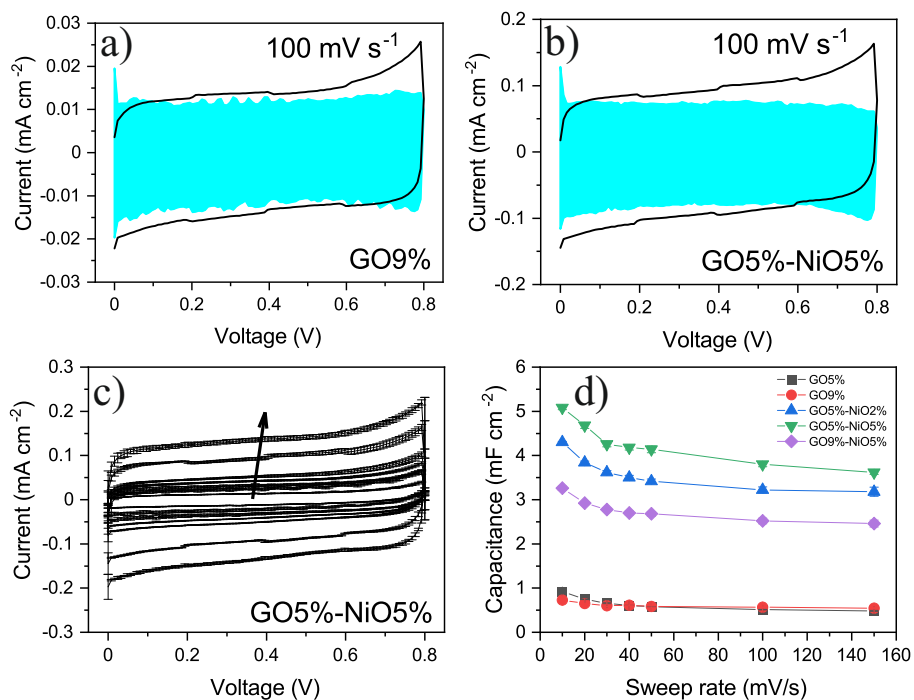


FIGURE 3.5: CV of the electrodes (a) GO9% and (b) GO5% – NiO5% at 100 mV s^{-1} with surface capacitance contribution highlighted in blue; (c) CV curves of sample GO5% – NiO5% at sweep rate range of 10 mV s^{-1} – 150 mV s^{-1} (arrow indicates the increasing sweep rate); (d) areal capacitance *vs.* sweep rate of the fabricated electrodes.

storage. Considering this behaviour, the surface capacitance can be determined from CV data using equation (2.3). The films composed of only rGO have similar surface capacitance values independently on the GO platelets concentration in the target dispersion, reaching *ca.* 1 mF cm^{-2} @ 10 mV s^{-1} . The addition of NiO NPs increases the surface capacitance. The addition of 2 wt% and 5 wt% NiO NPs to the 5 wt% GO dispersion leads to an increase of the surface capacitance to 4.3 mF cm^{-2} and 5 mF cm^{-2} @ 10 mV s^{-1} , respectively. However, for 5 wt% NiO NPs and 9 wt% GO the capacitance slightly decreases. It is important to emphasize that this comparison is

performed considering the surface capacitance instead of volumetric capacitance due to the large difference of thickness values. Although rGO electrodes with submicrometric thicknesses may exhibit greater volumetric capacitance values than rGO-NiO electrodes, such thin electrodes cannot be scaled up without losses because microstructural rearrangements obstruct the electrolyte diffusion and its interaction with the active material [146].

NiO-containing electrodes would exhibit additional charge storage processes as a result of oxidation of NiO to NiOOH (charging) and reduction of NiOOH to NiO (discharging), as it is described in the following reaction [147]



being z the fraction of nickel (III) sites. EDL and pseudocapacitance charge storage are surface processes by nature. The structure-morphology of the electrode material, however, can also lead to diffusion-limited (semi-infinite or bulk) electrochemical processes. As a result, complex systems composed of different types of nanomaterials can display pseudocapacitance (surface) or battery-like (bulk) behaviour even having the same chemical composition. For instance, NiO-based nanomaterials have been reported to exhibit different electrochemical behaviour depending on their nanostructure (extrinsic pseudocapacitive material) [147–150]. The dominance of capacitive processes with lack of redox peaks in the electrodes fabricated containing NiO NPs have been proven (Fig. 3.5b). This fact could indicate that either NiO nanostructures located on the surface of rGO sheets expand the distance between rGO sheets, increasing the effective surface exposed to the electrolyte (increment of porosity) and showing limited diffusive behaviour, or NiO nanostructures exhibit pseudocapacitive nature due to their small size.

TABLE 3.2: Relative concentration of GO, NiO NPs and imidazole precursors in the aqueous dispersions used in the RIMAPLE targets.

Target dispersion	Composition
GO-imi	5 wt% GO, 5 wt% imidazole
GO-NiO-imi	5 wt% GO, 5 wt% NiO NPs, 5 wt% imidazole

3.2 Nitrogen-doping of rGO and rGO-NiO electrodes

The electrochemical performance of the former fabricated films can be improved by means of incorporation of nitrogen groups in carbon materials. This enhancement can be achieved by the addition of nitrogen-containing precursors in the initial target dispersion. These groups can undergo reversible redox reactions, besides enhancing electron donor capability and wettability [151]. Imidazole is an aromatic nitrogen-containing compound with unique biological and pharmaceutical applications [152]. The highly polar nature of imidazole makes it susceptible to establish non-covalent bonds. Recent studies using UV laser radiation have proved the effectiveness of imidazole molecules as N-doping agent of GO [153]. Furthermore, the formation of N-doped graphene through thermal annealing of imidazole has been demonstrated [154]. Therefore, RIMAPLE deposition of GO in the presence of imidazole is expected to induce large N-doping of rGO. Two different sets of electrodes were prepared combining GO and imidazole in the RIMAPLE targets, with and without NiO NPs, using the same laser parameters as for the undoped rGO and rGO-NiO samples. The relative concentration of GO, NiO and imidazole in the aqueous dispersions are presented in Table 3.2.

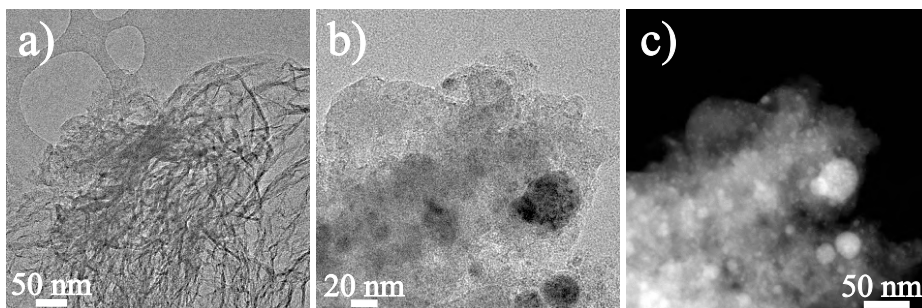


FIGURE 3.6: (a) TEM image of GO-imi sample; (b) TEM and (c) corresponding HAADF-STEM images of the same location in the GO-NiO-imi sample.

3.2.1 Morphological characterization

Under visual inspection, the doped films present similar appearance as the undoped counterparts, characterized by a uniform black colour. Moreover, SEM images do not show any differential feature to their counterparts without imidazole precursor. TEM analyses reveal that the GO-imi film shows higher density of wrinkles in the rGO flakes (Fig. 3.6a) and larger quantity of nanoholes. The formation of a high quantity of wrinkles and nanoholes was previously observed in RIMAPLE deposition of GO flakes in the presence of N-containing precursors as ammonia, urea and melamine molecules [141]. These results would point out that molecules containing nitrogen functional groups, as imidazole, induce high reactivity and subsequent structural alterations to the GO flakes during the UV laser irradiation process. Importantly, it is hypothesised that the existence of defects in the form of nanoholes will help create electrolyte diffusion channels and interact with edge atoms, which are more electrochemically active than basal ones [155, 156]. TEM and HAADF-STEM analyses of GO-NiO-imi film (Fig. 3.6b and c, respectively) reveal that the rGO surface is highly covered by nanometric crystals. HRTEM image shows the presence of a large amount of nanostructures with dimensions ranging from 1 nm to few tens of nm. The corresponding HAADF-STEM image, in which the intensity is strongly related to the atomic number, reveals that these crystals

are indeed composed of NiO (Ni-rich regions appear brighter). These NiO nanostructures are substantially smaller than the initial NiO NPs (50 nm) suggesting the development of melting-dewetting-recrystallization mechanisms during the laser irradiation-deposition process.

3.2.2 Compositional characterization

The composition of the deposited films is studied via wide scan and high resolution XPS. Fig. 3.7a shows the survey of the GO-NiO-imi film, in which C, O, Ni and N peaks are clearly identified. The wide scan spectra were used to calculate the atomic concentration of the chemical elements present in the raw GO and N-doped films, besides previous undoped GO (GO9%) and GO-NiO (GO9% – NiO5%) films for comparison. Fig. 3.7b and c display the calculated reduction degree ($at.\%C/at.\%O$ ratio) besides the nitrogen doping degree ($100 \times at.\%N / (at.\%N + at.\%C)$) of all samples. It is important to note that due to the presence of Ni and O atoms from NiO in the GO-NiO samples, the concentration of C, O and N in rGO material has to be recalculated (filled bars in Fig. 3.7b) from the measured data (open bars). Being the total atomic quantities of C, O, N and Ni named as qC , qO , qN and qNi , respectively, and considering NiO material as stoichiometric,

$$qNi = qO_{NiO} \quad (3.1)$$

$$qO = qO_{NiO} + qO_{rGO} \rightarrow qO_{rGO} = qO - qO_{NiO} = qO - qNi \quad (3.2)$$

Therefore, designating $qCNO = qC + qN + qO$, the atomic concentration recorded by XPS is, by definition,

$$[C]_{XPS} = \frac{qC}{qC + qN + qO + qNi} \equiv \frac{qC}{qCNO + qNi} \quad (3.3)$$

$$[O]_{XPS} = \frac{qO}{qCNO + qNi} \quad (3.4)$$

$$[Ni]_{XPS} = \frac{qNi}{qCNO + qNi} \quad (3.5)$$

By using equation (3.2) and (3.3), the real atomic concentration in rGO, considering all the measured C and N atoms present in the rGO structure, would be

$$[C]_{rGO} = \frac{qC}{qC + qN + qO_{rGO}} = \frac{qC}{qCNO - qNi} \quad (3.6)$$

$$[O]_{rGO} = \frac{qO_{rGO}}{qC + qN + qO_{rGO}} = \frac{qO - qNi}{qCNO - qNi} = \frac{[O]_{XPS} - [Ni]_{XPS}}{1 - 2[Ni]_{XPS}} \quad (3.7)$$

$$\frac{[C]_{rGO}}{[C]_{XPS}} = \frac{qCNO + qNi}{qCNO - qNi} = \frac{1}{1 - 2[Ni]_{XPS}} = \frac{[N]_{rGO}}{[N]_{XPS}} \quad (3.8)$$

Therefore, with equation (3.7) and (3.8), $[C, N, O]_{rGO}$ can be calculated from the atomic concentrations measured by wide scan XPS.

As seen, raw-GO exhibits a low C/O ratio (approximately 2.6) and no presence of nitrogen-containing groups. The deposited films from both targets comprising GO-water and targets containing reactive imidazole molecules, show an increase of the reduction degree in all cases, confirming that the GO flakes were reduced and deposited simultaneously. The rGO-based sample with the highest reduction degree (8.6) was synthesized in the presence of imidazole molecules. The GO-NiO film obtained without reactive molecules in the target displays a C/O ratio similar to that of raw GO. GO flakes may have a laser shielding effect due to the presence of highly UV absorbing NiO NPs, which would impede the photochemical deoxygenation process. Furthermore, the presence of imidazole molecules enhance the deoxygenation process, leading to a reduction degree of 13.7. The sample deposited without imidazole molecules in the target (GO, GO-NiO) reveal a minor incorporation of N into the rGO structure with a respective N-doping degree of 2% and 3% originating from the N_2 background gas

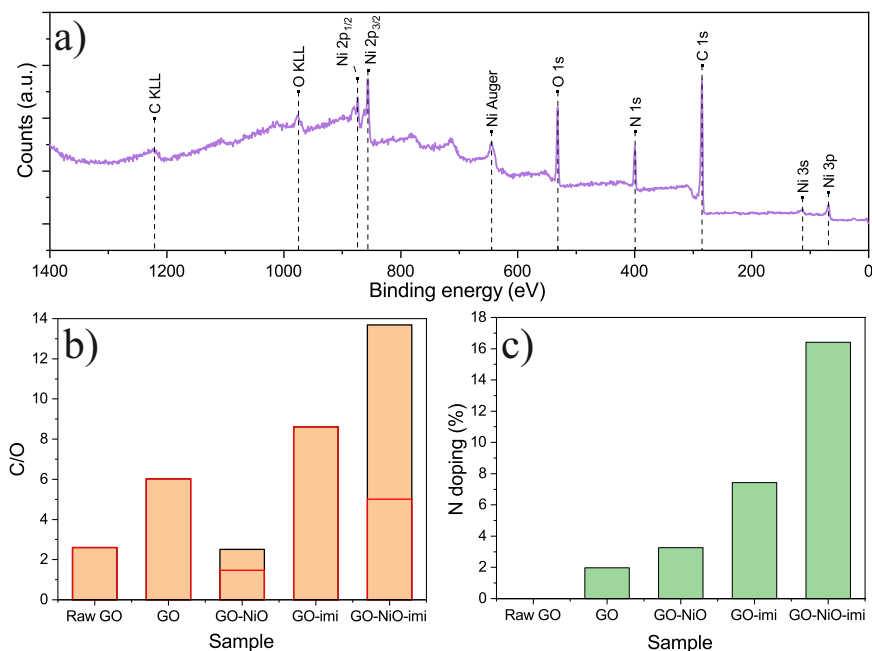


FIGURE 3.7: (a) Wide XPS spectra of electrode GO-NiO-imi, (b) reduction degree and (c) nitrogen doping degree of all fabricated electrodes. In (b), open bars are directly obtained from measurements, whereas filled bars correspond to the calculated concentration by subtraction of NiO contribution.

environment. Conversely, the samples synthesized with imidazole precursor exhibit higher N-doping degree (7% and 16% for GO-imi and GO-NiO-imi, respectively). This feature can be attributed to the decomposition of N-containing imidazole molecules and subsequent incorporation of N into the rGO structure

Representative C 1s and N 1s high resolution XPS spectra of the deposited samples are displayed in Fig. 3.8a-c, including the corresponding deconvoluted peaks. The C 1s signal is deconvoluted in five components ascribed to sp^2 -bonded carbon atoms, possibly with a minor contribution of sp^3 configuration (284.7 eV), in addition to hydroxyl (286.0 eV), epoxide (287.1 eV) and carboxylic (289.7 eV) groups [141]. The peak at 292.0 eV

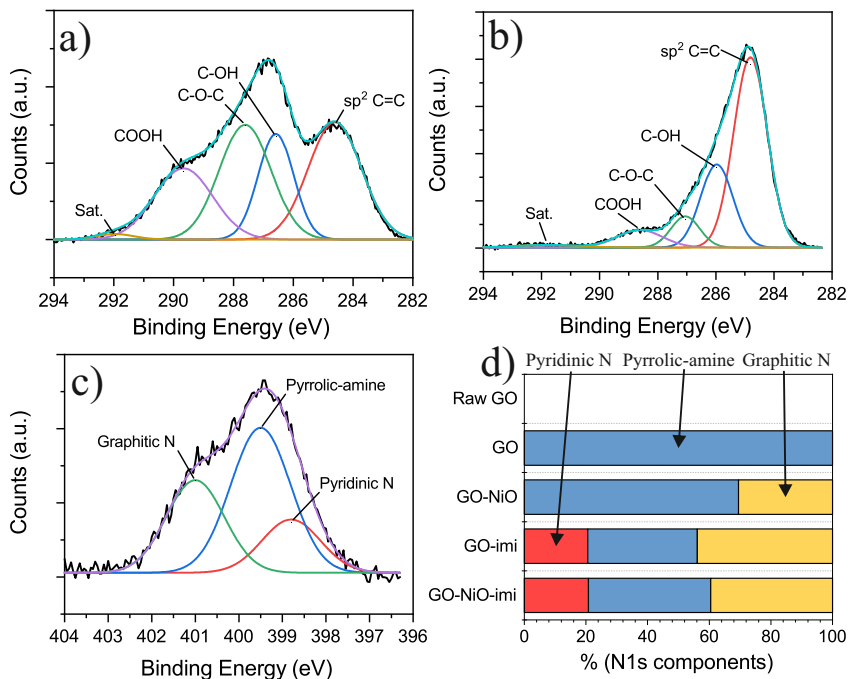


FIGURE 3.8: Deconvolution of high resolution C 1s XPS spectra of (a) raw GO and (b) GO-NiO-imi sample; (c) deconvoluted N 1s spectrum of GO-NiO-imi sample; and (d) ratio of N 1s components of the fabricated samples.

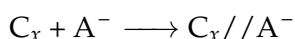
is related to a shake-up satellite caused by a π - π^* transition in graphene structure [157]. As can be observed in Fig. 3.8a and b, the relative intensity of the sp²-bonded carbon signal increases in the deposited films as compared to raw GO. This effect is a consequence of the decrease of carbon-oxygen bonds due to the reduction of deposited GO. On the contrary, the deconvolution of the N 1s spectra reveals the presence of nitrogen containing functionalities associated with pyridinic N (398.8 eV), pyrrolic-amine groups (399.5 eV) and graphitic N (401.0 eV) (Fig. 3.8c) [141]. It is worth mentioning that the contribution of pyridinic and pyrrolic N – C bonds superposes the hydroxyl and epoxide peaks of the C 1s spectrum [158]. Fig. 3.8d displays the integrated area of the N 1s deconvoluted components. GO sample exhibits the formation of pyrrolic-amine functionalities,

GO-NiO shows the presence of graphitic nitrogen besides pyrrolic-amine, and the samples developed with imidazole precursor reveal the presence of all functionalities.

3.2.3 Electrochemical characterization

The electrodes prepared with imidazole precursor were studied by cyclic voltammetry in the voltage window of 0–0.8 V and 10–150 $mV s^{-1}$ sweep rate. All the voltammograms show highly symmetric rectangular shapes without the presence of pronounced peaks (Fig. 3.9a,b). The deviation at highest potential comes from the oxygen-evolution reaction. The current densities measured for the electrode containing NiO NPs are higher as compared to those corresponding to the electrode obtained from GO-imidazole target dispersions, in the absence of NiO. No evidence of potential variation of features with sweep rate, characteristic of kinetic irreversibility, is perceived. However, a progressive symmetry deviation in the voltammograms with increasing sweep rate is observed at the voltage limits (0, 0.8 V), which is caused by kinetic limitations during the voltage reversal at each cycle. The rectangular-like shape, without marked redox peaks and the kinetic reversibility of the voltammograms point out to a capacitive behaviour (surface mechanisms) in the electrodes [159, 160].

The oxygen- and nitrogen-based functionalities contained in the N-doped rGO that constitute the electrodes would actually improve their ability to store charges. The deposited electrodes should exhibit EDL and pseudocapacitance caused by redox reactions as the two primary mechanisms of charge storage. Ideally, the formation of an electric double layer is expected at the interface between graphitic domains and electrolyte. Notably, any remaining oxygen-containing chemical groups in rGO would impart a polarity to carbon atoms, which interact with polar water molecules in the electrolyte, increasing wettability [161]. Under these conditions, the equilibrium reaction during charging at the positive electrode would be simply presented as



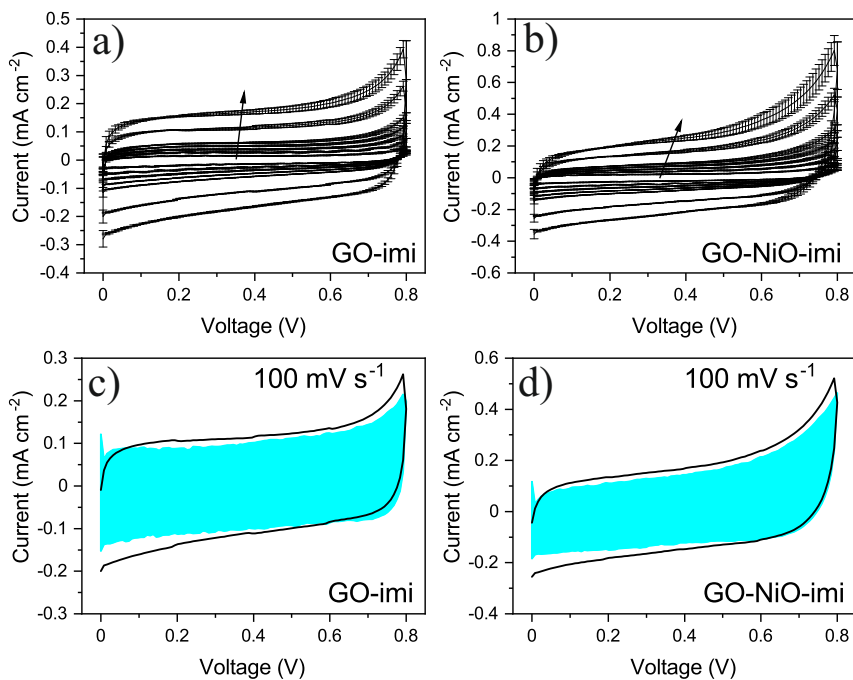


FIGURE 3.9: CV curves at sweep rate range 10 mV s^{-1} – 150 mV s^{-1} of sample (a) GO-imi and (b) GO-NiO-imi (arrow indicates the increasing sweep rate). CV of the electrodes (c) GO-imi and (d) GO-NiO-imi at 100 mV s^{-1} with surface capacitance contribution highlighted in blue.

being C_x the carbon structure of the electrode and A^- the anion molecules of the electrolyte. A negative electrode undergoes a similar mechanism, but involving cations. Additionally, nitrogen-containing chemical groups will add pseudocapacitance through several redox reactions. Pyridinic and pyrrolic nitrogen with negative charge, located at the graphene edges, were reported to have the highest influence on the capacitance as a result of the induced redox processes [162]. On the contrary, graphitic nitrogen, present within the graphene sheet, substituting C atoms, has been demonstrated to increase capacitance due to its positive charge that improves electron transfer and adds n-type nature to the material [161–166]. All of this functional

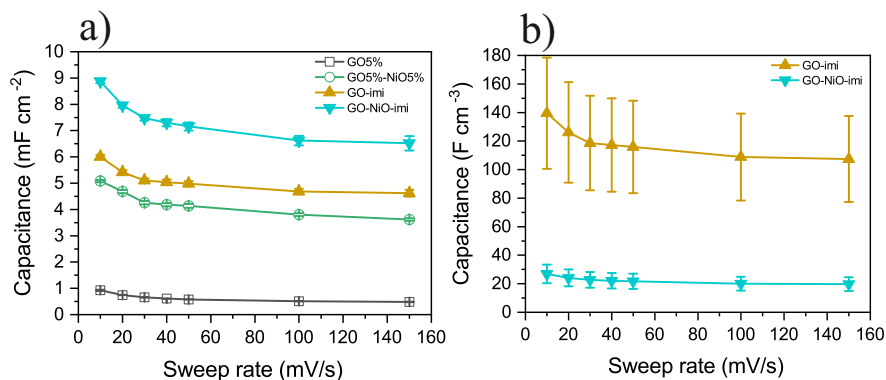


FIGURE 3.10: (a) Areal capacitance *vs.* sweep rate of the fabricated electrodes with imidazole precursor comparing with previous GO5% and GO5% – NiO5% (open symbols). (b) Corresponding volumetric capacitance *vs.* sweep rate of the N-doped electrodes.

chemical groups, besides the NiO nanostructures, would enhance the storage capability as compared to conventional rGO. Despite the formation of different redox-active species in the rGO structure, the main contribution to capacitance are surface processes, as it can be observed in Fig. 3.9c and d, where the surface capacitance contribution from the total current is calculated using equation (2.4). Taking into account the main contribution of this surface processes together with the quasi-rectangular shape of voltammograms, the surface capacitance can be determined from CV data using equation (2.3).

The areal capacitance is presented in Fig. 3.10a together with the areal capacitance values of GO5% and GO5% – NiO5% electrodes for comparison. As can be observed, the addition of the imidazole precursor increases the areal capacitance, reaching *ca.* 6 mF cm^{-2} and 9 mF cm^{-2} @ 10 mV s^{-1} for GO-imi and GO-NiO-imi, respectively. In Fig. 3.10b, the corresponding volumetric capacitance of these electrodes are calculated using the thickness values measured by SEM, $0.43 \pm 0.12 \mu\text{m}$ for GO-imi and $3.3 \pm 0.8 \mu\text{m}$ for GO-NiO-imi. The volumetric capacitance of GO-imi reaches around

$140 F cm^{-3}$ and that of GO-NiO-imi, $27 F cm^{-3}$. The higher volumetric capacitance of GO-imi electrode might be the result of the lower compactness (larger thickness) of GO-NiO-based films due to an increased distance between NiO-coated rGO sheets. Additionally, NiO, a p-type semiconductor, has been demonstrated to act as hole-transport electron blocking material in p-n junctions [167]. As previously discussed, graphitic N-doped rGO exhibits n-type behaviour. Thus, p-n nanojunctions with rectifying effect would be present in the N-doped rGO flakes coated with NiO nanostructures, which might hinder charge storage procedures. It is also worth noting that, as stated in the previous section, the performance of very thin electrodes, such as those based on rGO, should not be directly extrapolated to thicker films as they would not scale up linearly.

Galvanostatic charge discharge of both GO-imi and GO-NiO-imi electrodes at 1, 2, 4 and $8 mA cm^{-2}$ are presented in Fig. 3.11a and b, respectively. Despite the low thickness and low mass loading of the films (about few $\mu g cm^{-2}$), the corresponding specific currents are significant, about $kA g^{-1}$. The curves exhibit highly triangular profile without any plateaus, indicating a quasi-linear dependence of voltage with time, which is a distinctive behaviour of electrochemical capacitors. As can be observed, the charge/discharge time decreases as the applied current density increases. The volumetric capacitances, calculated by equation (2.5), are shown in Fig. 3.11c. Electrochemical impedance spectroscopy measurements were acquired to study the AC performance of the electrodes. Nyquist plots of GO-imi and GO-NiO-imi electrodes in a frequency range of 1 Hz to 200 kHz are presented in Fig. 3.12a. As observed, the EIS curves exhibit the characteristic behaviour of carbon-based porous electrodes containing a moderately straight line at low frequencies and a partial semicircle at high frequencies [168–170]. The curves were fitted by a modified Randles equivalent circuit shown in Fig. 3.12b and their plots are presented as continuous lines in Fig. 3.12a. This circuit contains a resistance $R1$ as equivalent series resistance (ESR), accounting for the intrinsic resistance of the electrolyte, besides electric contacts and materials of the electrode. This resistance is

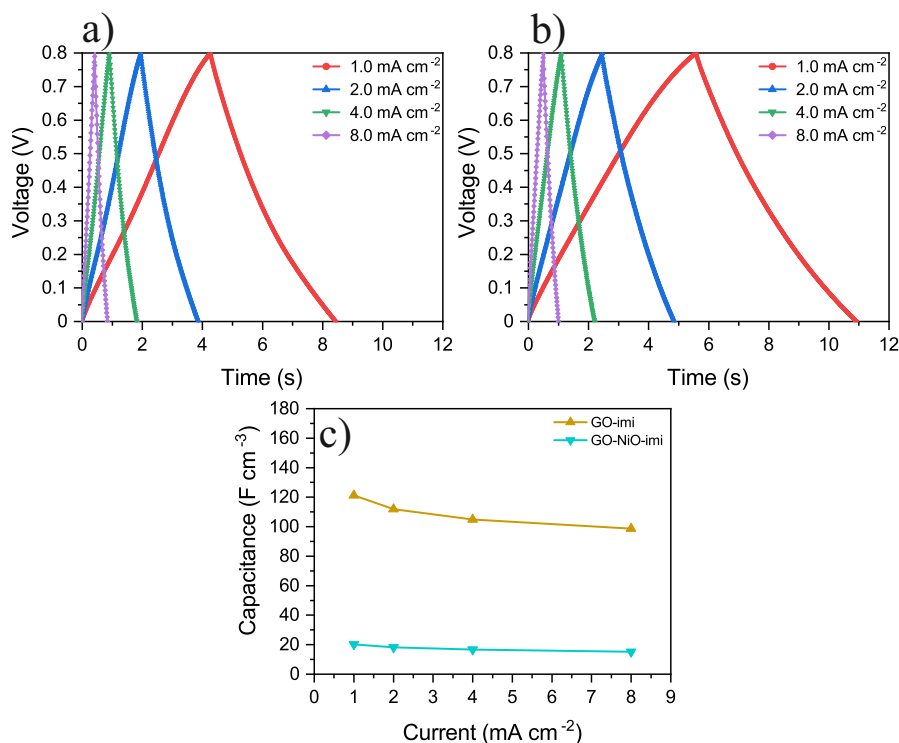


FIGURE 3.11: Galvanostatic charge–discharge data of (a) GO-imi and (b) GO-NiO-imi for different applied currents; (c) volumetric capacitance vs. applied current density of GO-imi and GO-NiO-imi.

connected in series with two CPEs in parallel configuration. $CPE1$ represents the impedance developed from the double layer charge storage processes, whereas $CPE2$ stands for the pseudocapacitance contribution generated by redox processes. A charge-transfer resistance ($R2$), related to redox processes, is placed in series to $CPE2$, and in parallel, a leakage resistance ($R3$). The fitted values for these parameters are listed in Table 3.3. Both electrodes exhibit similar ESR, around 20Ω , and $CPE1$ has lower n exponent of about 0.5–0.6 compared to $CPE2$ (0.9). The fitting of n values lower than 1 indicates that the properties of the electrodes are not homogeneous or exhibit some dispersion as highly contorted and rough surfaces, varying

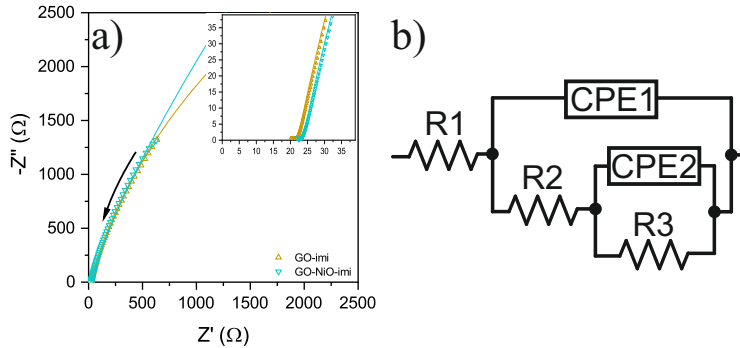


FIGURE 3.12: (a) Nyquist plot of the EIS measurement (points) and simulated data from the equivalent circuit (lines) of fabricated electrodes containing imidazole precursor (the arrow indicates the direction of increasing frequency). Inset details the high frequency range. (b) Equivalent circuit for data fitting.

TABLE 3.3: Fitting values for the elements of the equivalent circuit for electrodes with imidazole precursor.

	R1 (Ω)	R2 (Ω)	R3 (Ω)	CPE1		CPE2	
				Y (mS s ⁿ)	n	Y (mS s ⁿ)	n
GO-imi	19.6	2.9	11600	0.28	0.6	0.67	0.9
GO-NiO-imi	19.8	4.3	> 10 ⁸	0.35	0.5	0.61	0.9

thickness or composition of the film, and non-homogeneous redox reaction rates. Having n values of *CPE1* lower than *CPE2* indicates that compared to pseudocapacitive ones, double layer charge storage mechanisms are more influenced by material imperfections (dispersive features).

3.2.4 Device fabrication and performance study

The performance of GO-imi and GO-NiO-imi electrodes in working devices was examined by assembling symmetric electrochemical capacitors.

To this purpose, pairs of both GO-imi and GO-NiO-imi films were prepared (Fig. 3.13a). The voltammograms maintain the quasi-rectangular shape without the presence of prominent peaks (Fig. 3.13b). Galvanostatic charge-discharge voltage charts of the devices show the distinctive triangular-shape profile (Fig. 3.13c). As seen, the applied current density causes a reduction in the charge-discharge duration of cycles. Using equation (2.5), the corresponding volumetric capacitance of the SCs was calculated and is displayed in Fig. 3.13d. Remarkably, GO-imi SC exhibits higher volumetric capacitance than GO-NiO-imi device. GCD cycling at 1.5 mA cm^{-2} current density was also used to examine the stability of the devices. The GO-NiO-imi device disclose excellent behaviour with capacitance retention and coulombic efficiency remaining unaltered after 10000 cycles. Through mechanical strength and adhesion to the electrodes, NiO nanostructures may contribute to structural stability in these devices. However, the GO-imi SC shows a continuous fading of coulombic efficiency and can only withstand a certain number of cycles (*ca.* 5000), probably due to the considerably higher specific current density that the active material of the electrodes has to bear and lower mechanical strength, as consequence of the significant lower mass loading and the absence of NiO, respectively.

The Ragone plot shown in Fig. 3.13f, allows the evaluation of the overall performance of the SCs. The volumetric energy and power densities were calculated using equations (2.6) and (2.7), considering the total volume of active materials in the assemblies. A comparison of different energy storage devices is also presented, calculated with the total volume of the device, including the active material, the current collector and the separator with electrolyte [79, 171]. As can be observed, the GO-imi device has notably greater energy and power densities, about 4.0 mWh cm^{-3} and 6.5 W cm^{-3} , respectively, as compared to the NiO-based device. The energy density of GO-imi SC is also higher than that of commercial SCs and comparable to that of Li batteries. In terms of power density, there is a distinct advantage over Li batteries, while commercial SCs have similar power density values.

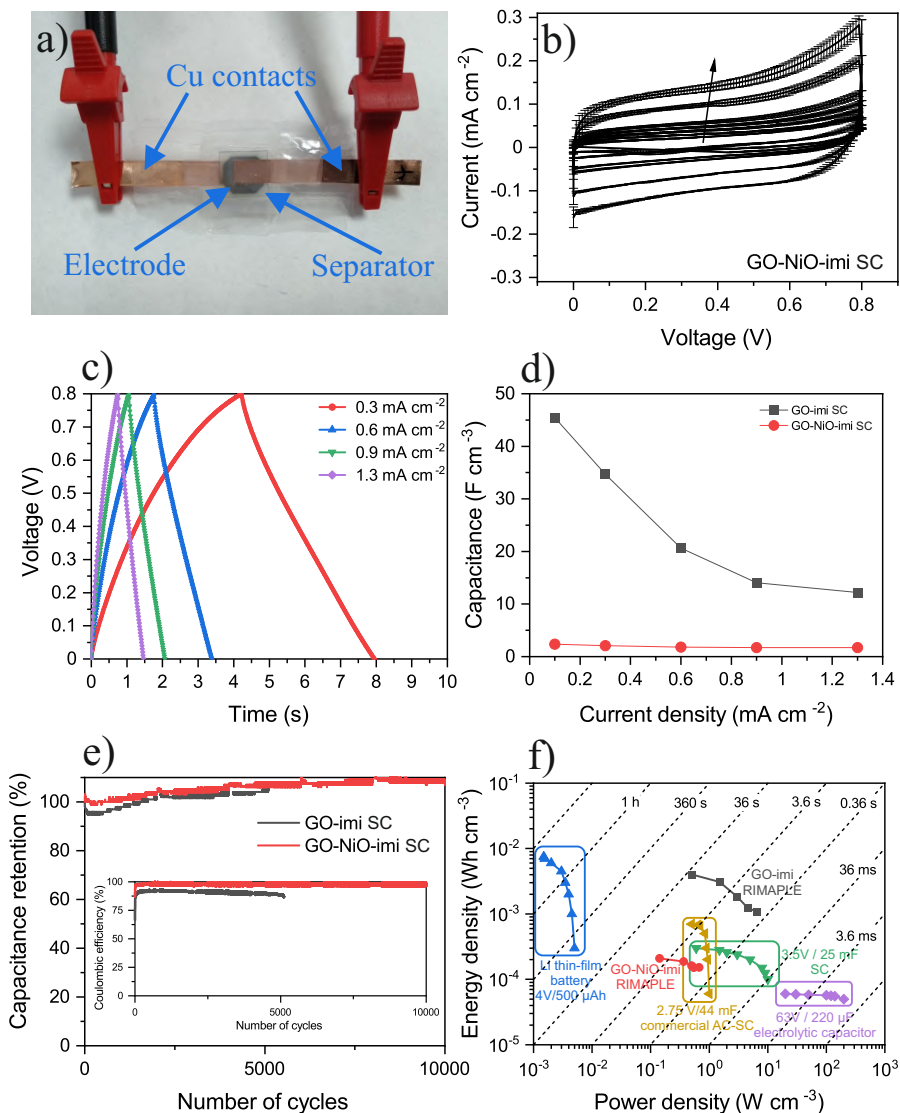


FIGURE 3.13: (a) Image of an assembled SC device. (b) CV curves at sweep rate range $10 - 150 \text{ mV s}^{-1}$ (arrow indicates the increasing sweep rate) and (c) GCD measurement of GO-NiO-imi SC device. (d) Volumetric capacitance *vs.* applied current of symmetric device GO-imi and GO-NiO-imi. (e) Capacitance retention and coulombic efficiency (inset) of both devices fabricated. (f) Ragone plot of the fabricated SC device compared with commercially available energy storage systems. Data for the lithium battery, $3.5 \text{ V} / 25 \text{ mF}$ supercapacitor (SC) and $6.3 \text{ V} / 220 \mu\text{F}$ electrolytic capacitor [171] and data for the $2.75 \text{ V} / 44 \text{ mF}$ activated carbon supercapacitor (AC-SC) [79].

TABLE 3.4: Relative concentration of precursors in the aqueous dispersions for RIMAPLE targets composed of GO, MWCNT and NiO NPs.

Target dispersion	Composition
GO-CNT-NiO-505	5 wt% GO, 5 wt% NiO NPs (No MWCNT)
GO-CNT-NiO-515	5 wt% GO, 1 wt% MWCNT, 5 wt% NiO NPs
GO-CNT-NiO-525	5 wt% GO, 2 wt% MWCNT, 5 wt% NiO NPs
GO-CNT-NiO-515-A	5 wt% GO, 1 wt% MWCNT, 5 wt% NiO NPs, 2 M NH ₃
GO-CNT-NiO-525-A	5 wt% GO, 2 wt% MWCNT, 5 wt% NiO NPs, 2 M NH ₃
GO-CNT-NiO-515-U	5 wt% GO, 1 wt% MWCNT, 5 wt% NiO NPs, 2 M urea
GO-CNT-NiO-515-M	5 wt% GO, 1 wt% MWCNT, 5 wt% NiO NPs, 0.3 M melamine

3.3 Addition of MWCNT to the rGO-NiO composite

The morphology of the material, specifically the pores distribution, is a key factor for the energy storage performance since it is directly related to the active surface where the electrolyte can interact [170, 172–174]. Hence, a unique technique for producing high surface area nanocarbon electrodes involves physically separating two-dimensional graphene-like sheets with a tendency to aggregate using one-dimensional CNT [175–178]. This study will be performed with the addition of MWCNT to the rGO-NiO composite in different concentrations to obtain micrometric thickness films for better stability. With this thickness, the scalability problems to thicker electrodes will be essentially avoided, although the transition from rGO submicrometric thick films to tens or hundreds of micron thick electrodes could lead to appreciably lower volumetric capacitances. The capacitance of the rGO-CNT-NiO composites can be further improved by doping with nitrogen-containing chemical groups. The different electrodes were prepared from the target dispersions presented in the Table 3.4 by the accumulation of 6000 pulses at $0.4 J cm^{-2}$ laser fluence. The concentration of

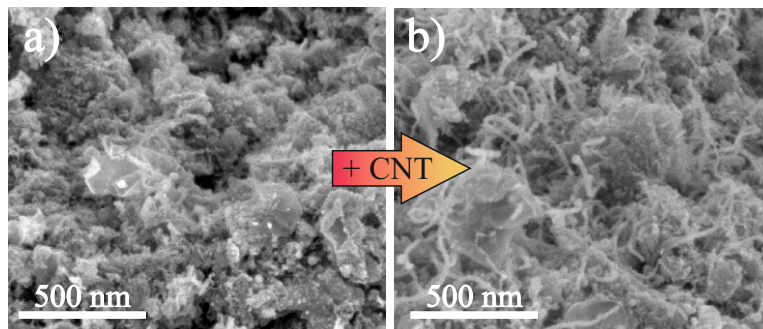


FIGURE 3.14: XHRSEM images of (a) GO-CNT-NiO-505, and (b) GO-CNT-NiO-515.

GO and NiO NPs was set at 5 wt% and the MWCNT concentration was varied up to 2 wt% to prevent precipitation and excessive viscosity of the dispersions. The different nitrogen-containing molecules used were ammonia, urea and melamine, which have been previously proven to cause laser-induced chemical reactivity and nitrogen doping [141]. The concentration of ammonia and urea were both set at 2 M, whereas the melamine concentration was fixed at 0.3 M to avoid precipitation.

3.3.1 Morphological characterization

The deposited films present a uniform black colour under visual inspection. The change in the morphology on the addition of MWCNT to the rGO-NiO composite is presented in Fig. 3.14. Randomly oriented MWCNT, of about 0.5–1 μm in length and *ca.* 20 nm in diameter, are mixed with rGO sheets, from hundreds of nm to *ca.* 1 μm in lateral size, and NiO NPs leading to an increased porosity. The rGO flakes display crumpled shapes and irregular edges, forming aggregates and cavities of about tens to hundreds of nm between the flakes and aggregates. Bent MWCNT appear in form of intertwined beams of nanotubes, randomly distributed over the rGO sheets.

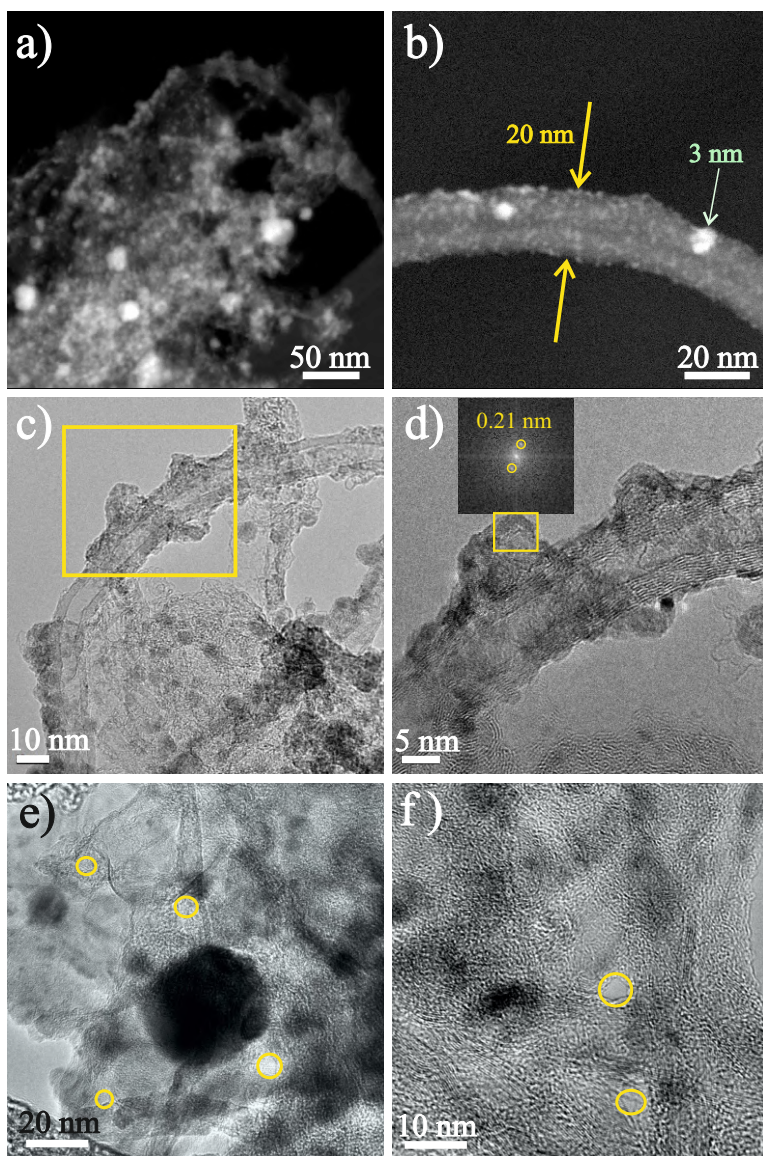


FIGURE 3.15: HAADF-STEM images of (a) GO flake and (b) MWCNT in sample GO-CNT-NiO-515. (c) HRTEM of sample GO-CNT-NiO-515; (d) zoomed-in area indicated in (c) with FFT of the area indicated by the rectangle. TEM images of (e) GO-CNT-NiO-515-M and (f) GO-CNT-NiO-515-A. Circles indicate the formation of nanometre-sized holes.

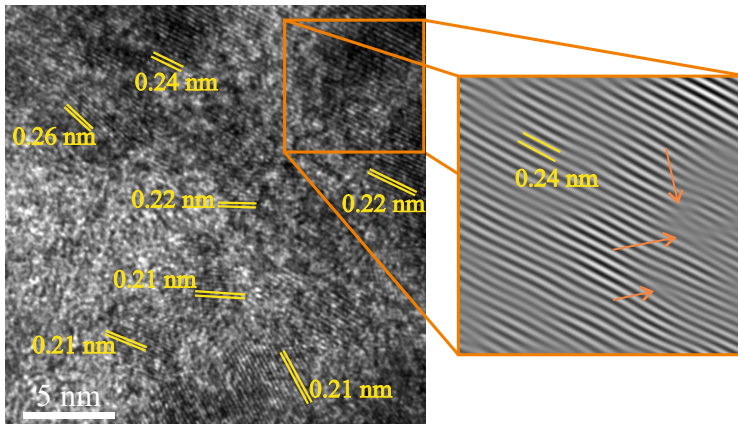


FIGURE 3.16: HRTEM image of GO-CNT-NiO-515-M and selected area filtered through FFT showing atomic planes of (111) NiO with arrows indicating dislocations.

High resolution HAADF-STEM studies reveal that the rGO and MW-CNT surfaces are covered with Ni containing nanostructures (bright regions in Fig. 3.15a) as small as 1 nm (Fig. 3.15b), indicating that the molten NiO NPs suffer both coalescence and dewetting mechanisms during the laser radiation action forming larger and smaller nanostructures than initial NPs. According to HRTEM analysis, the nanostructures covering both rGO flakes and MWCNT are crystalline (Fig. 3.15c and d). The interplanar distances of this nanometric regions, as determined by FFT studies, are 0.24, 0.21, 0.14, 0.12 and 0.1 nm, respectively attributed to (111), (200), (220), (222) and (400) crystallographic planes of cubic NiO (JCPDS 00-047-1049). Remarkably, small, up to 10 nm-sized holes can be identified on the surface of rGO flakes of the samples deposited in the presence of N-containing precursor (Fig. 3.15e and f) not observed in the undoped samples. Therefore, it could be stated that the nanoholes could be formed through laser-induced chemical reactions between the GO platelets and

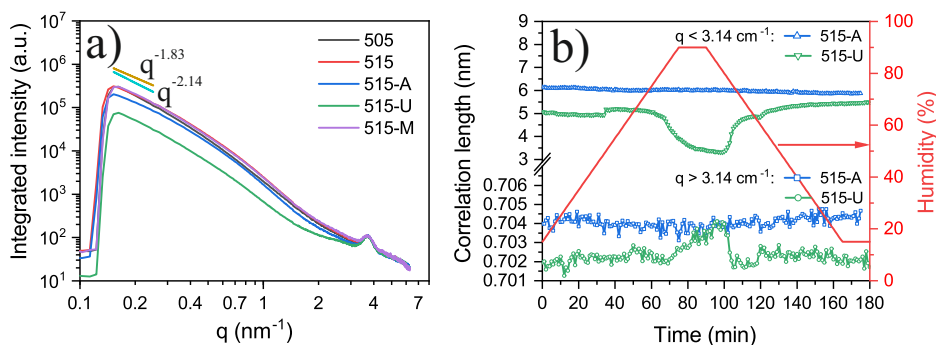


FIGURE 3.17: (a) In-plane GISAXS intensity profiles of all the samples. The q -range below 0.16 nm^{-1} is the beamstop area. The origin of the peak at $ca. 4 \text{ nm}^{-1}$ is from kapton window. (b) Temporal evolution of correlation length at low ($< 3.14 \text{ nm}^{-1}$) and high ($> 3.14 \text{ nm}^{-1}$) q -ranges.

N-containing molecules dissolved in the matrix submitted to laser radiation. HRTEM images of these N-containing films also depict highly crystalline NiO NPs with measured interplanar distances of $0.15\text{-}0.18 \text{ nm}$, $0.21\text{-}0.22 \text{ nm}$ and $0.24\text{-}0.25 \text{ nm}$ corresponding to (220), (200) and (111) crystallographic planes of cubic NiO (JCPDS 00-047-1049), respectively (Fig. 3.16). The value and distribution of these interplanar distances point to the development of highly strained structures, which would also explain the high density of edge dislocations found in certain areas filtered by FFT (Fig. 3.16 zoomed region). The intense kinetic conditions that crystals underwent during their growth at extremely high temperatures during very short times result in all of the phenomena described.

Grazing Incidence Small Angle X-ray Scattering (GISAXS) analysis was carried out to identify further structural characteristics at the nanoscale of the deposited composites. The acquired intensity profiles of representative samples are shown in Fig. 3.17a as a function of the in-plane scattering vector (q). The scattered intensities at the low q values recorded follow the power law and scale with the scattering vector as equation (2.2). The experimental data in the q -range below 0.24 nm^{-1} , corresponding to probing lengths ($d = 2\pi/q$) over 26 nm , was fitted with the aim to obtain the

power law exponents. The sample GO-CNT-NiO-505 is characterized by the highest exponent (2.14 ± 0.01). On the contrary, this value averaged for all samples containing MWCNT, decreases to 1.83 ± 0.02 . In the composite materials, the scattered intensity is a consequence of electron density fluctuations due to the presence of different types of nanomaterials exhibiting different sizes, shapes, structural changes and pores. Larger q -range measurements are necessary for the appropriate modelling of the structural responses. In addition, in order to investigate the fractal dimension of the samples, the q -range is requested to cover at least one decade, requiring Ultra-Small Angle X-ray scattering (USAXS) and Ultra-Small Angle Neutron Scattering (USANS) measurements. The present study will be focused on the qualitative description of water accessibility to the pores in the given q -range, specially for nitrogen-containing samples which exhibit the presence of nm -sized holes as shown by TEM (Fig. 3.15e and f). Additional GISAXS data was collected during continuous up-down humidity ramps, expected to cause the partial filling of pores with water. In such cases, the electron density variation should result in the form factor change and thus the scattering intensity. The q -range is split at 3.14 nm^{-1} , which correspond to probing length scales below 2 nm ($q > 3.14 \text{ nm}^{-1}$) and above 2 nm ($q < 3.14 \text{ nm}^{-1}$), and the correlation length (l_c) is calculated in the ranges using

$$l_c = \pi \frac{\int_0^\infty q I(q) dq}{\int_0^\infty q^2 I(q) dq} \quad (3.9)$$

where $I(q)$ is the scattering intensity [179, 180]. This parameter is shown in Fig. 3.17b as a very sensitive indicator of changes in the scattering data in the respective ranges assessed for samples GO-CNT-NiO-515-A and GO-CNT-NiO-515-U as a function of time. The fact that the GO-CNT-NiO-515-A samples exhibits no features while the sample produced with urea reversibly follows the humidity ramp in both q -ranges indicates that the surface chemistry is different for nitrogen-containing samples. All the rest of the samples measured behaves similarly to GO-CNT-NiO-515-A with no

response to humidity change. The correlation length of GO-CNT-NiO-515-U sample at low q -range decreases with the increase of humidity, indicating that the volume fraction of pores is greater than that of the composite material. In contrast, the correlation length rises with humidity at high q -range. These results point to the dominance of bigger ($> 2\text{ nm}$) pores in urea-containing sample, but more importantly, the reversible response in both q -ranges has been shown.

3.3.2 Compositional characterization

Wide-scan XPS surveys of the samples reveal the presence of C, O, N and Ni elements, similarly to the wide-scan spectra of GO-NiO-imi (Fig. 3.7a). The reduction and nitrogen incorporation processes in the rGO-MWCNT structures were studied through the C/O and $N/(N + C)$ atomic ratios assessed from the XPS surveys, after subtraction of the NiO contribution from O concentration (Fig. 3.18a and b). As observed, the C/O ratio slightly increases from 2.5 in samples GO-CNT-NiO-505 to 2.9 and 3.7 in GO-CNT-NiO-515 and GO-CNT-NiO-525, respectively, with the inclusion of MWCNT into the layer. This feature may indicate a lower relative oxygen-to-carbon content for MWCNT than for rGO. The C/O ratio increases using melamine, reaching 5.3. Then, it might be noted that the N-doping procedure results in increased reduction of the GO sheets and MWCNT. Furthermore, GO-CNT-NiO-515-M exhibits the highest level of nitrogen inclusion in the rGO structure (15.6), followed by the samples that were deposited in the presence of urea (10.9) and ammonia (6.5 for GO-CNT-NiO-515-A and 4.8 for GO-CNT-NiO-525-A). In the samples that include ammonia, the incorporation of higher concentration of MWCNT leads to the decrease of the the N-doping level, due to the higher carbon content present. The GO-CNT-NiO-505 and GO-CNT-NiO-515 samples exhibit the lowest nitrogen ratio, about 3.3 and 2.5, respectively, originating from the reactive interaction of the heated carbon nanoentities with the background N_2 gas.

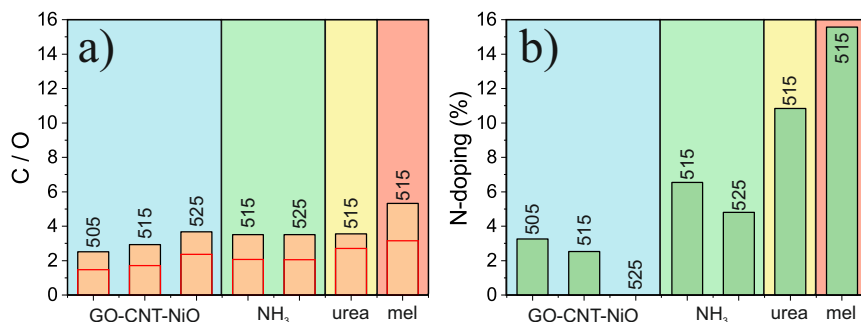


FIGURE 3.18: (a) Reduction degree and (b) nitrogen doping degree of fabricated electrodes. In (a), open bars are directly obtained from measurements, whereas filled bars correspond to the calculated concentration by subtraction of NiO contribution.

High resolution XPS spectra of C 1s and N 1s of the samples are similar to that of the samples which do not include MWCNT in their composition (Fig. 3.8b and c). The C 1s spectra of representative films were deconvoluted into five components: C = C sp^2 with some contribution of C – C sp^3 (284.7 eV), hydroxyl groups (285.6 eV), epoxide functionalization (286.7 eV), carboxylic groups (288.9 eV) and a shake-up satellite (290.4 eV) (Fig. 3.19a). These peaks are present in all samples, with the exception of the shake-up satellite which is characteristic for the GO-CNT-NiO-515-M film only (Fig. 3.19c). In all the spectra, the component associated to C = C bonds is the most intense one. The N 1s spectra were deconvoluted into four components assigned to pyridinic nitrogen (398.7 eV), pyrrolic-amine groups (399.9 eV), quaternary (graphitic) nitrogen (401.9 eV) and pyridinic NO_x (404.5 eV) (Fig. 3.19b) [157, 181, 182]. Interestingly, the concentration of different nitrogen groups vary from sample to sample (Fig. 3.19d). The pyrrolic-amine groups are present in all layers, being the unique component in GO-CNT-NiO-515 and GO-CNT-NiO-515-M, whereas GO-CNT-NiO-505 and GO-CNT-NiO-515-A contain also graphitic N. GO-CNT-NiO-515-A and GO-CNT-NiO-515-U contain pyridinic NO_x (14% of the deconvoluted area) and pyridinic N (37%) functionalization, respectively. The

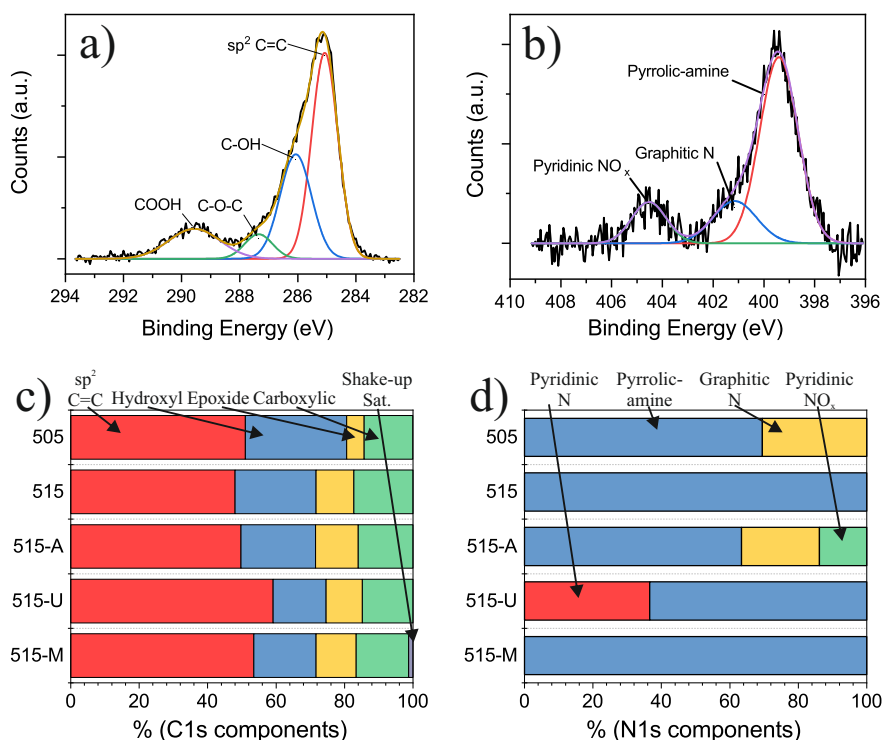


FIGURE 3.19: Deconvolution of high resolution (a) C 1s and (b) N 1s of GO-CNT-NiO-A sample. Areal percentage of the XPS deconvoluted components of the (c) C 1s and (d) N 1s peaks of the fabricated samples GO-CNT-NiO.

presence of the observed *nm*-sized holes in the N-containing rGO structures (Fig. 3.15e and f), can be explained by the fact that the pyridinic and pyrrolic N groups are linked to vacancies in the graphene backbone. The incorporation of nitrogen into the carbon structure could occur by two different methods [51, 183–187]:

- (i) The synthesis of a carbon-nitride material via thermal decomposition of the N-containing molecules, acting as an intermediate product for the formation of identified N-functional groups.

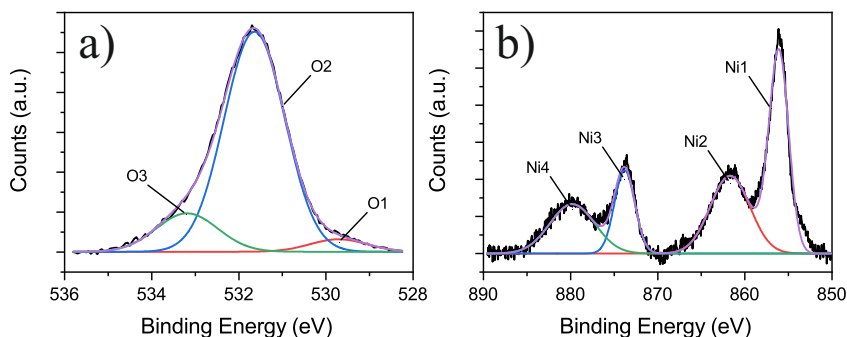


FIGURE 3.20: High resolution (a) O 1s and (b) Ni 2p spectra of the GO-CNT-NiO-515-U sample.

- (ii) The direct chemical reaction of GO-MWCNT functional groups with the N-containing precursor molecules and N_2 ambient gas in the irradiation chamber.

The O 1s and Ni 2p high resolution XPS signals were also registered. The representative O 1s and Ni 2p spectra are displayed in Fig. 3.20a and b, respectively. O 1s lines were deconvoluted into three components: O1 at 529.7 eV , O2 at 531.7 eV and O3 at 533.2 eV . O1 is associated to double C = O bonds of carboxyl groups present in the rGO and MWCNT, besides Ni – O bonds of the NiO nanostructures. O2 can be ascribed to defective sites and/or adsorbed O in NiO crystals, as well as nickel hydroxide compounds. O3 is related to single C – O bonds of the hydroxyl and epoxy groups of the nanocarbons [188]. All the samples show similar configuration of the O 1s components, being O2 the most intense peak. Finally, the spectra of the Ni 2p doublet were deconvoluted into four components: Ni1 (856.1 eV) and Ni3 (873.8 eV) corresponding to Ni 2p_{3/2} and Ni 2p_{1/2}, respectively, and their associated shake-up satellites Ni2 (861.7 eV) and Ni4 (879.8 eV). The GO-CNT-NiO-515-A sample also shows the presence of a weak component centred at 853.8 eV . The position of these distinctive peaks indicates the formation of NiO and Ni(OH)₂, which were formed by the chemical reaction between molten NiO droplets and evaporated H₂O molecules from the matrix [188].

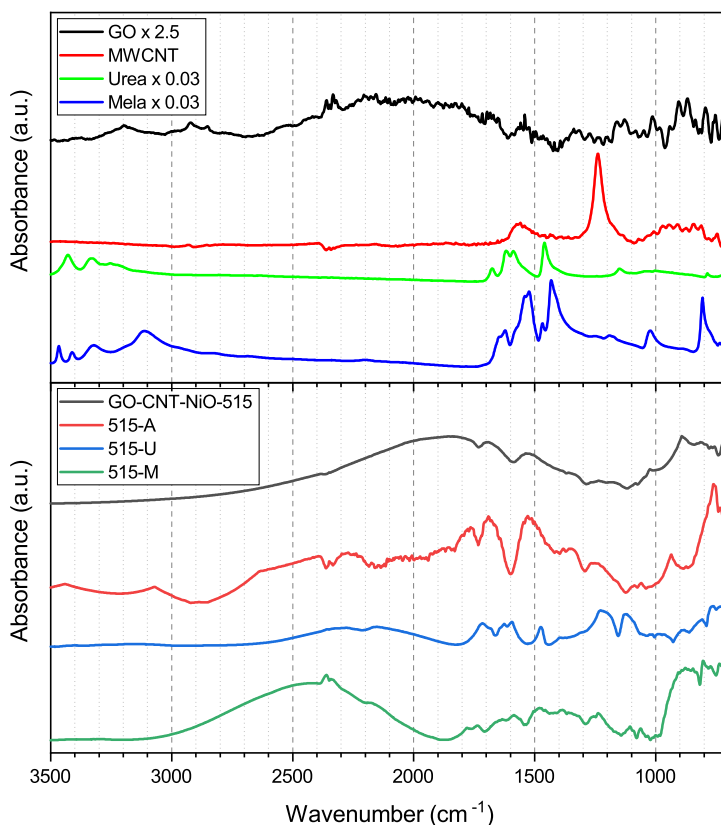


FIGURE 3.21: Characteristic FTIRM normalized spectra of raw GO, MWCNT, urea and melamine powders as well as deposited samples GO-CNT-NiO-515, GO-CNT-NiO-515-A, GO-CNT-NiO-515-U and GO-CNT-NiO-515-M.

Additional studies of the composition of the sample were performed by synchrotron trans-reflection mode-FTIRM. Representative spectra of raw precursors and films are shown in Fig. 3.21. The list of the observed bands and their assignment are presented in Table B.1 of the Appendix B. As seen, raw GO powder exhibits extremely weak characteristic bands, likely as a result of strong scattering. The spectrum of MWCNT displays the bands corresponding to C – O, C – OH and C – C bonds. The spectra of urea and melamine base materials are composed by typical bands of N- and O-containing groups. The spectrum of the GO-CNT-NiO-515 film mainly

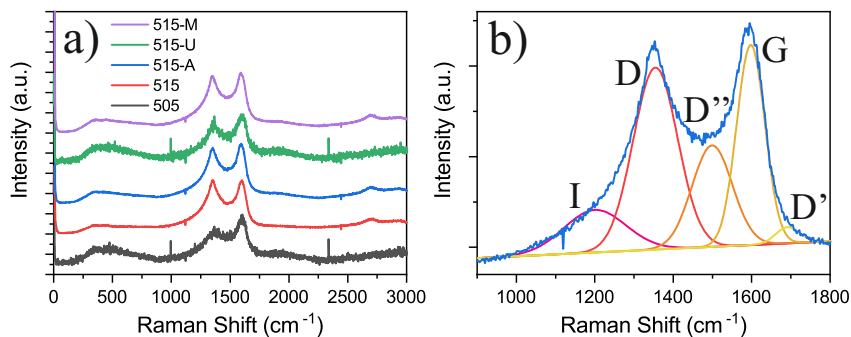


FIGURE 3.22: (a) Raman spectra acquired for representative films and (b) deconvolution of the Raman spectrum of film GO-CNT-NiO-515-A.

displays weak bands corresponding to C = C and C – O – C, besides the contribution of C = O and C – N bonds. The spectra of GO-CNT-NiO-515 films obtained with N-containing precursors reveal the presence of additional bands ascribed to several types of carbon-nitrogen chemical groups. The spectra of the deposited samples do not coincide with the spectra of the precursor materials. Thus, the presence of unreacted molecules may be disregarded. The considerable nitrogen incorporation and bonding types observed by XPS are confirmed by FTIR investigations. The absence of C – H or C – C sp³ bands may have contributed to the minor amorphization of the rGO/MWCNT and the formation of alkyl chains.

For the quantitative examination of the laser-induced structural modifications of the deposited carbon nanostructures, Raman spectroscopy investigations were also performed. Several spectra were acquired at different sites of each deposited layer (Fig. 3.22a) and were deconvoluted into five components centred at *ca.* 1190, 1360, 1490, 1600 and 1690 cm⁻¹ referred to as *I*, *D*, *D''*, *G*, and *D'* components, respectively (Fig. 3.22b). Moreover, the peak centred at 490 cm⁻¹ is associated to NiO nanostructures [189]. The sp²-bonded carbons contained in the materials generate the *G* band, whereas the presence of defects in the graphitic structure (vacancies, boundaries, sp³) cause the disorder-activated *D* band [190]. It is well acknowledged that the *D/G* intensity ratio (I_D/I_G) is a figure of merit

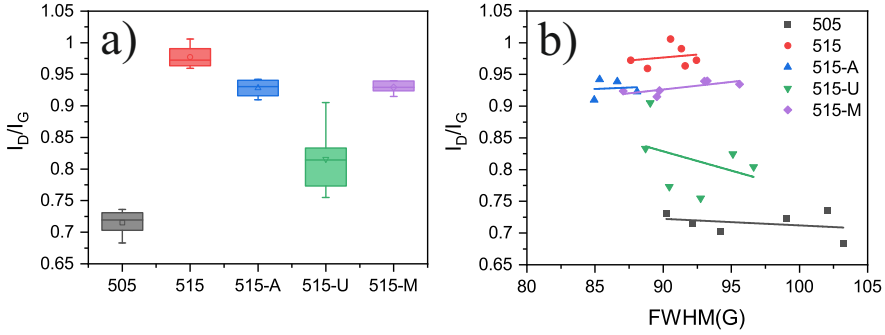


FIGURE 3.23: (a) Box plot of the measured D/G intensity ratios and (b) D/G intensity ratio *vs.* $FWHM(G)$ of representative samples, including linear fits.

for determining the quantity of defects present in the graphene structure, as well as the ratio of D/G integrated intensities. If the laser-generated defects destroy the graphitic rings, I_D/I_G increases in a low-density defects regime, whereas decreases in a high-density defects regime [190–192]. However, attaining only to the intensity ratio may lead to erroneous conclusions as the disorder not only affect the intensities of the bands but also the position and shape of the Raman peaks [193]. Since the width of the G band always increases with the structural disorder, the I_D/I_G *versus* full width at the half maximum of G, $FWHM(G)$, allows us to determine the defect regime of the rGO-MWCNT materials.

As observed in Fig. 3.23a where the D/G intensity ratios are presented, the samples GO-CNT-NiO-505 and GO-CNT-NiO-515-U are envisaged to have the lowest density of defects as they show the lowest D/G ratio. However, attaining to D/G intensity ratio *vs.* $FWHM(G)$ (Fig. 3.23b) reveals that these samples are in a regime of high density of defects, accounting to the decreasing behaviour. The samples GO-CNT-NiO-515, GO-CNT-NiO-515-A and GO-CNT-NiO-515-M exhibit the opposite tendency, indicating the presence of low density of structural defects.

According to the I_D/I_G *vs.* $FWHM(G)$ results, the mean distance between defects (L_D) and the corresponding density of defects (n_D) were calculated using

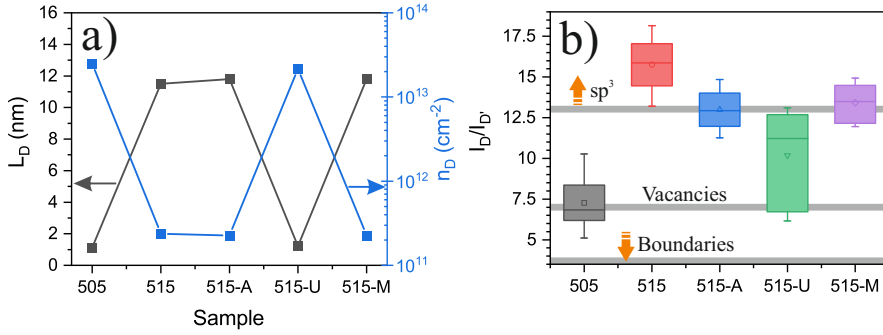


FIGURE 3.24: (a) Calculated mean distance between defects (L_D) and corresponding density of defects (n_D). (b) Box plot of the D/D' intensity ratio for the deposited samples.

$$L_D^2 (nm^2) = \frac{4.3 \times 10^3}{E_L^4 (eV^4)} \left[\frac{I_D}{I_G} \right]^{-1} \quad (3.10)$$

$$n_D^2 (cm^{-4}) = 7.3 \times 10^{-9} E_L^4 (eV^4) \frac{I_D}{I_G} \quad (3.11)$$

where $E_L = \hbar\omega_L$ is the laser photon energy in eV . Equations (3.10) and (3.11) are only valid for a regime of low-density of defects ($L_D > 10 nm$) [190, 191]. For a high-density of defects regime ($L_D < 3 nm$), it should be calculated using equations (3.12) and (3.13) [190]

$$L_D^2 (nm^2) = 5.4 \times 10^{-2} E_L^4 (eV^4) \frac{I_D}{I_G} \quad (3.12)$$

$$n_D^2 (cm^{-4}) = \frac{5.9 \times 10^{14}}{E_L^4 (eV^4)} \left[\frac{I_D}{I_G} \right]^{-1} \quad (3.13)$$

As observed in Fig. 3.24a, the samples GO-CNT-NiO-515, GO-CNT-NiO-515-A and GO-CNT-NiO-515-M disclose similar values of L_D (ca. 12 nm) and n_D (ca. $2 \times 10^{11} \text{ cm}^{-2}$), whereas GO-CNT-NiO-505 and GO-CNT-NiO-515-U reveal about one order of magnitude lower L_D (ca. 1 nm) and two order of magnitude higher n_D (ca. $2 \times 10^{13} \text{ cm}^{-2}$) values.

D and D' bands, absent in pristine graphene, increase when disorder is induced in the sample up to a maximum value where it begins to decrease. Therefore, these bands are activated by defects in graphene and the characteristics of such bands depend only on the type of defect and not on the defect concentration [194, 195]. The nature of the defects created in the deposited carbon nanostructures can be experimentally studied by the D/D' intensity ratio, $I_D/I_{D'}$ (Fig. 3.24b) [195]. The samples containing low-density of defects, GO-CNT-NiO-515, GO-CNT-NiO-515-A as well as GO-CNT-NiO-515-M, present a $I_D/I_{D'}$ ratio near 13, pointing to the main formation of defects associated with sp^3 hybridized carbon. Moreover, GO-CNT-NiO-505 and GO-CNT-NiO-515-U disclose $I_D/I_{D'}$ ratio of around 7.3 and 10.2, respectively, suggesting the foremost creation of vacancies with the possibility of some contribution of boundary-like defects. It is worth recalling that only the GO-CNT-NiO-515-U sample contains pyridinic C – N groups. The presence of these groups in conjunction with the high density of vacancies/boundaries could explain the SAXS different correlation length with humidity of this specific sample.

3.3.3 Electrochemical characterization

The registered CV plots display a quasi-rectangular shape with no presence of prominent peaks (Fig. 3.25a and b). The rectangular-like nature of the voltammograms, together with the main contribution of capacitive processes calculated using equation (2.4) and shown in Fig. 3.25c and d, points towards capacitive charge storage processes. The addition of MWCNT does not increase significantly the diffusion components. Therefore, the volumetric capacitance of the electrodes can be calculated using equation (2.3). As witnessed in Fig. 3.25e, the maximum capacitance of the electrodes without MWCNT is *ca.* $4 F cm^{-3} @ 10 mV s^{-1}$. Interestingly, the addition of MWCNT to the material structure significantly increases the volumetric capacitance. The maximum values of capacitance rise to *ca.* 10 and $20 F cm^{-3} @ 10 mV s^{-1}$ in electrodes GO-CNT-NiO-515 and GO-CNT-NiO-525, respectively. This implies that the addition of 2 wt% MWCNT to the GO-CNT-NiO-505 target will enhance capacitance by 500%. The large

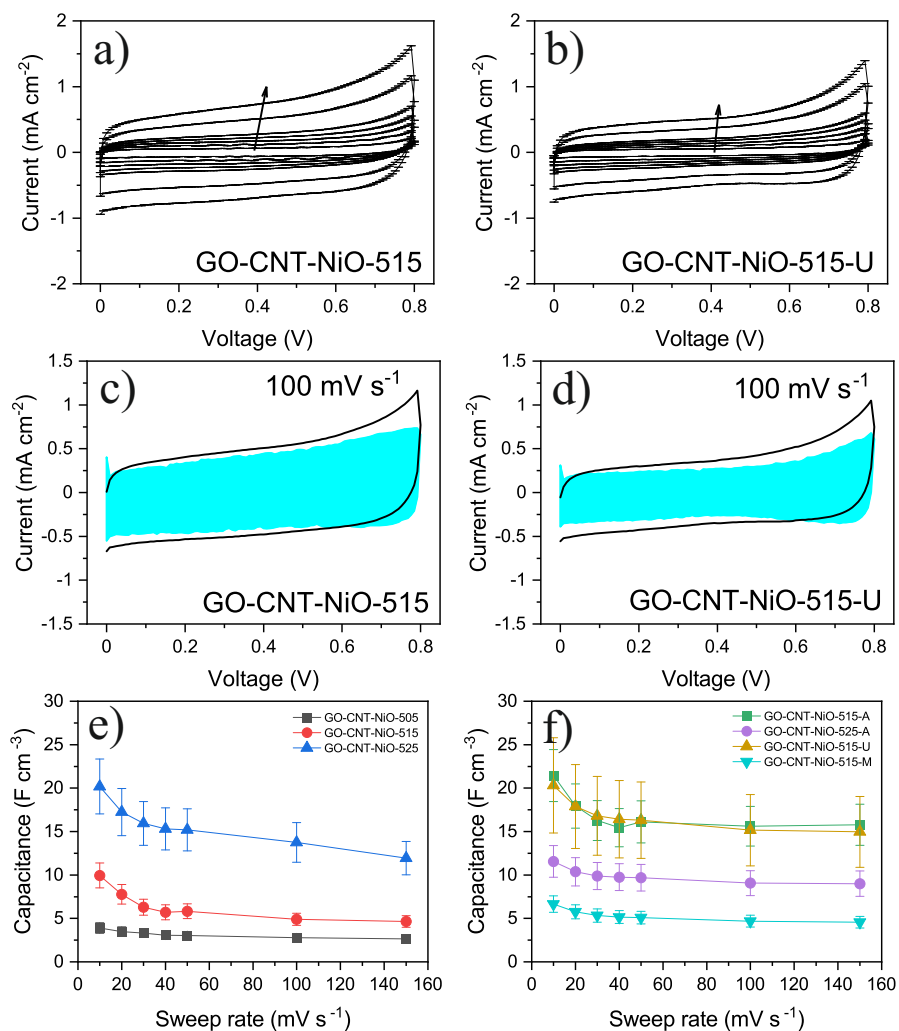


FIGURE 3.25: CV curves at sweep rate range 10–150 $mV s^{-1}$ of (a) GO-CNT-NiO-515 and (b) GO-CNT-NiO-515-U (arrow indicates the increasing sweep rate). CV of (c) GO-CNT-NiO-515 and (d) GO-CNT-NiO-515-U electrodes at 100 $mV s^{-1}$ with surface capacitance contribution highlighted in blue. Volumetric capacitance *vs.* sweep rate of (e) GO-CNT-NiO electrodes and (f) N-doped electrodes.

increase of capacitance can be attributed to the film's increased porosity since the nanostructure and composition of the samples do not appreciably differ from one another. The low mass loading of the films does not allow for the quantitative evaluation of the porosity through the conventional Brunauer-Emmett-Teller (BET) method. SEM analyses, however, distinctly show the existence of NiO-coated MWCNT that are randomly oriented inside the films. These MWCNT create channels between rGO sheets enhancing the electrolyte's ionic access to larger surface area of the material (Fig. 3.14) [172, 173, 196].

Additionally, the chemical composition plays a critical influence in the capacitance of the films (Fig. 3.25f). The volumetric capacitance of GO-CNT-NiO-515 samples deposited in the presence of ammonia and urea precursors increases to $20\text{--}21\text{ F cm}^{-3}$ @ 10 mV s^{-1} despite their different N-doping nature in their structure. However, the electrode with the highest N-doping percentage (mainly pyrrolic N-amine) deposited in the presence of melamine precursor has a lower capacitance than the GO-CNT-NiO-515 electrode. The rGO-NiO and rGO-NiO-melamine electrodes previously showed a similar behaviour, which was linked to the decreasing porosity of the composite material [141]. The combined action of O- and N-containing groups, such as quinone- and pyridinic-pyrrolic N, have also been proven to increase electrochemical energy storage capacitance [162]. Moreover, graphitic-N groups, absent in the melamine sample, have been demonstrated to contribute as strong electron-acceptor improving electron transport [197–199]. These characteristics would also induce the raise of the capacitance of the electrodes obtained with ammonia and urea. Surprisingly, when the relative amount of MWCNT in the ammonia-based targets increases (GO-CNT-NiO-525-A), the capacitance decreases as compared to the samples synthesized in the absence of ammonia. Different explanations could be given to this behaviour [51, 186]:

- (i) Variations in film morphology (porosity) caused by the different thermal conditions developed at the MAPLE targets during laser irradiation.

- (ii) Variability in redox behaviour or charge-transfer efficiency of similar N-containing groups depending on their base material, either rGO or MWCNT.
- (iii) Minor differences in the structure of N-containing groups in rGO and MWCNT not detected by XPS and FTIRM measurements, caused by reaction of ammonia during laser irradiation with O-containing groups in GO and carboxylic-doped MWCNT.

Galvanostatic charge-discharge analyses of GO-CNT-NiO samples were performed in the $0.03\text{--}6\text{ mA cm}^{-2}$ current density range. The resulting curves exhibit a nearly linear voltage response with time, with a triangular shape, characteristic for capacitive materials (Fig. 3.26a). As expected, the charge/discharge time decreases as the current density rises. Equation (2.5) was also used to compute the volumetric capacitance of the electrodes. The capacitance rapidly decreases with the increase of the applied current density, as shown in Fig. 3.26b. At a current density of $30\text{ }\mu\text{A cm}^{-2}$, the maximum capacitance of 84 F cm^{-3} is measured in the GO-CNT-NiO-515-A electrode.

EIS measurements of the electrodes are presented in Fig. 3.27a. The Nyquist plots of the samples display the characteristic straight-line shape at low frequencies and a partial semicircle at high frequencies previously explained. The equivalent circuit represented in Fig. 3.27b was used for the fitting of the electrodes. The circuit is based on a Randles cell and consist on an equivalent series resistance ($R1$); a constant phase element ($CPE1$); a resistor ($R2$) in parallel with the CPE accounting for leakage of charges in the capacitor due to electrochemical reactions; and a Warburg element (W) in series with the capacitor, related to semi-infinite diffusion of ions in the electrode. In contrast with the equivalent circuit used for imidazole containing electrodes (Fig. 3.12b), there is no second CPE element to differentiate EDL and pseudocapacitance. Similar characteristic times could impede their distinction in two components. Therefore, the only CPE used should incorporate both mechanisms. Table 3.5 presents the fitted values

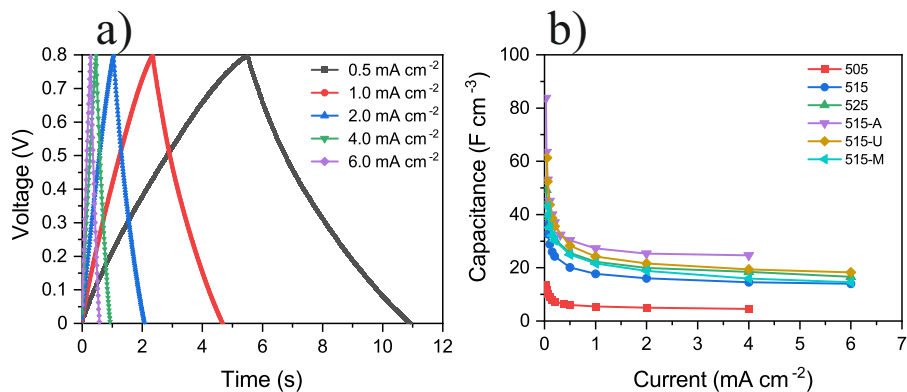


FIGURE 3.26: (a) Galvanostatic charge-discharge data of electrode GO-CNT-NiO-515-U and (b) volumetric capacitance *vs.* applied current density of GO-CNT-NiO samples.

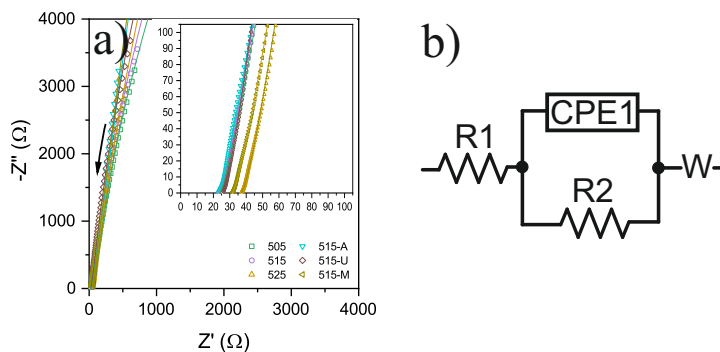


FIGURE 3.27: (a) Nyquist plot of the EIS measurement (points) and simulated data from equivalent circuit (lines) of GO-CNT-NiO samples (the arrow indicates the direction of increasing frequency). Inset details the high frequency range. (b) Equivalent circuit for data fitting.

TABLE 3.5: Fitting values for the elements of the equivalent circuit for GO-CNT-NiO electrodes.

	R1 (Ω)	R2 ($k\Omega$)	CPE1		W
			Y ($\mu S s^n$)	n	A_W ($\Omega s^{-1/2}$)
GO-CNT-NiO-505	23.8	50	54.5	0.93	186.4
GO-CNT-NiO-515	22.7	54	49.6	0.94	218.7
GO-CNT-NiO-525	31.5	97	60.6	0.93	174.1
GO-CNT-NiO-515-A	22.7	$> 10^5$	57.5	0.92	141.6
GO-CNT-NiO-515-U	25.2	63	46.8	0.95	187.9
GO-CNT-NiO-515-M	36.8	260	57.7	0.94	189.4

of the parameters of the equivalent circuit components. The equivalent series resistance, R_1 , of the electrode-electrolyte system ranges from 23–37 Ω . The n exponent of the CPE element is greater than 0.92, indicating a nearly ideal capacitor performance. The leakage resistance, R_2 , is high in all electrodes ($> 50 k\Omega$) accounting for low loss of stored charges, in agreement with the similar charge/discharge time relation, equal to 1. Interestingly, this resistance rises with the loading of MWCNT, and the GO-CNT-NiO-515-A electrode shows practically no leakages.

Additional studies of representative samples were investigated through Step Potential Electrochemical Spectroscopy (SPECS), scanning the applied voltage in steps of 25 mV in the 0–0.8 V range (Fig. 3.28a). All the current peaks were fitted using equation (2.13) and an example of this fitting is shown in Fig. 3.28b. Fig. 3.29 presents the fitted values C_C , R_S , B and G (or i_{res}) obtained as a function of the voltage step. The GO-CNT-NiO-515-U electrode has the highest capacitance across the entire voltage range, followed closely by GO-CNT-NiO-515-A but with statistically different results, verified by an ANOVA study of the capacitance calculated from multiple SPECS and CV experiments. This can be concluded despite

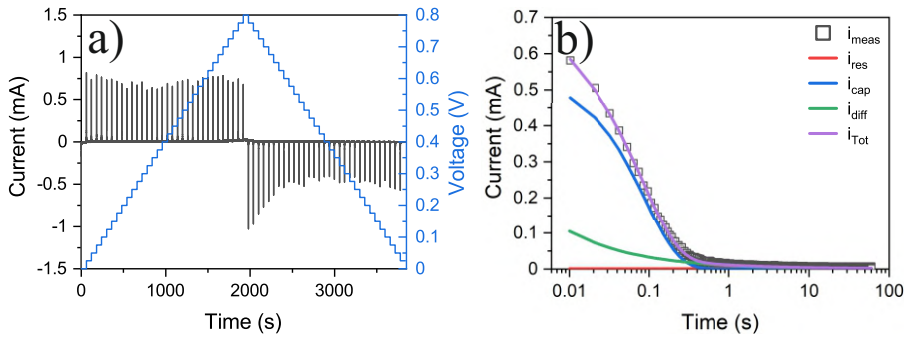


FIGURE 3.28: (a) Example of applied voltage steps and corresponding current evolution with acquisition time in SPECS experiment. (b) Fitting of a typical measured current curve (i_{meas}) considering the capacitive (i_{cap}), diffusional (i_{diff}) and residual (i_{res}) components, and $i_{Tot} = i_{cap} + i_{diff} + i_{res}$.

the dispersion and associated error of the fitted values. The electrodes GO-CNT-NiO-515 and GO-CNT-NiO-515-M show lower and fairly similar capacitance between them, while GO-CNT-NiO-505 exhibits the lowest capacitance, demonstrating that the addition of MWCNT increases the ability of the rGO-based composite to store energy. Interestingly, as compared to the other electrodes, GO-CNT-NiO-515-U exhibits a significantly greater value of R_S . Since the electrolyte, cell configuration and current collector are constant across all experiments, the change in series resistance should be attributed to the chemical-structural modification of the active material of the electrodes. Some interaction deviations at the electrode-electrolyte interface brought on by surface redox reactions could also increase this resistance. In all voltage range, the B parameters of the GO-CNT-NiO-515-U and GO-CNT-NiO-515-A electrodes are very similar and higher than those of other samples. This fact would imply higher values of either the effective area or the diffusion coefficient of such electrodes, given an equivalent amount of transferred electrons in their respective redox processes and comparable ionic concentrations. In all electrodes, the residual current, i_{res} ,

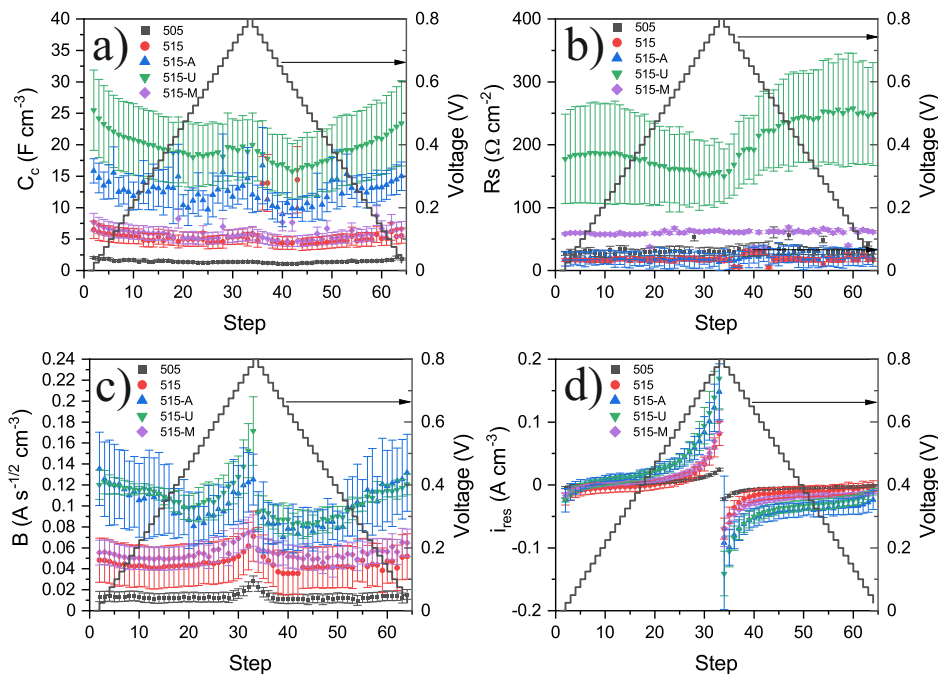


FIGURE 3.29: Results obtained from fitting SPECS current curves for each measurement step: (a) C_C , (b) R_S , (c) B and (d) i_{res} parameters.

increases with the applied voltage, being slightly higher for GO-CNT-NiO-515-U and GO-CNT-NiO-515-A electrodes.

Cyclic voltammograms can be emulated from the SPECS data in the 4×10^{-4} – 1.2 V s^{-1} sweep rate range [132]. As seen in Fig. 3.30a, the resulting voltammograms display a rectangular-like shape, as demonstrated in previous CV studies, indicating that the surface processes (EDL and pseudocapacitance) contribute mainly to the stored charge. The measured current was assumed to be the sum of the capacitive (i_{cap}) and diffusional (i_{diff}) components, with the contribution of residual current (i_{res}) being disregarded. The response current should follow equation (2.4), which enables analysis of the contribution to the current of the capacitive (surface) processes and the diffusion-limited ones for each voltage (Fig. 3.30a). As expected, the percentage of the capacitive contribution increases with

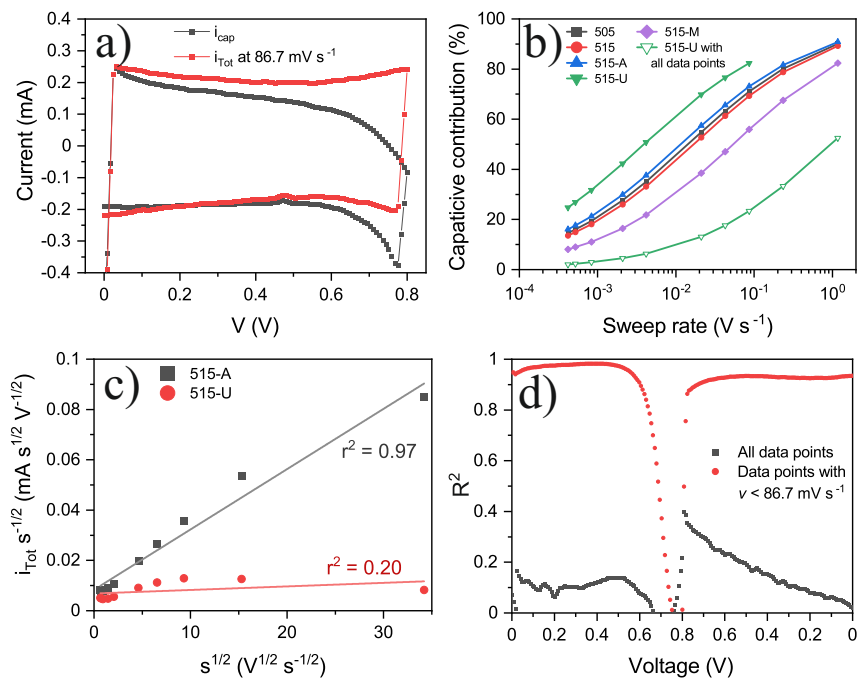


FIGURE 3.30: (a) Typical voltammogram generated from SPECS data, corresponding to GO-CNT-NiO-5151-U electrode at 86.7 mV s^{-1} sweep rate (i_{Tot}), together with the calculated current generated from the capacitive processes (i_{cap}). (b) Percentage of the capacitive charge for the analysed electrodes. (c) Typical linear fitting of $i_{Tot} v^{-1/2}$ vs. $v^{-1/2}$ for GO-CNT-NiO-5151-U and GO-CNT-NiO-5151-A electrodes. (d) Coefficient of determination (R^2) of the linear fitting as a function of voltage (up and down) for the GO-CNT-NiO-5151-U electrode.

sweep rate due to the difficulties of diffusional ionic species to follow the fast voltage variations (Fig. 3.30b). In contrast to the above conclusions, the GO-CNT-NiO-515-U electrode displays a significantly low capacitive contribution that could be interpreted as “battery-like” behaviour. However, the origin of this effect is connected to the fitting process. Fig. 3.30c shows two typical linear regressions of $i_{Tot} v^{-1/2}$ vs. $v^{-1/2}$. As can be seen, the data from GO-CNT-NiO-515-A film fits the data well across all the voltage range, while GO-CNT-NiO-515-U sample has a very poor fit due to the current fading at highest sweep rates. In the complete voltage range of this

particular sample, a extremely low coefficient of determination is calculated (Fig. 3.30d), not observed for other electrodes. This lack of linearity may be the result of the electrical attenuation in the porous matrix of the electrode, which exhibits an additional increase in resistance that is not taken into account by equation (2.4). This behaviour was attributed to the “porous-electrode” effect [200, 201] where the signal may become attenuated in pores having finite resistance, leading to a progressively increase of the iR -drop. Due to this attenuation, the local response current cannot be stated as a straightforward relation between the current and v or $v^{1/2}$. Thus, it is possible to underestimate the surface percentage. Therefore, the significantly larger R_s values found in GO-CNT-NiO-515-U compared to the other electrodes are likewise explained by this “porous-electrode” effect. The linear regression of this particular sample disregarding the fastest sweep rates ($v > 86.7 \text{ mV s}^{-1}$) results in a coefficient of determination close to 1. This value is maintained across the entire voltage range with the exception of voltages close to 0.8 V. Consequently, the associated capacitive percentage significantly increases, rising to the highest one (Fig. 3.30b). The larger C_C values obtained from the current peaks regression investigation (Fig. 3.29a) and this outcome would be consistent.

The reactive inverse MAPLE fabrication of ternary hybrid electrodes composed of rGO, MWCNT and NiO NPs was proven. The relative quantity of MWCNT allows the tuning of the layer morphology leading to a boost of the capacitance. The majority of previous works primarily attribute the increased capacitance seen in the N-doped graphene-based electrodes to various elements of the electric-faradaic behaviour of the N-containing functional groups and their impact in nearby carbon atoms [185, 202–208]. Thus, it is believed that the graphitic N promotes the electron transfer, leading to the decrease of the charge-transfer resistance of the n-type doped graphene. In addition to their activity in catalytic reactions, pyridinic and pyrrolic N are also believed to have pseudocapacitive properties in charge-discharge processes, especially in pyridinic groups. Large dipole moments are also present in substitutional and pyridinic N, which would increase the wettability of the electrode. Despite the fact that the

porosity is always present, significantly fewer studies connected the improvement in charge storage performance to the nanomorphology caused by nitrogen doping of graphene [209–211]. The results of the present study reveal the significance of the structural configuration of the electrode at the nanoscale — specially, crystalline defects — influencing the ability of the electrode to store energy. This structural effect, which is related to chemical functionalization, might be as significant as the faradaic component. Obtaining electrodes with a certain structural-electrochemical nature highly depends on the type of precursor molecule used for the N-doping process. The GO-CNT-NiO-515-U electrode exhibits a considerably more porous structure as compared to other electrodes, as revealed by the XPS, Raman spectroscopy and GISAXS investigations. This is due to the presence of pyridinic N in the electrode, which is linked to carbon atom vacancies and the formation of nanoholes [212]. This feature together with the faradaic nature of pyridinic N [213], would explain the higher capacitance of the electrode as compared to highly N-doped films with comparable density of defects in the graphitic structure. Due to the electric-faradaic behaviour of the graphitic N and pyridinic N – O groups [162], the capacitance of GO-CNT-NiO-515-A sample is almost double of that of GO-CNT-NiO-515-M and its counterpart without ammonia (GO-CNT-NiO-515). Additionally, it has been demonstrated that the pyrrolic N groups, despite being linked to structural holes, do not significantly contribute to the capacitance of the samples. Pyridinic N would preferentially form in the basal-plane, whereas pyrrolic N is situated at the edges of plasma-fabricated N-doped graphene materials [214]. Assuming this fact, edge pyrrolic N in the fabricated composites would not significantly contribute to the formation of nanoholes (i.e. to the increase of the effective surface area), on the contrary to basal pyridinic N groups, which mostly contribute to the increase of the EDL capacitance.

3.4 Conclusions

Reactive inverse MAPLE is a potential technique for the fabrication of functional graphene-based composites for electrochemical capacitors.

Electrodes composed of rGO only were successfully developed. The effects of the addition of NiO NPs to the rGO was also studied. The formation of NiO nanostructures were demonstrated, enhancing the areal capacitance of the rGO-NiO composite. The storage performances of the electrodes were improved with the addition of imidazole to the RIMAPLE target dispersion as nitrogen-containing precursor to N-doped the nanocarbon material. The assembling of symmetric electrochemical devices was tested, with good durability and stability upon cycling, up to 10000 cycles.

The addition of MWCNT increased mesoporosity, which augments diffusion pathways for the ionic species of the electrolyte, leading to the increase of the capacitance. Additionally, the constitution of the carbon nanoentities significantly differs depending on the type of N-containing precursor molecule. It was possible to deposit nanocomposites with controlled degrees of GO reduction and N-doping level, through UV laser-induced reactions between GO sheets and precursor molecules, enabling the adjustment of the functional characteristics in a very straightforward and flexible manner. Notably, compared to analogue electrodes containing rGO, MWCNT, NiO with different N-doping, the electrode synthesized using urea precursor in the target exhibited higher porosity and density of structural defects of the vacancy-boundary type. The significant increase in the capacitance of the electrode was directly associated to the variation in structural configuration at the nanoscale, related to the presence of pyridinic N.

Chapter 4

Nanocarbon-based electrodes with CeO₂

This chapter will be focused on the development of carbon-based electrodes decorated with CeO_x NPs. Simulations of the laser process will elucidate the different mechanisms involved during deposition. Morphological and compositional analyses will describe the electrodes and their energy storage performance will be studied by means of electrochemical measurements.

After this investigation, the composite electrodes' electrochemical performances will be improved through the addition of manganese oxide NPs. Two different methods of target preparation will be tested and the results will be compared between them and previous ones. Subsequently, a device will be assembled and studied with the best obtained electrodes. To conclude, the electrochemical performance of these electrodes will be evaluated with an organic electrolyte.

4.1 Electrodes composed of rGO, MWCNT and CeO_x

Cerium dioxide (CeO₂) is a relevant rare earth metal oxide that is both abundant and inexpensive. Recent findings demonstrate the exceptional supercapacitive performance of CeO₂ nanostructures [215–217], and also in combination with carbon-based materials [218, 219]. Despite having

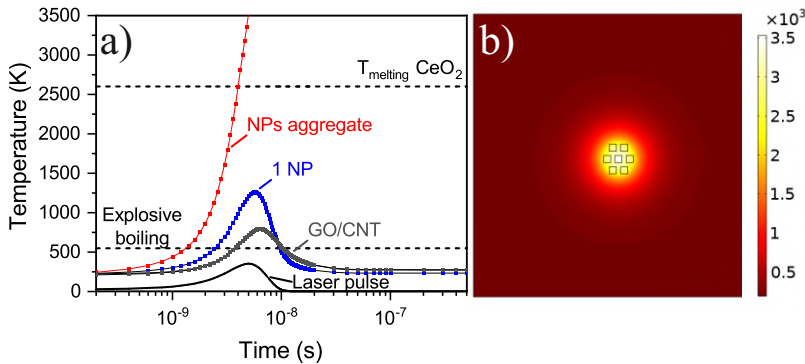


FIGURE 4.1: (a) Simulated temperature of CeO_2 NPs and carbon nanostructures during laser irradiation and (b) temperature map (K) of an aggregate of 50 nm radius composed of 6 NPs surrounding a single one at the end of the laser pulse.

good redox characteristics, CeO_2 structures generally have poor conductivity and lack of structural stability. Synergistic effects would arise from the combination of this material in nanoscale size with carbon-based compounds. This way, the disadvantages of CeO_2 materials could be avoided preserving the thermal conductivity, high electron mobility, mechanical stability and large surface area of carbon-based materials.

As previously stated in Chapter 3, GO and MWCNT follow similar photothermal and photochemical processes. Focusing on CeO_2 NPs and considering their absorption and their bandgap of *ca.* 3.2 eV [220], the excited electrons would result in significant heating through electron-phonon scattering. The laser irradiation of CeO_2 could cause its reduction forming Ce_2O_3 [221, 222]. Moreover, a reversible transition between the cerium oxidation states Ce^{4+} and Ce^{3+} can be produced by the existence of intrinsic oxygen vacancies from either laser-induced defects or the raw nanoparticle lattice [223].

The effect of UV laser irradiation of GO, MWCNT and CeO_2 NPs immersed in a water-ice target during RIMAPLE deposition process was investigated by numerical simulations using COMSOL software. The study

TABLE 4.1: Relative concentration of precursors in the aqueous dispersions for RIMAPLE targets composed of GO, MWCNT and CeO₂ NPs.

Target dispersion	Composition
GO-Ce	5 wt% GO, 5 wt% CeO ₂ NPs
CNT-Ce	1 wt% MWCNT, 5 wt% CeO ₂ NPs
GO-CNT-Ce-515	5 wt% GO, 1 wt% MWCNT, 5 wt% CeO ₂ NPs
GO-CNT-Ce-525	5 wt% GO, 2 wt% MWCNT, 5 wt% CeO ₂ NPs

of nanocarbon materials follows a similar description as using NiO NPs described in Chapter 3. The temperature change was simulated during single pulse irradiation conditions taking into consideration the optical [224] and thermophysical properties [225] of CeO₂ NPs (Table A.1). As previously stated, the transparency of water ice to the used UV radiation allows the rapid heating of the nanocarbon materials and the oxide NPs after the absorption of the radiation. As shown in Fig. 4.1a, the abrupt heat released by a single NP or a carbon nanoentity (GO, CNT) induces the explosive boiling of water ice surrounding the laser-absorbed material and the deposition of the material of interest in the substrate surface. GO is reduced throughout this deposition process by the laser irradiation, and the CeO₂ NPs follow thermally-driven recrystallization at temperatures above 1000 °C during several *ns*, but remaining below the melting point. However, since NPs tend to aggregate, melting and phase change of the CeO₂ can be induced by laser irradiation of the aggregates with dimensions at least 50 *nm* radius (Fig. 4.1b).

Electrode layers were prepared starting from dispersions with concentrations of base materials summarized in the Table 4.1. The deposition of the electrodes was performed by the accumulation of 6000 pulses at 0.4 J cm^{-2} laser fluence. Stainless steel foils were used as substrates, following the procedure described in Chapter 2.

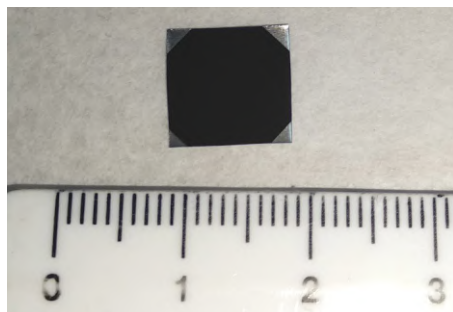


FIGURE 4.2: Electrode layer deposited over stainless steel substrate.

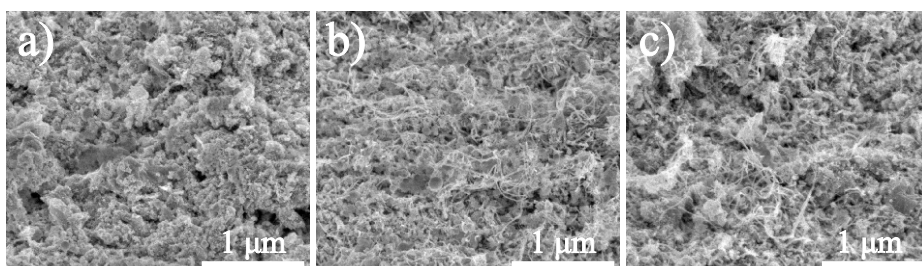


FIGURE 4.3: XHRSEM images of (a) GO-Ce, (b) CNT-Ce and (c) GO-CNT-Ce-515 samples.

4.1.1 Morphological characterization

The fabricated electrodes are adherent to the flexible substrate and show uniform black colour (Fig. 4.2). The thickness of the electrodes is on the micrometric range: $1.4 \pm 0.2 \mu\text{m}$ for GO-Ce; $1.2 \pm 0.1 \mu\text{m}$ for CNT-Ce; $1.7 \pm 0.1 \mu\text{m}$ for GO-CNT-Ce-515; and $1.1 \pm 0.1 \mu\text{m}$ for GO-CNT-Ce-525. Morphological XHRSEM analyses prove that the fabricated electrodes have a homogeneous structure. The carbon nanostructures of GO-Ce (Fig. 4.3a) and CNT-Ce (Fig. 4.3b) composites can be clearly distinguished. The structure of the ternary rGO, MWCNT and CeO_2 NPs layer (Fig. 4.3c) is characterized by a higher porosity as compared to the binary counterparts.

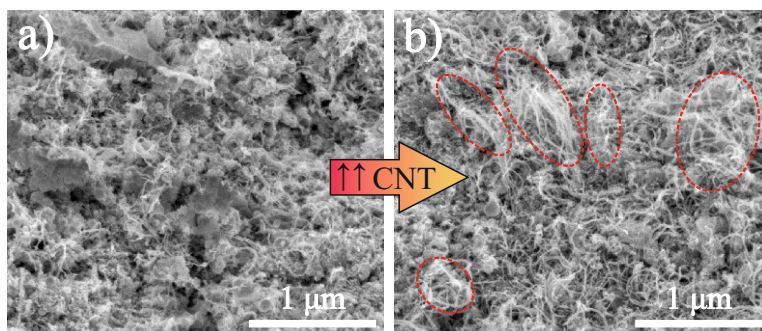


FIGURE 4.4: XHRSEM images of (a) GO-CNT-Ce-515, and (b) GO-CNT-Ce-525. Regions with agglomerated MWCNT are indicated.

The investigations revealed that the concentration of MWCNT in the initial dispersion is crucial to avoid aggregation. The increase of the MWCNT concentration to 2 wt% causes the formation of aggregates and intertwined nanotubes (Fig. 4.4b), not observed at lower concentration where the MWCNT are evenly distributed (Fig. 4.4a).

Fig. 4.5a and b show higher magnification XHRSEM images where the presence of rGO sheets and MWCNT decorated with nanostructures can be observed. In Fig. 4.5c, the HRTEM image reveals that the MWCNT (0.34 nm interplanar distance) are covered with nanocrystals. The surface particles have dimensions of around 5 nm and show highly crystalline structures with interplanar distance of 0.31 nm corresponding to the (1 1 1) lattice plane of CeO₂ (JCPDS 00-004-0593). These structures are spread over the surface of the MWCNT. It is worth mentioning that these structures are suitable for energy storage applications with the MWCNT working both as a scaffold and as a current collector for the insulating pseudocapacitive metal oxides, which store energy through pseudocapacitance. Additionally, the small size of the oxide crystals enables them to maintain low electric resistance [223]. Besides the few nanometer-sized nanoparticles, larger spherical particles can also be distinguished, with diameters reaching a few tens of nanometers (Fig. 4.5a). The particles size range is different from that of raw CeO₂ NPs (average diameter of 25 nm) due

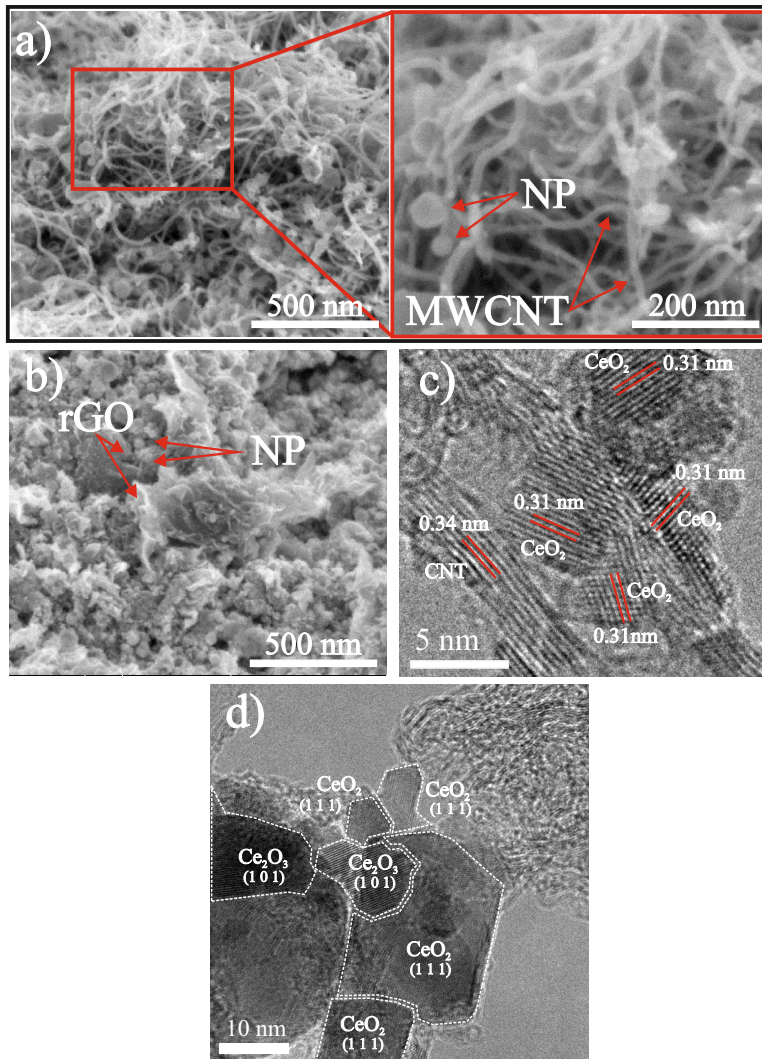


FIGURE 4.5: XHRSEM images of (a) CNT-Ce electrode with magnified region on the right and (b) GO-Ce layer. HRTEM images of (c) CNT-Ce and (d) GO-CNT-Ce-515.

to the laser-induced structural transformation during the deposition process. Small nanoparticles would be probably formed by fragmentation of molten CeO₂ droplets while the larger particles, through their coalescence. HRTEM images of GO-CNT-Ce-515 sample indicate that both rGO sheets and MWCNT were decorated with NPs exhibiting a plethora of sizes and compositions (mainly CeO₂ and Ce₂O₃). Fig. 4.5d reveals different crystalline domains compatible with (1 0 1) and (1 1 1) lattice planes of Ce₂O₃ (JCPDS 00-023-1048) and CeO₂, respectively, of sizes in the range 5 – 35 nm, proving that part of the CeO₂ is reduced during the laser deposition process.

4.1.2 Compositional characterization

Fig. 4.6a shows the wide range XPS spectrum of the GO-CNT-Ce-515 electrode. The spectrum consists on the lines corresponding to the elements present in the composition of the layer, C, O and Ce. The incorporation of N from background gas during deposition is negligible as the N 1s line could not be detected in the spectrum. In Fig. 4.6b and c, the respective C 1s and O 1s high-resolution spectra of the electrode are presented. C 1s peak is deconvoluted into four lines equivalent to rGO-NiO composites from Chapter 3, corresponding to sp²-bonded carbon (284.8 eV) with some contribution from sp³ bonds, carbon-oxygen single bonds hydroxyl (285.7 eV) and epoxide (286.5 eV) as well as carbon-oxygen double bonds of carboxylic (289.5 eV) groups [141]. As in rGO-NiO samples, the absence of carbonyl groups present in RIMAPLE samples that contain Fe₃O₄ and TiO₂ NPs [108, 141, 145], is noteworthy. Analysing the areal percentage of each peak, sp²-bonded C=C is the main component of the C 1s spectrum, indicating the reduction of the GO platelets during laser irradiation and the formation of graphene-like structures. Furthermore, O 1s signal is deconvoluted in components corresponding to oxygen bonding with Ce⁴⁺ (529.95 eV) and Ce³⁺ (531.4 eV), the last one also related to oxygen vacancies O²⁻ in the metal oxide lattice, besides the contributions of hydroxyl

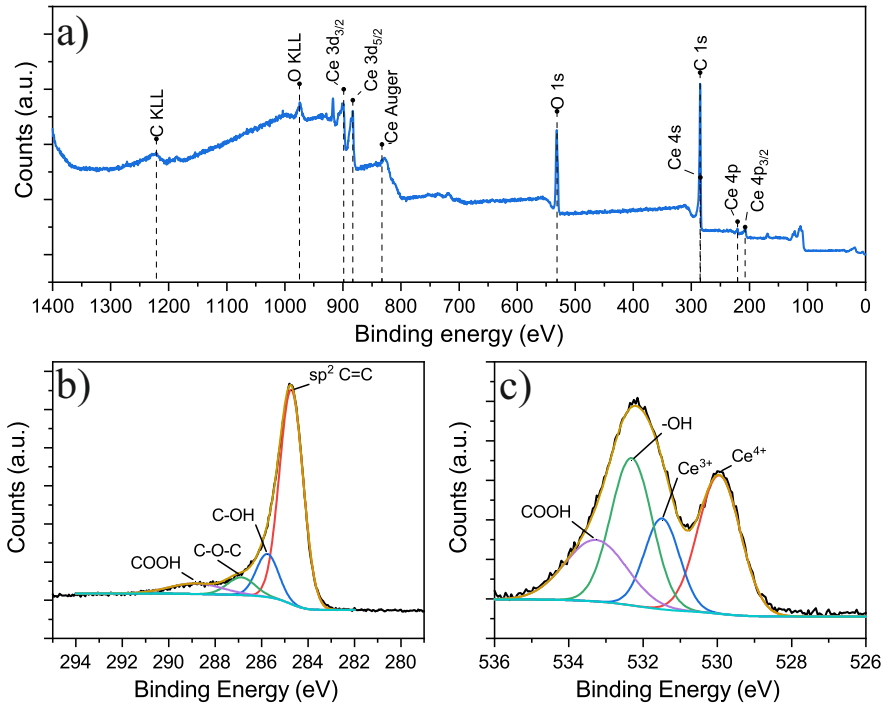


FIGURE 4.6: (a) Wide XPS spectra and fitting curves of high-resolution (b) C 1s and (c) O 1s spectra of the sample GO-CNT-Ce-515.

(532.15 eV) and carboxyl (533.2 eV) bonds [153, 226, 227]. From the integrated area of the Ce⁴⁺ and Ce³⁺ peaks, the relative content of Ce⁴⁺ is estimated at 61%.

For the elucidation of the Ce bonding states, Ce 3d_{3/2} and Ce 3d_{5/2} signals were deconvoluted. The six peaks labelled as v_0, v_1, v_2 (3d_{5/2}) and v'_0, v'_1 and v'_2 (3d_{3/2}) refer to the three pairs of spin-orbit doublets characteristic of Ce⁴⁺ 3d final states. Another two pairs of spin-orbit doublets u_0, u'_0 and u_1, u'_1 correspond to Ce³⁺ [228]. The contribution of these last doublets to the XPS spectrum of raw-CeO₂ NPs is lower, as compared to the spectrum of the GO-CNT-Ce-515 electrode (Fig. 4.7). This complex deconvolution does not allow obtaining a reasonable result. However, the contribution of Ce⁴⁺ can be estimated using the relation

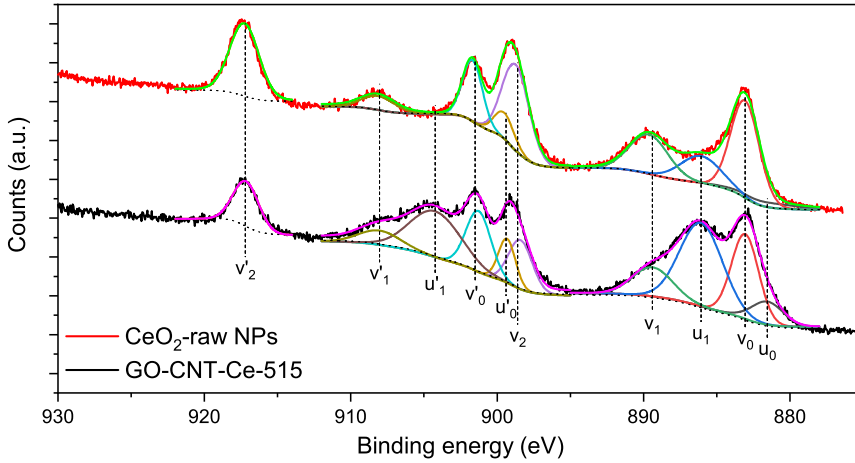


FIGURE 4.7: Ce $3d_{3/2}$ and Ce $3d_{5/2}$ high resolution XPS of GO-CNT-Ce-515 and CeO₂-raw NPs.

$$Ce^{4+} (\%) = \frac{v'_2\%}{14} \times 100 \quad (4.1)$$

where $v'_2\%$ is the percentage of v'_2 peak area respect to the total Ce 3d area, with the relative error in the range of 10% [229]. Using this relation, the percentage of Ce⁴⁺ for raw CeO₂ is 100%, as expected, and for GO-CNT-Ce-515 is 70%, compatible with the one obtained from the study of the O 1s band. The coexistence of both states leads to the presence of Ce₂O₃ and CeO₂ as determined with HRTEM analyses. Additionally, CeO_{2-x} intermediate states that contain partially reduced CeO₂ could be also present in the layers. Therefore, some of the initial NPs undergo reduction processes during the deposition, changing from Ce⁴⁺ to Ce³⁺ state. Given that stoichiometric CeO₂ is an insulator, this reduction is crucial for increasing the electronic conduction achieved with the diffusion through hopping mechanism of small formed polarons. Additionally, there is an improvement of the capacity of the ceria matrix to store and mobilise oxygen [227, 230].

The composition of the electrodes was further investigated by synchrotron-based FTIRM. Despite the reduced film thickness, intense synchrotron

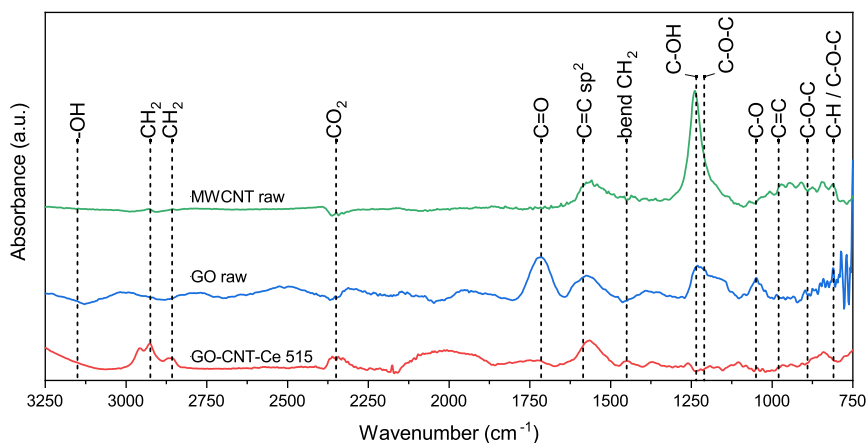


FIGURE 4.8: SR-FTIR spectra of samples MWCNT-raw, GO-raw and GO-CNT-Ce 515.

light source allowed to identify various characteristic bands in the trans-reflection operation mode. Fig. 4.8 shows the SR-FTIR of representative samples. GO-raw spectrum is composed by peaks situated at 810 cm^{-1} (attributed to C–H and/or C–O–C), 890 cm^{-1} (C–O–C), 1050 cm^{-1} (C–O alkoxy), 1210 cm^{-1} (C–O–C), 1235 cm^{-1} (C–OH) and 1715 cm^{-1} (C=O), corresponding to the oxygen containing functional groups of GO platelets. The spectrum also reveals a flatten band at 1600 cm^{-1} (C=C sp^2) [74, 231]. The C–OH line from the carboxylic functionalization is the dominant feature of the MWCNT-raw spectrum. However, the C=O band is not visible, and the C=C sp^2 bonds line of the carbon structure is slightly shifted towards lower wavenumbers as compared to the C=C line in the spectrum of the GO platelets [232].

The spectrum of the GO-CNT-Ce-515 sample reveals the presence of C=C sp^2 groups with a band located at 980 cm^{-1} as well as a broadband in the range $1560\text{--}1600\text{ cm}^{-1}$. The doublet peaks at 2857 cm^{-1} and 2925 cm^{-1} are ascribed to symmetric and antisymmetric stretching vibrations of $-\text{CH}_2$ and the peak at 1450 cm^{-1} is associated with $-\text{CH}_2$ bending [233, 234]. It has been reported that these groups, which are constituents of alkyl chains that could be formed during reconfiguration of GO to rGO, contribute to

the electrochemical performance [235]. However, this alkyl groups could be by-products not linked to the rGO. All of the oxygen-containing bands present in raw materials are reduced or are missing in the characteristic spectrum of the deposited sample, proving the reduction of GO platelets during the deposition process. The small bands located at 2350 cm^{-1} and assigned to CO₂ are present in all measured samples.

4.1.3 Electrochemical characterization

Voltammograms of the electrodes GO-Ce, CNT-Ce and GO-CNT-Ce-515 at 100 mV s^{-1} sweep rate are shown in Fig. 4.9a, b and c, respectively. The capacitive contribution from the total current measured using equation (2.4) is highlighted. Once again, the oxygen-evolution process in the aqueous electrolyte is responsible for the peak at *ca.* 0.8 V . The recorded voltammograms show quasi-rectangular shape and no presence of prominent peaks. This behaviour together with the main contribution of the capacitive current proves the capacitive (surface) processes as main charge storage mechanisms in the electrodes. The percentage of the capacitive contribution of all the fabricated samples at 100 mV s^{-1} is presented in Fig. 4.9d, confirming that the main contributions are surface processes. Fig. 4.9e shows the typical voltammograms of the electrode GO-CNT-Ce-515 for different sweep rates. The quasi-rectangular shape of the voltammograms is conserved with the sweep rate change. Considering the major contribution of surface processes, the volumetric capacitance can be calculated from CV data with the aid of equation (2.3). Fig. 4.9f shows the volumetric capacitance at different sweep rates for the four fabricated electrodes. Comparing the capacitance measured at 10 mV s^{-1} sweep rate, both GO-Ce and CNT-Ce electrodes disclose *ca.* 60 F cm^{-3} . However, the electrode containing MWCNT reveals lower energy storage for higher sweep rates, in agreement with the lower capacitive surface contribution from the total current, as presented in Fig. 4.9d. This result supports the ones from Chapter 3, revealing that the addition of MWCNT to GO-NiO system boosts the diffusive process, lowering the capacitance at high sweep rates. The addition

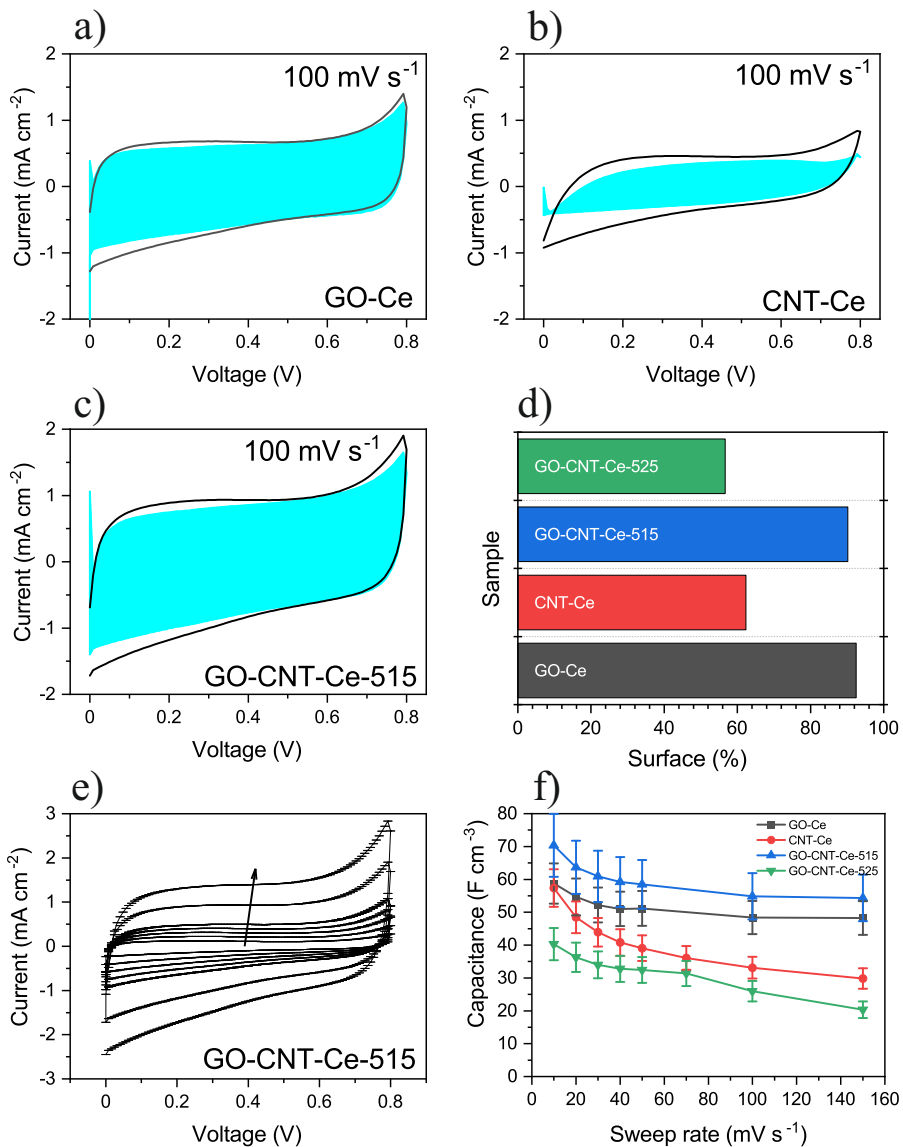


FIGURE 4.9: CV of the samples (a) GO-Ce, (b) CNT-Ce and (c) GO-CNT-Ce-515 at 100 mV s^{-1} with surface capacitance contribution highlighted in blue; (d) percentage of surface contribution in capacitance of the fabricated electrodes at 100 mV s^{-1} ; (e) CV curves of the sample GO-CNT-Ce-515 at sweep rate range 10 mV s^{-1} – 150 mV s^{-1} (arrow indicates the increasing sweep rate); (f) volumetric capacitance *vs.* sweep rate of the fabricated electrodes.

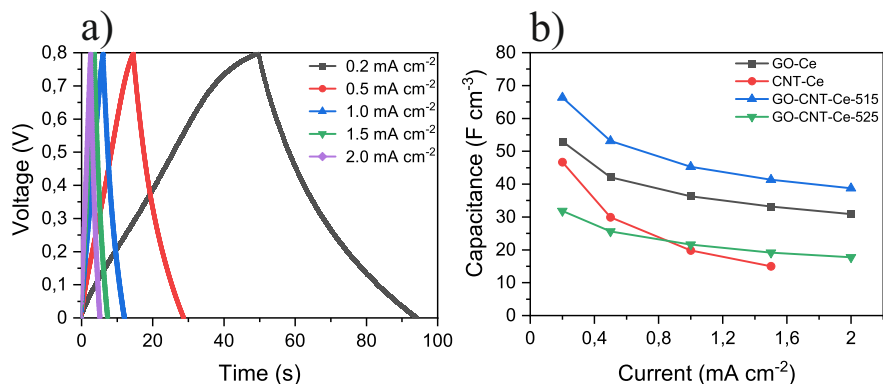


FIGURE 4.10: (a) Galvanostatic charge–discharge data of GO- CNT-Ce-515 for different applied currents; (b) volumetric capacitance vs. applied current density of all the fabricated electrodes.

of 1 *wt%* of MWCNT to GO-Ce dispersion, increases slightly the capacitance of the obtained electrode to *ca.* $70 F cm^{-3}$. In addition to enhance electron transport, the MWCNT increase porosity and prevent re-stacking of GO by broadening the spacing between GO sheets [236]. The addition of a higher concentration of MWCNT (2 *wt%*) reduces the capacitance to $40 F cm^{-3}$, due to the formation of nanotubes aggregates, hindering the access of the electrolyte ions to the active area of the electrode [236].

GCD measurements were acquired at current densities in the range of $0.2 - 2 mA cm^{-2}$. Fig. 4.10a depicts a typical charge-discharge curve and the quasi-linear voltage response with time that gives capacitive materials their distinctive triangular form. The decrease in the charge/discharge time with the increasing current can also be observed. The coulombic efficiency is around 97% for most current densities and it decreases to 90% for the lowest applied current values. As a result, there is practically no charge loss during operation. The volumetric capacitance was calculated using equation (2.5) and the results are represented in Fig. 4.10b. The measured capacitances are consistent with those calculated in CV data, reaching similar values for applied currents of $0.2 mA cm^{-2}$ and sweep rates of

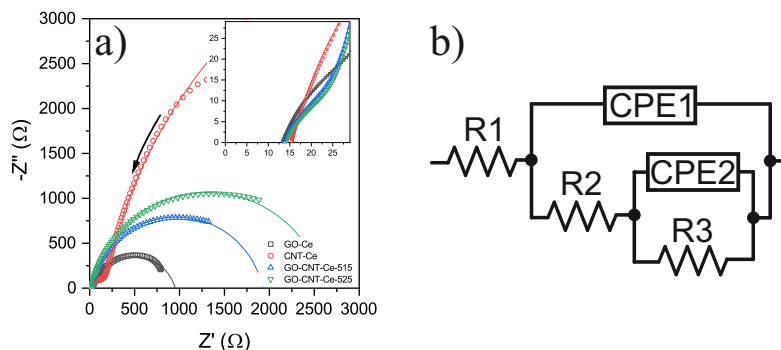


FIGURE 4.11: (a) Nyquist plot of the EIS measurement (points) and simulated data from the equivalent circuit (lines) of all the fabricated samples (the arrow indicates the direction of increasing frequency). Inset details the high frequency range; b) equivalent circuit for data fitting.

10 mV s^{-1} . Additionally, as applied density rises, capacitance decreases, resulting in quicker processes and less charge being stored.

The electrodes were also investigated through EIS measurements. The registered Nyquist plots are presented in Fig.4.11a. At high frequencies, EDL and charge-transfer reactions result in a characteristic partial semi-circle loop. At low frequencies, diffusion processes should be predominant. However, slower mechanisms could result in an additional semi-circle loop, shifting diffusion to lower frequencies. Hence, two distinct processes with their respective characteristic time may be differentiated in some electrodes with two unique semicircle plots. The equivalent circuit shown in Fig. 4.11b was used to fit all the curves, and the plots are shown as continuous lines in Fig. 4.11a. The equivalent circuit used is the same one as films containing imidazole from Chapter 3 (Fig. 3.12b), where a detailed explanation of their components was given. Table 4.2 summarizes the values of the elements for the equivalent circuit fitting of the EIS data. The films present a comparable ESR (or $R1$) values of about 14Ω . This resistance is the sum of the intrinsic resistance of electrodes and that of electrolyte besides the external wiring. The $R2$ (charge-transfer resistance)

TABLE 4.2: Fitting values for the elements of the equivalent circuit.

	R1 (Ω)	R2 (Ω)	R3 (Ω)	CPE1		CPE2	
				Y ($\mu S s^n$)	n	Y ($\mu S s^n$)	n
GO-Ce	13.4	51.4	886.1	25.8	0.82	36.0	0.84
CNT-Ce	15.4	225.3	10991	14.2	0.85	52.8	0.89
GO-CNT- Ce-515	13.8	30.7	1881.3	38.1	0.83	25.5	0.94
GO-CNT- Ce-525	14.4	25.7	2564.1	23.3	0.84	22.9	0.91

values of the electrodes are also comparable, with the exception of CNT-Ce electrode, which has a resistance one order of magnitude higher. It is worth noting that this electrode presented the highest decay of capacitance with the sweep rate (CV) and the current density (GCD) (Fig. 4.9f). Therefore, the high charge-transfer resistance of this film accounts for its slower storage of energy, decreasing its performance in fast charge-discharge processes. Warburg elements were negligible in the fitted model, indicating that the *R2* element is the one accounting for electrolyte diffusion contribution in the measured frequency range. Low charge leakage is indicated by *R3* (leakage resistance) values in the order of $k\Omega$. Regarding CPE, all *n* values are greater than 0.82, confirming the almost ideal capacitor behaviours.

4.2 Increase of electrochemical performance through combination of metal oxides

The maximum capacitance value of the electrodes containing CeO₂ NPs is higher as compared to their counterparts including NiO NPs in their composition (presented in Chapter 3). The capacitance of the electrodes can be further increased through different routes. It has been demonstrated that combining two or more metal oxide materials can improve electrical conductivity. Hence, better charge storage performances result from enhancing charge transfer [237]. Besides, the combination of metal oxides leads to different oxidation states enabling multiple redox reactions, enhancing rapid faradaic reactions with synergistic effects [238]. The study of the supercapacitive improvement of mixtures composed of two or more metal oxides has recently been the subject of numerous investigations. Among various metal oxides, manganese-based ones (MnO_x) are the most promising materials due to their superior electrochemical performance, low cost, abundance, structural diversity as well their environmentally friendly nature [239, 240]. Although MnO₂ was reported to have the best energy storage properties [241], MnO and Mn₃O₄ are also used as SC electrodes [242–245]. Storage performance of CeO₂ electrodes has been increased with the addition of Co [246] and ZnO [247]. Manganese oxide electrodes has been investigated in combination with Co₃O₄ [248], ZnO [249], Fe₂O₃ [250], Cu₂O [251], and different metal ions as cobalt, copper, nickel or chromium [252, 253]. Moreover, the synthesis of MnO_x and CeO₂ mixed oxide electrodes has been also reported, revealing outstanding storage performances [254–259]. In conclusion, the synergistic effect produced by combining cerium and manganese oxide materials could indicate a viable composite for supercapacitive devices.

4.2.1 Manganese acetate reaction with H₂O₂ for target preparation

Although MnO₂ has the best storage capability among manganese oxides, the acquisition of commercial MnO₂ NPs is not possible. However, MnO₂

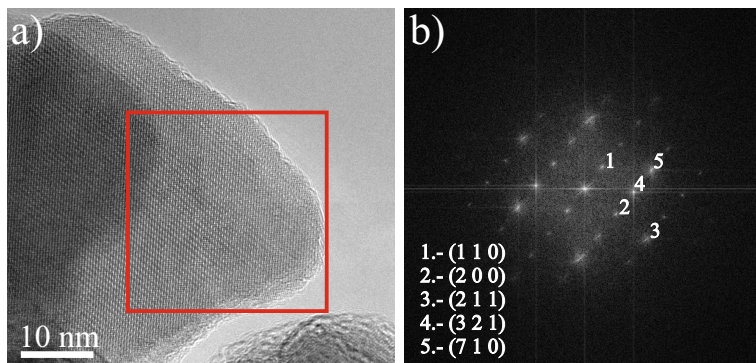
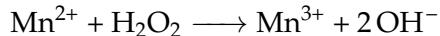
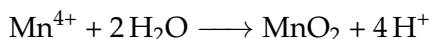
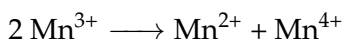


FIGURE 4.12: (a) HRTEM image of the crystals obtained as product of reaction of manganese acetate with H_2O_2 and (b) FFT of the selected region in (a).

can be synthesized using manganese acetate precursor [260] and hydrogen peroxide (H_2O_2) following the oxidation reaction:



where Mn^{3+} under alkaline conditions, is rapidly converted to MnO_2 as follows:



The target for RIMAPLE consisted in the preparation of a determined concentration of manganese acetate aqueous solution. H_2O_2 at 30% was added drop by drop sonicating at the same time. The reactions were performed with an open container due to its exothermic nature. Once all the H_2O_2 had entirely reacted, the container was closed and left sonicating for one hour. To prove the formation of the expected compound, HRTEM images of the produced crystals have been analysed. The crystal structure presented in Fig. 4.12 shows interplanar distances compatible with (110), (200), (321) and (211) MnO_2 (JCPDS 00-044-0141). The size of the structures is in the range of 10 to 50 nm. Following with the target

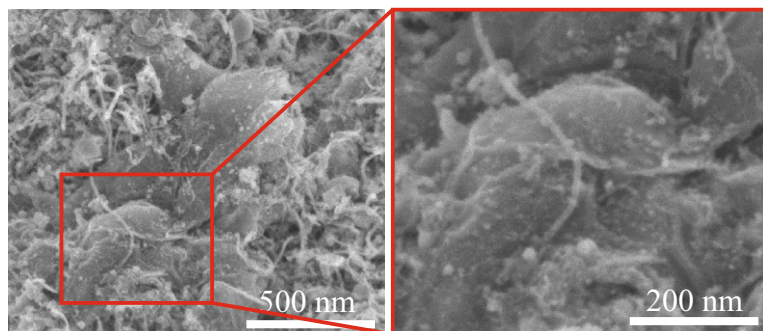


FIGURE 4.13: XHRSEM images of GO-CNT-Ce-Mn-5152-H₂O₂ electrode with magnified region on the right.

preparation, the solution was mixed with GO, MWCNT and CeO₂ NPs and stirred overnight. Before laser irradiation, the dispersion was sonicated for one hour. Two different electrodes were prepared using the concentration of the GO-CNT-Ce electrode with the highest storage capability (5 wt% of GO, 1 wt% of MWCNT and 5 wt% of CeO₂ NPs): one reacting 0.57M manganese acetate with H₂O₂ which corresponds to a 2 wt% to the total mass added (GO-CNT-Ce-Mn-5152-H₂O₂) and the second one, reacting 1.45M of acetate, corresponding to 5 wt% (GO-CNT-Ce-Mn-5155-H₂O₂). The morphology and composition of the electrode GO-CNT-Ce-Mn-H₂O₂-5152 was compared to the GO-CNT-Ce-515 electrode. Electrochemical properties of the electrodes were systematically investigated.

4.2.1.1 Morphological characterization

Under visual inspection the fabricated electrodes show homogeneous black colour. The black colour is caused by the carbon nanoentities, independently on the addition of other components. Compared to previous electrode layers, the thickness measured for the manganese containing electrodes is larger, although still in the micrometric range. GO-CNT-Ce-Mn-5152-H₂O₂ has a thickness of $2.3 \pm 0.2 \mu\text{m}$ whereas GO-CNT-Ce-Mn-5155-H₂O₂ is $2.3 \pm 0.5 \mu\text{m}$ thick. Both rGO platelets and MWCNT decorated with nanometric structures can be identified in the XHRSEM images of the

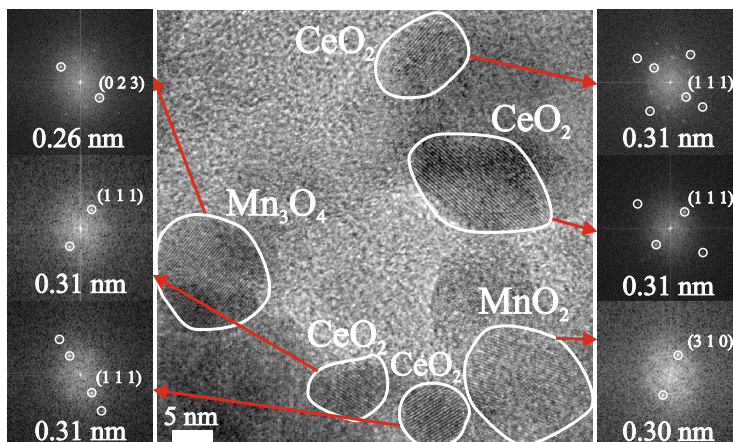


FIGURE 4.14: HRTEM images of GO-CNT-Ce-Mn-5152-H₂O₂ electrode and FFT patterns of the marked regions.

electrode (Fig. 4.13). HRTEM images (Fig. 4.14) reveal the presence of different crystalline structures. The measured interplanar distances of 0.31 nm , 0.19 nm and 0.16 nm are compatible with (111), (220) and (311) CeO_2 (JCPDS 00-004-0593). However, the interplanar distances of 0.31 nm could correspond also to the (310) lattice plane of MnO_2 (JCPDS 00-044-0141). The interplanar distance of 0.27 nm corresponds to (222) Mn_2O_3 (JCPDS 01-071-0636). This coexistence of different phases could be attributed to the mixture of Mn^{2+} and Mn^{3+} from material not completely oxidized besides Mn^{4+} from completely oxidized one. Additional HRTEM images demonstrate the presence of distances compatible also with Ce_2O_3 . In summary, HRTEM investigations reveal the coexistence of CeO_2 , Ce_2O_3 and Mn_2O_3 , whereas MnO_2 could be also present in the structure of the composite films.

4.2.1.2 Compositional characterization

XPS investigations were performed to disentangle the stoichiometry of the oxides formed in the composite electrodes and determine their relative concentrations. In Fig. 4.15a, the wide range XPS spectrum of the GO-CNT-Ce-Mn-5152-H₂O₂ electrode is presented. The spectrum is composed

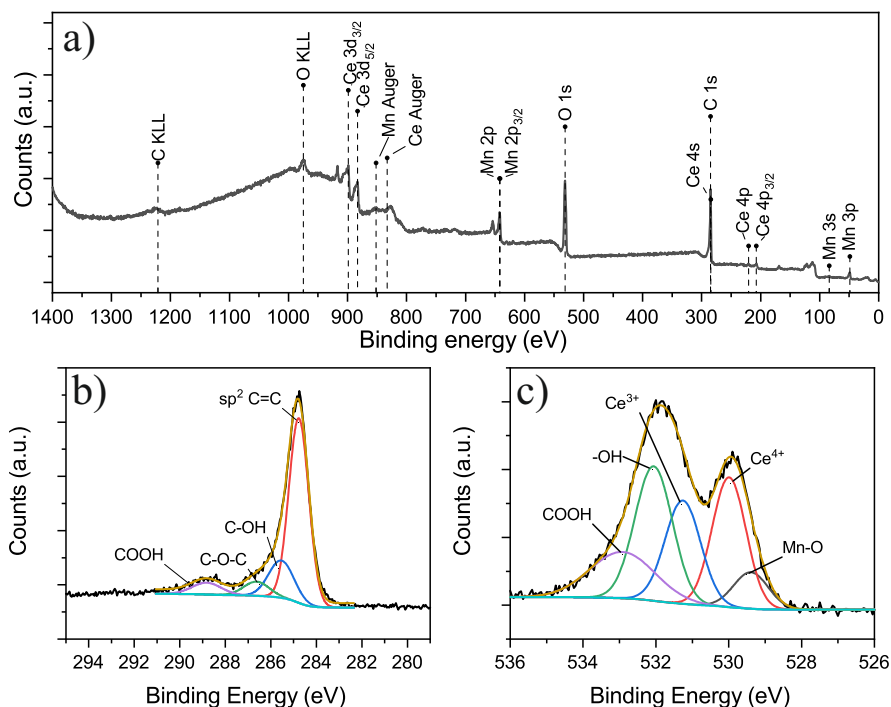


FIGURE 4.15: (a) Wide XPS spectra; (b) C 1s and (c) O 1s high resolution XPS peaks of the GO-CNT-Ce-Mn-5152-H₂O₂ electrode.

by the C, O, Ce and Mn. N from background gas is barely incorporated as in the prior Ce-containing electrodes. The C 1s high resolution peak (Fig. 4.15b) is similar to the C 1s peak of GO-CNT-Ce-515 electrode shown in Fig. 4.6b, consisting of a main contribution from sp²-bonded C=C and less intense lines corresponding to the remaining oxygen-containing groups of GO platelets. For the O 1s peak (Fig. 4.15c), the deconvolution includes the O²⁻ structural peak, related to Mn – O – Mn bond (529.39 eV) [261, 262] besides the Ce⁴⁺, Ce³⁺, hydroxyl and carboxyl bond contributions. The Mn – O peak is the most intense one in the O 1s spectra of the individual manganese oxide (*ca.* 80%). Therefore, the contribution of hydroxyl and water peaks from this compound to the fabricated composited film is negligible. The relative content of Ce⁴⁺ and Ce³⁺ can be calculated from

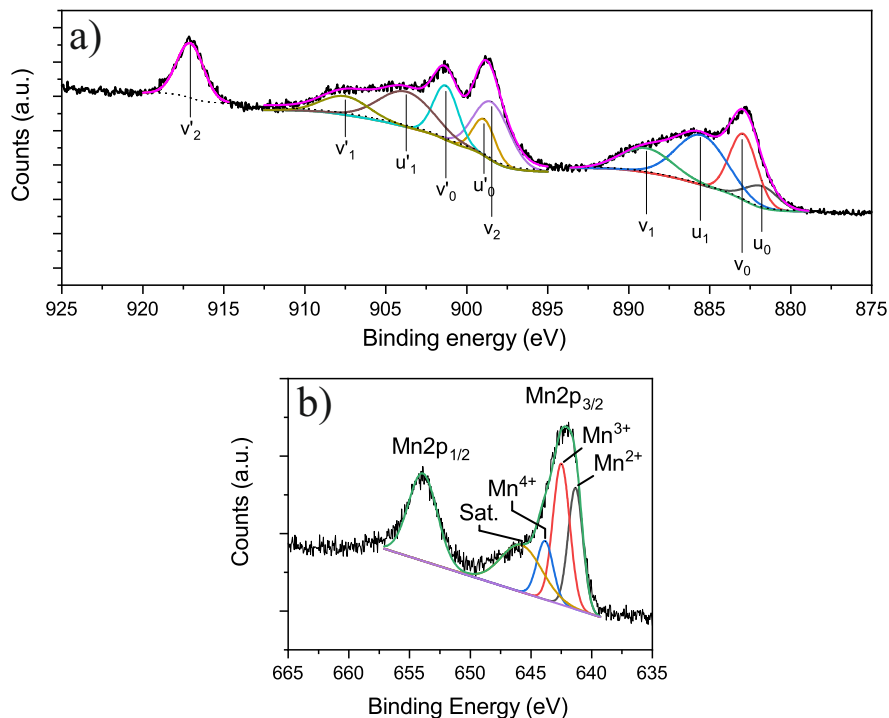


FIGURE 4.16: (a) Ce 3 d and (b) Mn 2 p high resolution XPS peaks of the GO-CNT-Ce-Mn-5152-H₂O₂ electrode.

the areal percentage of each peak, resulting in a 67% and 33% respectively. The 3 d_{3/2} and 3 d_{5/2} Ce lined were also deconvoluted (Fig. 4.16a). Using the equation (4.1), the percentage of Ce⁴⁺ for GO-CNT-Ce-Mn-5152-H₂O₂ is estimated at around 70%, similar to the value calculated from the O 1s line. Moreover, the value is similar also to that estimated for the electrode GO-CNT-Ce-515, proving that the addition of the manganese compound does not influence the reduction process of CeO₂ NPs during laser irradiation.

Through the deconvolution of the Mn 2 p peak, different MnO_x phases were identified and their relative percentages can be calculated. The Mn 2 p peak consists of two lines assigned to Mn 2 p_{1/2} and Mn 2 p_{3/2} (Fig. 4.16b). The Mn 2 p_{3/2} line is deconvoluted in peaks centred at 641.3 eV, 642.5 eV and 643.84 eV binding energies, corresponding to Mn²⁺, Mn³⁺ and Mn⁴⁺,

respectively, and a satellite peak at 645.7 eV [263, 264]. The slightly higher binding energies as compared to the values of pure stoichiometric MnO, MnO₂ and Mn₃O₄ [265], may indicate a strong interaction between manganese and cerium oxides [266]. The relative Mn²⁺, Mn³⁺ and Mn⁴⁺ content is calculated using the integrated area of the constituent peaks, without the satellite lines. The percentage of Mn²⁺ is 33.6%, Mn³⁺ is 47.6% and Mn⁴⁺ is 18.9%. Accordingly, the sample contains a mixture of MnO (9.8% Mn²⁺), Mn₃O₄ (23.8% Mn²⁺ and 47.6% Mn³⁺) and MnO₂ (18.9% Mn⁴⁺). The presence of these species is in agreement with HRTEM analyses. The predominance of Mn₃O₄ is confirmed by XPS analyses, consistent with HRTEM investigations. The existence of MnO₂ has been also proven.

4.2.1.3 Electrochemical characterization

The energy storage performance of the fabricated electrodes was studied through electrochemical measurements. The results were compared to the characteristics of electrodes containing GO, MWCNT and CeO_x (GO-CNT-Ce-515 electrode). In Fig. 4.17a, the CV curves of the sample GO-CNT-Ce-Mn-5155-H₂O₂ are presented at different sweep rates. Similarly to previous electrodes, the CV curves have a quasi-rectangular shape without the presence of prominent peaks. Despite the overlapping of CV curves, the main contributions to the total current calculated using equation (2.4) are still capacitive surface processes. Considering these characteristics, the equation (2.3) determines the volumetric capacitance. Fig. 4.17b shows the obtained results. The addition of 2 wt% of manganese acetate for the reaction with H₂O₂ does not improve significantly the storage capability as compared to GO-CNT-Ce-515. However, the increase of the manganese acetate concentration to 5 wt%, leads to a volumetric capacitance of *ca.* 110 F cm⁻³ @ 10 mV s⁻¹, as compared to around 70 F cm⁻³ of the GO-CNT-Ce-515 electrode. GCD measurements prove the quasi-linear voltage response with time (Fig. 4.17c). The coulombic efficiency is over 98% in all the applied current densities, hence, negligible charge is lost during the operation.

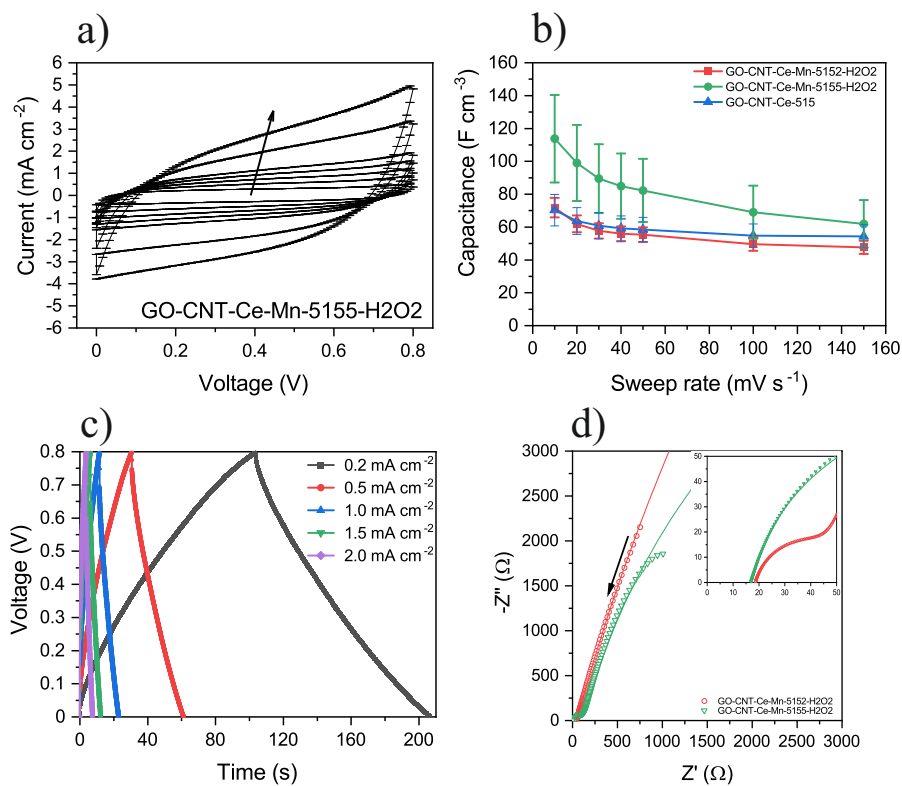


FIGURE 4.17: (a) CV curves of film GO-CNT-Ce-Mn-5155-H₂O₂ at sweep rate range 10 – 150 mV s⁻¹ (the arrow indicates the increasing sweep rate); (b) volumetric capacitance *vs.* sweep rate of the electrodes GO-CNT-Ce-Mn-5152-H₂O₂ and GO-CNT-Ce-Mn-5155-H₂O₂ with sample GO-CNT-Ce-515 for comparison; (c) GCD data of GO-CNT-Ce-Mn-5155-H₂O₂; and (d) Nyquist plot of EIS measurement (points) and simulated from equivalent circuit (lines) of the electrodes (the arrow indicates the direction of increasing frequency. Inset details the high frequency range).

TABLE 4.3: Fitting values for the elements of the equivalent circuit with the addition of manganese acetate and H₂O₂.

	R1 (Ω)	R2 (Ω)	R3 (Ω)	CPE1		CPE2	
				Y ($\mu S s^n$)	n	Y ($\mu S s^n$)	n
GO-CNT-Ce-Mn-5152-H2O2	18.8	35.8	46975	7.9	0.89	84.7	0.83
GO-CNT-Ce-Mn-5155-H2O2	17.1	146.46	14838	11.6	0.87	76.0	0.84

Finally, EIS measurements are presented as Nyquist plot in Fig. 4.17d with equivalent behaviour as the previously fabricated electrodes. For these samples, besides the semicircle loop at high frequencies of EDL and charge-transfer reactions, a quasi-linear straight line at low frequencies of diffusion processes can be identified. The circuit that fits the EIS data is the same as previous electrodes (Fig. 4.11b) and the fitting values are summarized in Table 4.3. As expected, the $R1$ is similar to previous ones (around 18Ω). Moreover, the fitted values of $R2$ are higher, especially for GO-CNT-Ce-Mn-5155-H₂O₂ electrode, causing a greater semicircle loop at high frequencies. This higher value could be associated with the incorporation of bigger manganese oxides nanostructures in the electrode [267], even though no evident changes are observed in HRTEM images. Leakage resistances ($R3$) are in the range of $k\Omega$ accounting for low leakages. As to CPE, n values are higher than 0.84, and as a consequence both electrodes can be considered almost ideal capacitors. It is important to point out the increase of Y value of $CPE2$ compared to previous electrodes and to the corresponding $CPE1$. This fact points to the enhancement of the pseudocapacitance with the manganese oxide incorporation. In summary, it has been proved that the addition of manganese oxide species increases the total capacitance by pseudocapacitive processes.

4.2.2 Electrodes prepared from GO platelets, MWCNT, CeO₂ NPs and manganese acetate target solutions

In the procedure described in the previous section the main goal was to obtain MnO₂ NPs in the target dispersion, previously to laser irradiation, through the reaction of manganese acetate with H₂O₂. In parallel experiments, the possibility to synthesize MnO_x NPs through direct laser irradiation of manganese acetate in addition to the CeO₂ NPs and the carbon-based material was also investigated. Fortunately, MAPLE technique allows the deposition of metal oxide NPs using aqueous solutions of metal organic precursors (acetates) in the frozen targets [144]. Therefore, the UV photon energy and the resulting temperature rise are sufficient to cause the acetate groups to decompose under the action of the laser pulses, allowing the free metal ions to form oxide nanostructures inside the target before the material is ejected.

More precisely, during the RIMAPLE deposition procedure, the laser radiation absorbed by the molecules of manganese acetate has sufficient energy to break the Mn – O bond of the acetate (photodissociation process) [140]. However, prior studies found that in the reactive MAPLE process, photothermal pathways dominate the decomposition of acetates. Additionally, the deposition of these compounds can be restricted by a water explosive boiling temperature lower than that of acetate decomposition [144]. Even though, during the RIMAPLE deposition, the energy required to reach the decomposition temperature of the Mn acetate is originating from heat transfer from GO, MWCNT and CeO₂ NPs. These structures rapidly heat the matrix surrounding them over the temperature needed for acetate decomposition (over 600 K) [268, 269]. Thermal simulations prove that the temperature reached in a radius of *ca.* 200 nm around CeO₂ NPs aggregates (Fig. 4.1b), GO and MWCNT would be sufficient to cause the molecules of manganese acetate to decompose resulting in the crystallization of Mn oxides. Additionally, photochemical processes can occur producing manganese oxide species with different stoichiometries [270].

TABLE 4.4: Relative concentration of precursors in the aqueous dispersions for RIMAPLE targets composed of GO, MWCNT, CeO₂ NPs and Mn(CH₃COO)₂.

Target dispersion	Composition
GO-CNT-Ce-Mn-5151	5 wt% GO, 1 wt% MWCNT, 5 wt% CeO ₂ NPs, 1 wt% Mn(CH ₃ COO) ₂
GO-CNT-Ce-Mn-5152	5 wt% GO, 1 wt% MWCNT, 5 wt% CeO ₂ NPs, 2 wt% Mn(CH ₃ COO) ₂
GO-CNT-Ce-Mn-5155	5 wt% GO, 1 wt% MWCNT, 5 wt% CeO ₂ NPs, 5 wt% Mn(CH ₃ COO) ₂

Three different targets for the electrodes fabrication were prepared maintaining the concentration of GO, MWCNT and CeO₂ NPs of the GO-CNT-Ce electrode with the best electrochemical performance (Table 4.4). The deposition conditions, detailed in Chapter 2, consisted on the accumulation of 6000 pulses at 0.4 J cm^{-2} laser fluence on the frozen targets, being the ejected material deposited over stainless steel substrates placed at 4 cm separation distance.

4.2.2.1 Morphological characterization

The fabricated electrodes presented a measured thickness of $1.3 \pm 0.2 \mu\text{m}$ for GO-CNT-Ce-Mn-5151, $1.3 \pm 0.2 \mu\text{m}$ for GO-CNT-Ce-Mn-5152 and $1.4 \pm 0.3 \mu\text{m}$ for GO-CNT-Ce-Mn-5155. In the XHRSEM images (Fig. 4.18a), the evenly distribution of the GO platelets and MWCNT, can be clearly identified, and they appear decorated with nanostructures. It is anticipated that Mn ions dissolved in boiling water will produce manganese oxide crystallites, producing nanostructures of various sizes in the fabricated electrode. Both Ce- and Mn-based nanostructures can be found on the carbon nanoentities, as revealed by HAADF-STEM and EDX analysis (Fig. 4.18b). It is visible that both Mn and Ce nanostructures are mixed up but without sharing position. Therefore, there is no proof that mixed oxides were

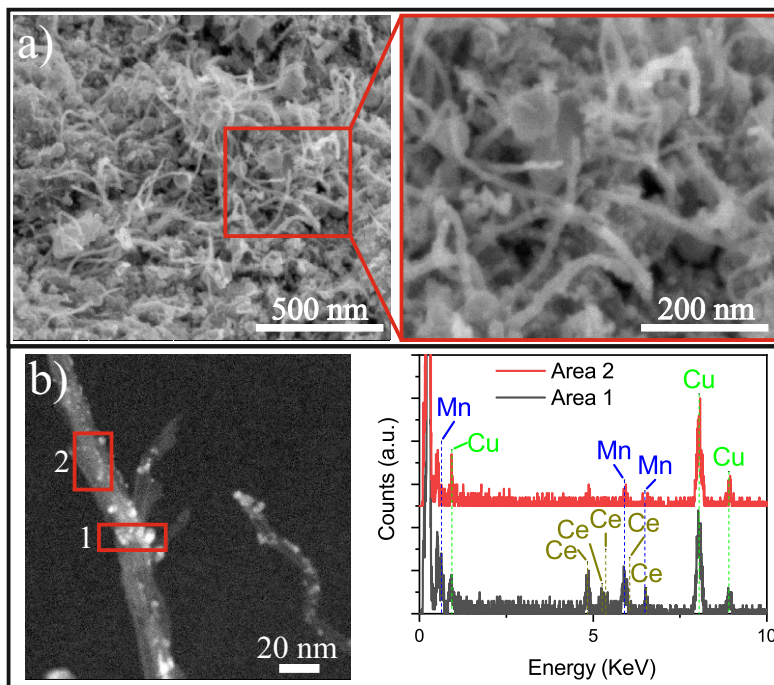


FIGURE 4.18: (a) XHRSEM images of GO-CNT-Ce-Mn-5152 with magnified region on the right; (b) HAADF-STEM image of a nanotube in GO-CNT-Ce-Mn-5152 with EDX spectra of the depicted regions.

formed during the deposition process. The average size of the Ce NPs (region 1) is around 2.8 nm and that of Mn NPs (region 2) is around 1.7 nm. HRTEM image in Fig. 4.19 reveals different crystal structures. Both CeO_2 and Ce_2O_3 are observed, similarly to the crystal structures identified in the ternary GO-CNT-Ce electrode. Simultaneously, the FFT patterns indicate the presence of MnO (JCPDS 04-005-4310) and Mn_3O_4 (JCPDS 01-075-0765) crystal structures. These results confirm that original acetate decomposes during laser irradiation, followed by oxides formation through recrystallization mechanisms. Moreover, due to the presence of two distinct oxidation states (Mn^{2+} and Mn^{3+}) in Mn_3O_4 that were not present in the original compound (only Mn^{2+} in the acetate), it can be stated that Mn suffers oxidation when exposed to laser irradiation.

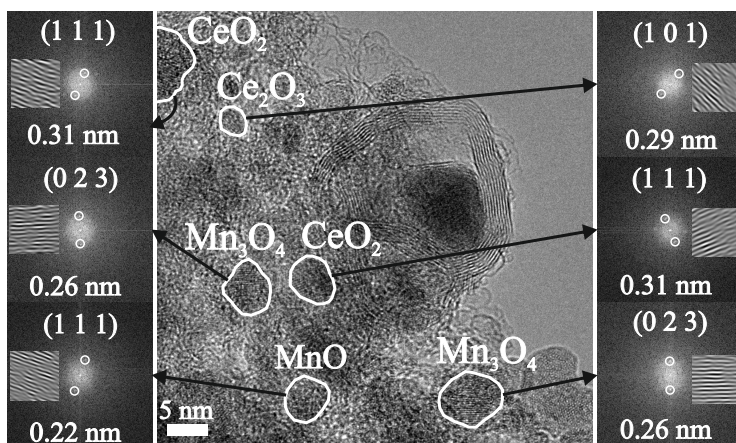


FIGURE 4.19: HRTEM image of GO-CNT-Ce-Mn-5155 with FFT and filtered lattices of the specified regions.

4.2.2.2 Compositional characterization

XPS analyses were performed in order to further investigate the chemical composition and chemical bonding states in the composite electrodes. Wide range XPS spectrum of the electrode GO-CNT-Ce-Mn-5152 is similar to that registered for the GO-CNT-Ce-Mn-5152-H₂O₂ electrode (Fig. 4.15a). The C 1s peak (Fig. 4.20a) is also comparable to that of GO-CNT-Ce-515 (Fig. 4.6b), having the main contribution from sp^2 -bonded C=C and low intensity lines of oxygen-containing groups. The O 1s peak (Fig. 4.20b) includes the lines of Mn – O – Mn bonds, as well as the Ce^{4+} , Ce^{3+} , hydroxyl and carboxyl bonds, similarly to that of GO-CNT-Ce-Mn-5152-H₂O₂ electrode (Fig. 4.15c). The relative content of Ce^{4+} is about 71%. Using the equation (4.1), the corresponding deconvolution of Ce 3d spectrum (Fig. 4.20c) reveals around 78% of Ce^{4+} , compatible with the value extracted from O 1s peak and similar to that of GO-CNT-Ce-515. Therefore, the addition of the Mn metal organic precursor to the target dispersion does not alter the reduction process of CeO_2 NPs. The Mn 2p peak (Fig. 4.20d) follows an equivalent deconvoluted configuration to that of GO-CNT-Ce-Mn-5152-H₂O₂ (Fig. 4.16b). As in the previous analyses, the

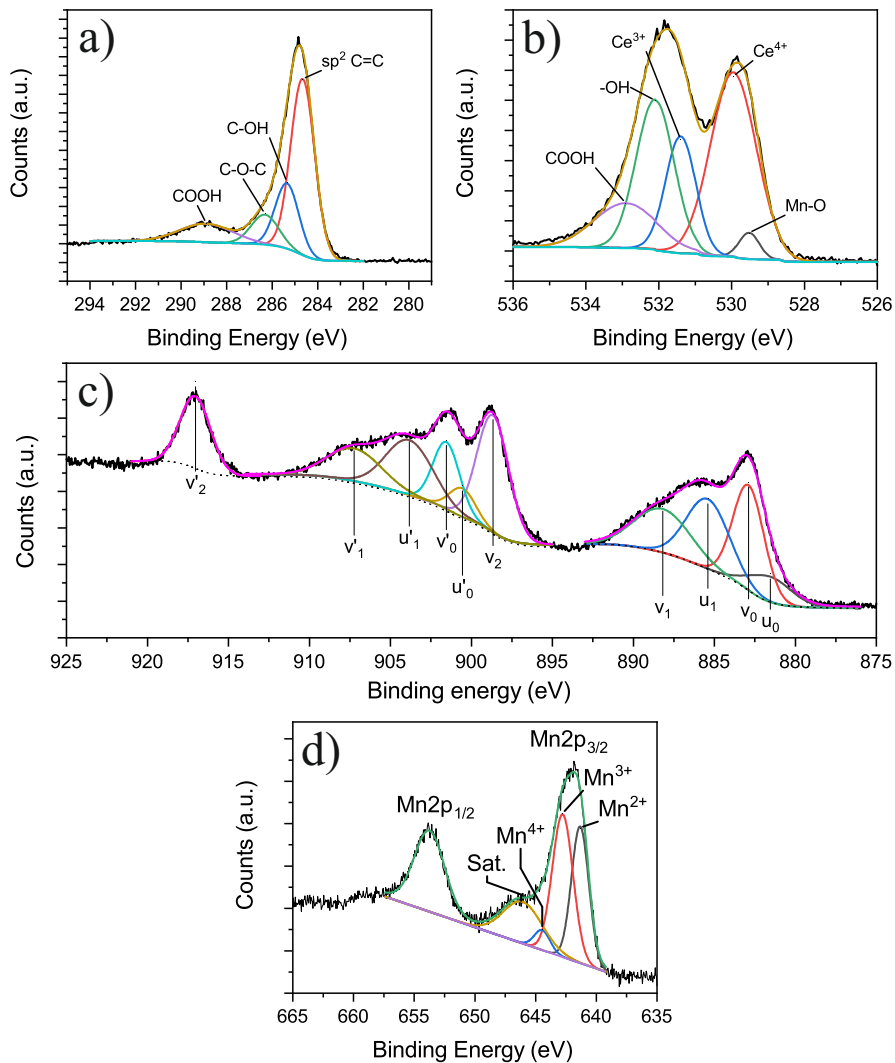


FIGURE 4.20: (a) C 1s, (b) O 1s, (c) Ce 3d and (d) Mn 2p high resolution XPS peaks of the GO-CNT-Ce-Mn-5152 electrode.

location of the peaks at higher binding energies than in the raw oxides may be caused by a strong interaction between cerium and manganese oxides. Although more local techniques such as EDX may point to the formation of separated Mn and Ce oxides without sharing position, larger-scale XPS analyses suggest some cation mixing. The percentage of Mn²⁺, Mn³⁺ and Mn⁴⁺ are 42.7%, 51.3% and 6.0%, respectively. Therefore, the electrode contains a combination of MnO (17.0% Mn²⁺), Mn₃O₄ (25.7% Mn²⁺ and 51.3% Mn³⁺) and MnO₂ (6.0% Mn⁴⁺) oxide stoichiometries. As compared to the electrode obtained from target dispersions containing MnO₂ NPs, the increase of MnO and decrease of MnO₂ is manifested, while the Mn₃O₄ concentration in the electrodes remains constant.

4.2.2.3 Electrochemical characterization

The obtained voltammograms (Fig. 4.21a) exhibit quasi-rectangular shape without presence of prominent redox peaks, being capacitive processes the main charge storage mechanism. The dominance of surface capacitive processes can be deduced also using equation (2.4) from the voltammogram taken at 100 mV s⁻¹ sweep rate (Fig. 4.21b). Accordingly, the percentage of the capacitive contribution to the total current is represented in Fig. 4.21c. Regarding GO-CNT-Ce-Mn-5155 electrode, k_1 and k_2 terms might not be calculated with a sufficient accuracy due to lack of linearity of equation (2.4) in most of the voltage values. The coefficient of determination, R^2 , is calculated for the linear fit $i(v, V)/v^{1/2}$ vs. $v^{1/2}$ for each voltage value and it is depicted in Fig. 4.21e. As an example of this, the voltage at 0.3475V is presented where the experimental points do not follow a straight line. Thus, no simple mechanisms would account for the origin of the k_1 , k_2 sweep rate dependence. This behaviour was attributed to the “porous-electrode” dispersion effect [200, 201] explained in Chapter 3. Despite the anomalous behaviour of this specific sample, for other electrodes the main contributions are surface processes. Interestingly, with the addition of Mn oxides, the diffusive component increases (Fig. 4.9d), despite their pseudocapacitive behaviour [30]. Fig. 4.21d shows the volumetric capacitance at different sweep rates using equation (2.3) for the

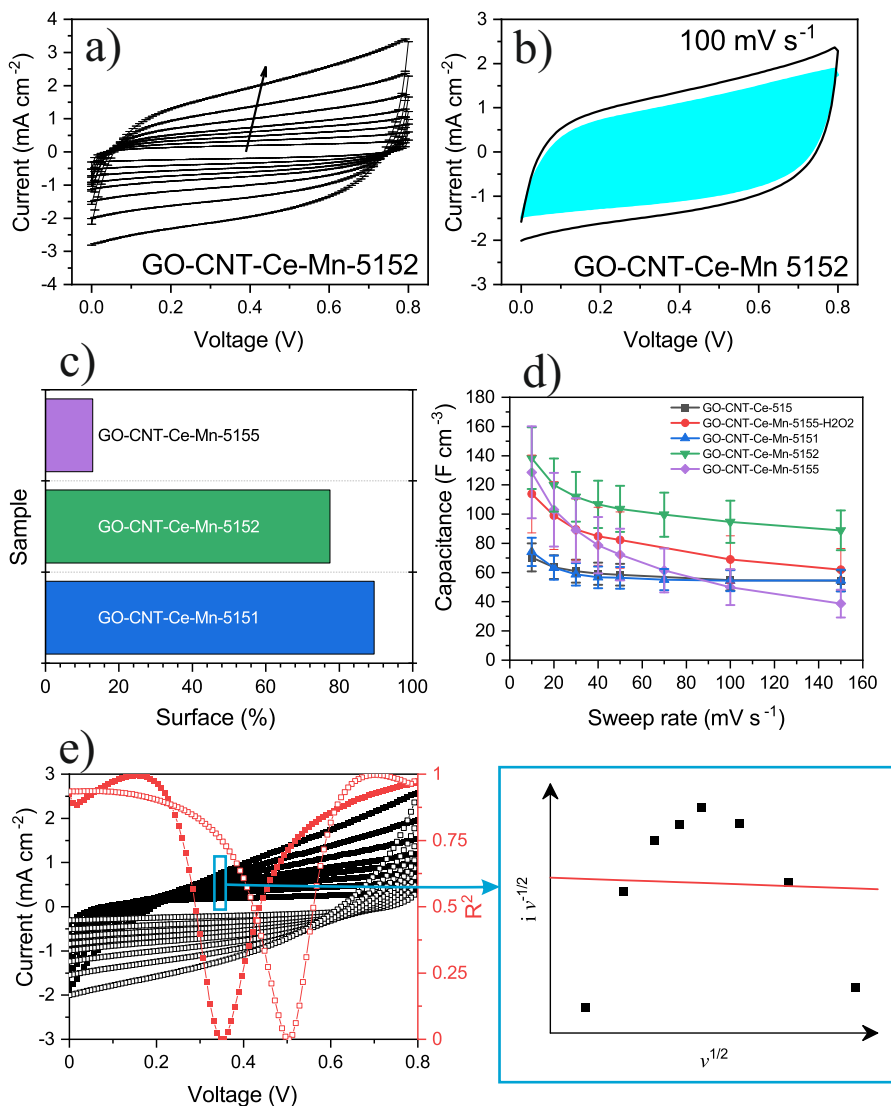


FIGURE 4.21: (a) CV curves of GO-CNT-Ce-Mn-5152 electrode at sweep rate range $10 - 150 \text{ mV s}^{-1}$ (the arrow indicates the increasing sweep rate); (b) CV curve at 100 mV s^{-1} with highlighted surface capacitance contribution; (c) percentage of surface capacitance contribution at 100 mV s^{-1} ; and (d) volumetric capacitance *vs.* sweep rate of the electrodes. (e) CV curves of GO-CNT-Ce-Mn-5155 electrode at sweep rate range $10 - 150 \text{ mV s}^{-1}$ with corresponding R^2 of the linear fit $i(v, V)/v^{1/2}$ *vs.* $v^{1/2}$ at each voltage value. The fitting at 0.3475 V is used as an example of the non-linearity of this fitting.

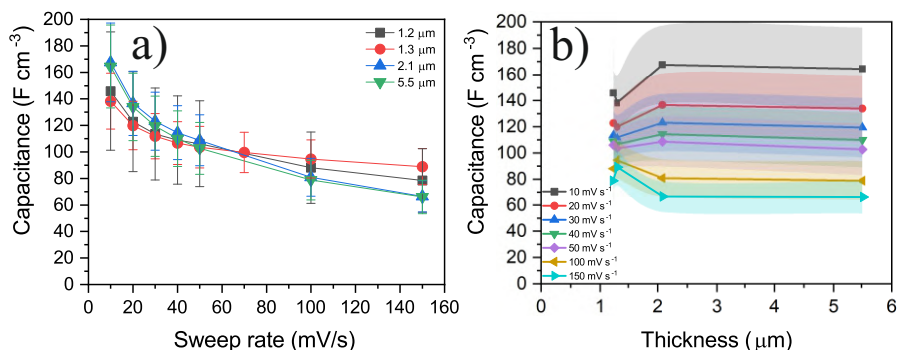


FIGURE 4.22: (a) Volumetric capacitance *vs.* sweep rate of GO-CNT-Ce-Mn-5152 for diverse thicknesses and (b) volumetric capacitance *vs.* thickness for different sweep rates.

different electrodes. For comparison, the electrodes with the highest storage performances GO-CNT-Ce-515 and GO-CNT-Ce-Mn-5155-H₂O₂ have been added to this plot. As can be observed, the addition of MnO_x rises the capacitance in all cases. With the addition of only manganese acetate with a manganese acetate/CeO₂ NPs relative concentration of 1/5, the capacitance reaches *ca.* 75 F cm⁻³ @ 10 mV s⁻¹. Increasing the amount of manganese oxide precursor to 2/5 and 5/5 relative concentration, the capacitance boosts to *ca.* 140 F cm⁻³ and 130 F cm⁻³, respectively. A higher decay in capacitance at faster sweep rates is observed for the electrode obtained with the highest amount of manganese oxide precursor. Similarly to CNT-Ce electrode, this behaviour results from an increase of the diffusive contribution, which suggests either the mobility limitation of electrolyte ions or the extrinsic pseudocapacitive nature of manganese oxides (MnO, MnO₂ and Mn₃O₄) [242–245, 252, 271, 272]. Comparing to the GO-CNT-Ce-Mn-5155-H₂O₂ electrode, an increase of capacitance value of almost 15% is observed, proving the effectiveness of the direct synthesis method.

Layers with larger thickness values, in the micrometric range, may decrease their capacitance as some path for the electrolyte diffusion can be blocked reducing the active surface area. To test this behaviour, thicker electrodes had been fabricated, increasing the original thickness of 1.2 μm

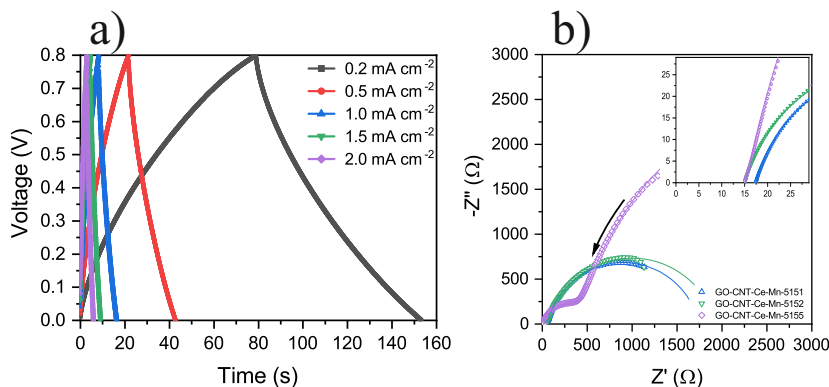


FIGURE 4.23: (a) GCD data of GO-CNT-Ce-Mn-5152; and (b) Nyquist plot from EIS measurements (points) and simulated from equivalent circuit (lines) of the electrodes (the arrow indicates the direction of increasing frequency. Inset details the high frequency range).

up to $5.5 \mu\text{m}$ with the accumulation of successive deposition processes. No relevant variation of the volumetric capacitance with thickness of electrode was observed (Fig. 4.22a). This result proves the good diffusion of the electrolyte ions towards the active surface (Fig. 4.22b).

GCD analyses of GO-CNT-Ce-Mn-5151/-5152/-5155 electrodes reveal the triangular charge-discharge response and a coulombic efficiency around 98% proving negligible charge lost during operation (Fig. 4.23a). The volumetric capacitance values calculated using equation (2.5) are similar to the values obtained from the CV curves for similar applied currents (Fig. 4.21d). EIS results obtained from these electrodes are presented in Fig. 4.23b as Nyquist plots. The carbon-based porous electrode response is similar to that of previous samples, especially to GO-CNT-Ce electrodes where two different processes with different characteristic times could be identified (Fig. 4.11a). The equivalent circuit used for fitting is depicted in Fig. 4.11b, the same used for previous electrodes, and the fitting values are listed in Table 4.5. The calculated $R1$ resistances are in the range $15 - 17\Omega$, similar to the values of electrodes presented in Tables 4.2 and 4.3. The $R2$ components are also similar to the values calculated for previous

TABLE 4.5: Fitting values for the elements of the equivalent circuit with the addition of manganese acetate as metal organic precursor

	R1 (Ω)	R2 (Ω)	R3 (Ω)	CPE1		CPE2	
				Y ($\mu\text{S s}^n$)	n	Y ($\mu\text{S s}^n$)	n
GO-CNT-Ce-Mn-5151	17.5	64.8	1659.9	16.3	0.86	63.6	0.87
GO-CNT-Ce-Mn-5152	15.1	63.3	1855.3	14.4	0.87	77.8	0.84
GO-CNT-Ce-Mn-5155	15.2	525.8	6447.4	10.6	0.88	83.0	0.88

samples, with the exception of the GO-CNT-Ce-Mn-5155 electrode, significantly higher than previous results. The consequence of this difference could be addressed similarly as in the case of CNT-Ce electrode, where it was observed a higher decay of capacitance at faster sweep rates, or GO-CNT-Ce-Mn-5155-H₂O₂ electrode where it was associated with bigger manganese oxide nanostructures incorporated. R_3 resistances are all in the range of $k\Omega$, thus low current is leaked. CPE elements can be considered as almost ideal capacitors, n values being higher than 0.86 in all fittings. As in the case of GO-CNT-Ce-Mn-5152-H₂O₂ and GO-CNT-Ce-Mn-5155-H₂O₂ electrodes, the Y magnitudes of $CPE2$ are higher than that of $CPE1$ and are significantly larger as compared to the electrodes without Mn oxide. These results confirm that incorporation of MnO_x leads to the increase of the pseudocapacitance contribution and consequently, the storage performance of the electrodes.

4.2.2.4 Device fabrication and performance study

A symmetric electrochemical capacitor fabricated with two facing GO-CNT-Ce-Mn-5152 electrodes was assembled to test the performance of the best volumetric capacitance. Fig. 4.24a shows the typical voltammograms for different sweep rates. The shape of the voltammograms is similar to that

registered for the single electrode (Fig. 4.21a). The calculated volumetric capacitance for different sweep rates (CV) and current (GCD) reaches *ca.* $25 F cm^{-3} @ 10 mV s^{-1}$ in both cases (Fig. 4.24b and c). For the calculation, the total volume of the active materials has been used. The Ragone plot is shown in Fig. 4.24d where equations (2.6) and (2.7) were used to calculate the volumetric energy and power densities, using the total volume of active material. These last results are presented together with different energy storage devices (comprising the current collectors, the active material and the separator) [79, 171] including also the results presented in Chapter 3, related to NiO containing electrodes. The improvement in both power and energy densities over the prior RIMAPLE symmetric N-doped GO-NiO device (GO-NiO-imi) must be emphasized, highlighting the similar thickness of electrodes involved. Although there is a decay in both parameters compared to those of GO-imi symmetric device, the submicrometric thickness of that device will not escalate correctly to practical performances for the explanation previously discussed. The fabricated rGO-MWCNT-CeO_x-MnO_x capacitor exhibits power and energy densities, up to $5.4 W cm^{-3}$ and $2.2 mWh cm^{-3}$, respectively. The stability of the device has been also studied by GCD cycling at *ca.* $2 mA cm^{-2}$ current density (Fig. 4.24e). The capacitance retention and the coulombic efficiency decay *ca.* 10% after 20000 cycles, maintaining the triangular charge-discharge shape practically unaltered (Fig. 4.24e, inset). The decay is presumably related to electrolyte drying process for poorly sealed devices. Nevertheless, the improved stability of this devices have been demonstrated, doubling the number of cycles of previous experiments.

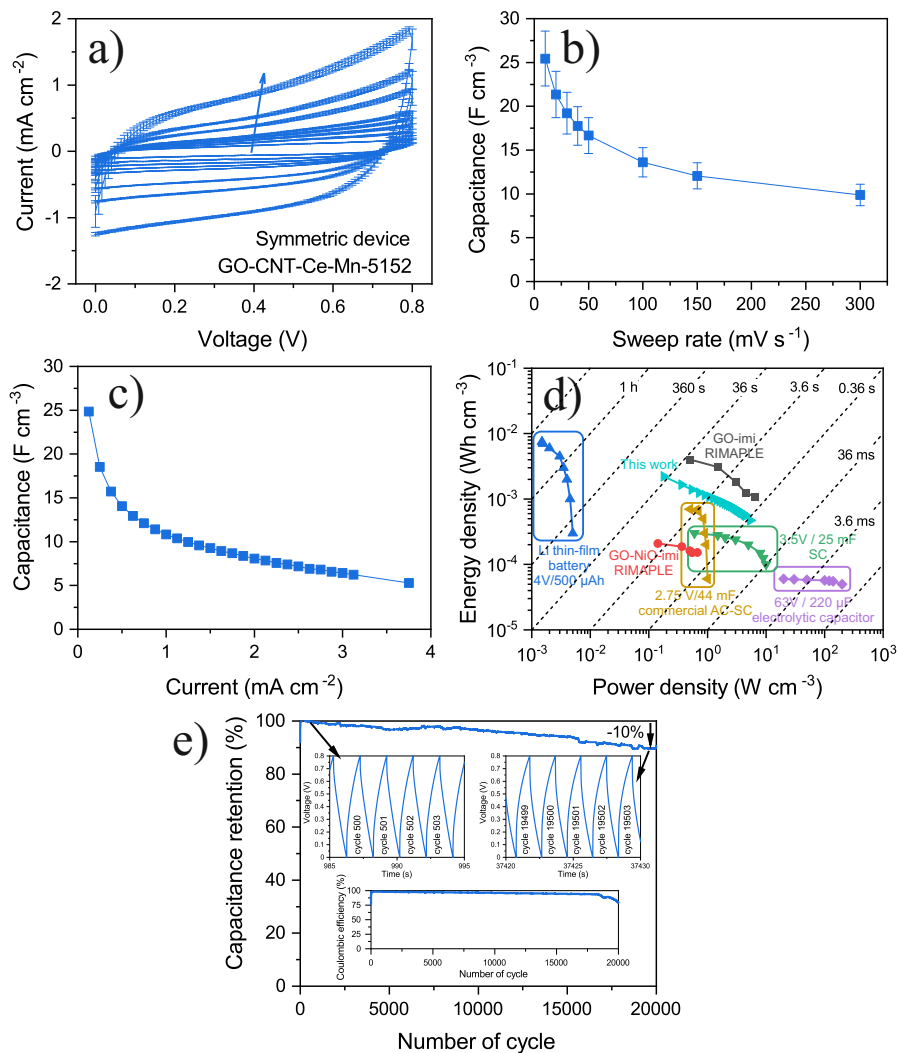


FIGURE 4.24: (a) CV curves at sweep rate range 10 – 150 mV s^{-1} (arrow indicates the increasing sweep rate), (b) volumetric capacitance *vs.* sweep rate and (c) volumetric capacitance *vs.* applied current of a symmetric device GO-CNT-Ce-Mn-5152. (d) Ragone plot of the fabricated SC device compared with commercially available energy storage systems. Data for Li battery, 3.5 V/25 mF supercapacitor (SC) and 6.3 V/220 μF electrolytic capacitor [171], data for the 2.75 V/44 mF activated carbon supercapacitor (AC-SC) [79] and GO-NiO-imi and GO-imi symmetric devices from Chapter 3. (e) Capacitance retention with charge-discharge zoomed regions (superior insets) and coulombic efficiency (inferior inset).

4.3 Organic electrolyte for energy increase

Considering that the energy of electrochemical devices is proportional to the squared of the operating voltage as seen in equation (2.6), a simple method to obtain high energy storage devices is to increase the operating voltage. Compared to aqueous solutions, electrolytes composed of a salt dissolved in an organic solvent offer a wider electrochemical stability window, in detriment of lower ionic conductivity and specific capacitance. Quaternary ammonium salts are frequently employed in organic electrolytes, being tetraethylammonium tetrafluoroborate (TEABF₄) dissolved in acetonitrile (ACN) the most used salt for commercial supercapacitors [12].

In this section, further performance studies of an asymmetric GO-CNT-Ce-Mn-5152/AC supercapacitor are presented using 1 M TEABF₄ dissolved in ACN as electrolyte instead of the previous aqueous 1 M Na₂SO₄ solution. As these electrochemical tests are performed using Swagelok-type cells, the electrodes are deposited over circular stainless steel substrates with a diameter of 12 mm. In order to study the voltage window of the single electrode, the Swagelok cells were assembled in a three-electrode configuration, placing the working composite electrode opposed to the thick activated carbon electrode and using a Ag wire as reference. As the thickness of the composite electrode is much lower than the AC one, GO-CNT-Ce-Mn-5152 acts as limiting current electrode and the results are only referred to it.

CV measurements were performed increasing the voltage window in small steps to avoid deterioration of the electrolyte and/or electrodes, until a certain voltage produces irreversible reactions. The electrodes reach up to +1.3 V and down to -1.6 V vs. Ag reference, allowing a voltage window of $\Delta V = 2.9$ V. In Fig. 4.25a, the voltammograms with the determined voltage window is presented for different sweep rates. As observed in the CV plot, the quasi-rectangular shape is still maintained despite the presence of small bulges caused by reversible surface redox reactions. Using equation (2.4), the contribution of surface capacitance can be differentiated

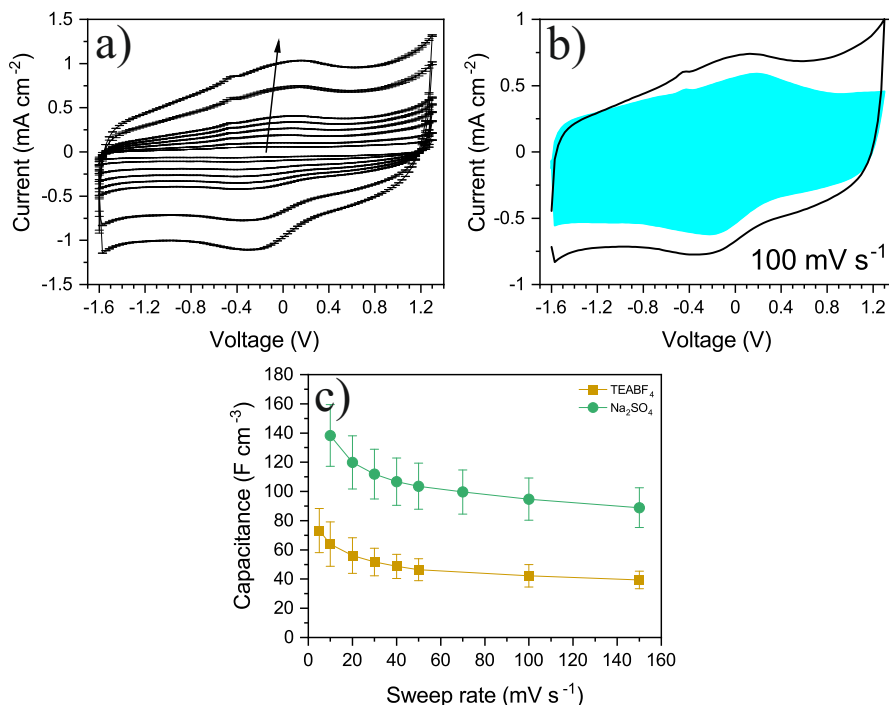


FIGURE 4.25: (a) CV curves of electrode at sweep rate range 5 mV s^{-1} – 150 mV s^{-1} (arrow indicates the increasing sweep rate) and (b) CV curve at 100 mV s^{-1} with highlighted surface capacitance contribution of GO-CNT-Ce-Mn-5152 with 1 M TEABF_4 dissolved in ACN. (c) Volumetric capacitance *vs.* sweep rate of GO-CNT-Ce-Mn-5152 electrode with aqueous and organic electrolyte.

(Fig. 4.25b). As can be observed, the main contribution to the total current are surface processes. Hence, using equation (2.3) the volumetric capacitance can be calculated (Fig. 4.25c). The volumetric capacitance of the same electrode using aqueous electrolyte is also represented in Fig. 4.25c. With the organic electrolyte, the capacitance has drop to *ca.* 75 F cm^{-3} @ 5 mV s^{-1} . Charge-discharge measurements were performed in the current density range of 0.09 – 1.6 mA cm^{-2} (Fig. 4.26), revealing the triangular profile, even in long cycles, with a coulombic efficiency of *ca.* 100%.

Once established the working voltage window of the electrode in the organic TEABF₄/ACN electrolyte, a symmetric device was assembled. To

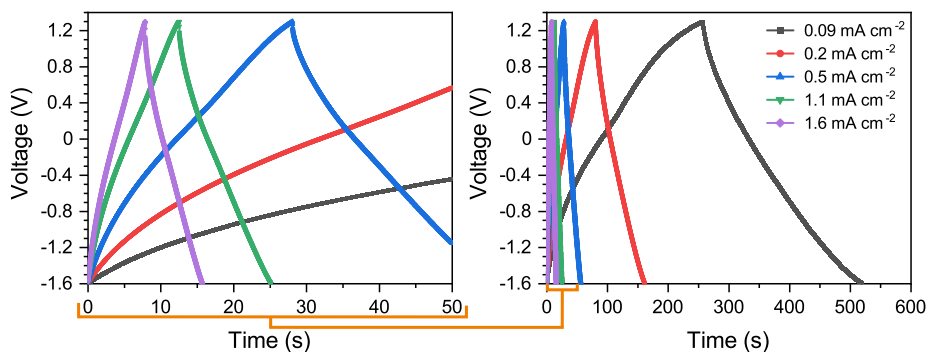


FIGURE 4.26: GCD measurement of electrode GO-CNT-Ce-Mn-5152 with organic electrolyte. In left plot a zoomed region of shorter charge-discharge cycles is depicted for better visualization.

avoid significant deterioration upon cycling, the voltage window was limited to $\Delta V = 2.8 \text{ V}$. The electrochemical investigations were performed using a Swagelok cell with a two-electrode set-up, facing two GO-CNT-Ce-Mn-5152 electrodes. GCD measurements were performed in the current density range of $0.06\text{--}0.6 \text{ mA cm}^{-2}$ and display the triangular profile without any presence of bulges (Fig. 4.27a). The charge-discharge profiles are the last cycle of 100 consecutive cycles, at each different applied current density. The capacitance remains constant after a few cycles of stabilization while the coulombic efficiency is *ca.* 95%, indicating that almost no charge is lost during operation, similarly to the single electrode measurements. The calculated specific energy and power densities, using the total active material, are presented in the Ragone plot shown in Fig. 4.27c together with the performances of other storage devices (considering the current collectors, active material and separator) [79, 171] as well as previous results, including also GO-imi, GO-NiO-imi and GO-CNT-Ce-Mn-5152 devices assembled using aqueous electrolyte. The increase in energy density is outstanding as compared to $1 \text{ M Na}_2\text{SO}_4$ aqueous electrolyte, reaching an energy density up to 16 mWh cm^{-3} , while maintaining a similar power density of 4.5 W cm^{-3} .

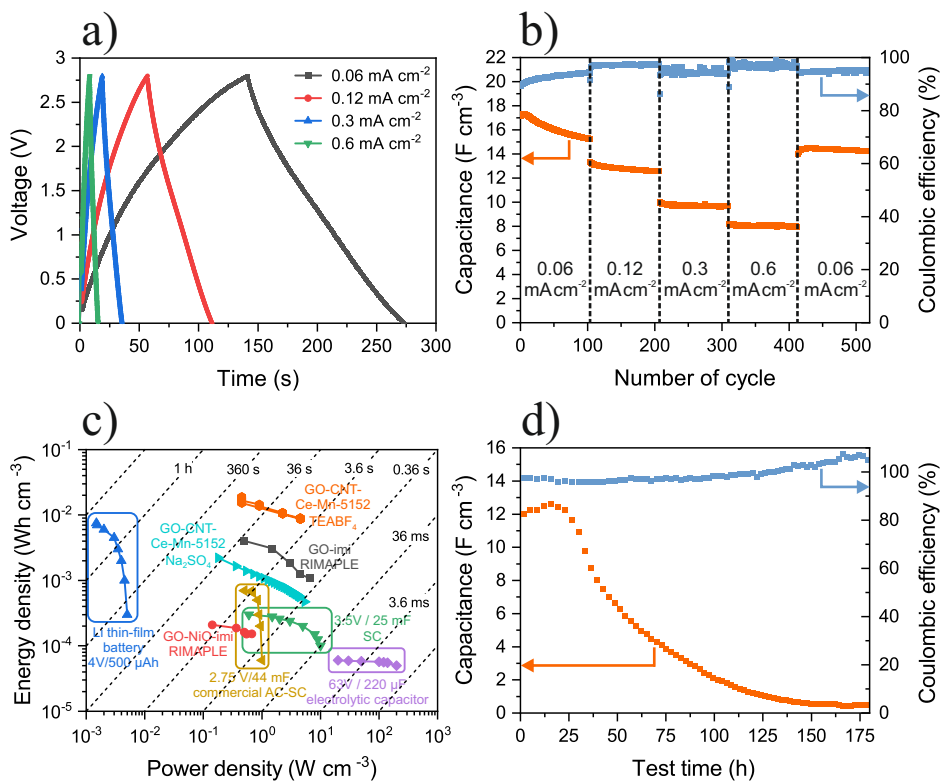


FIGURE 4.27: (a) GCD measurements and (b) calculated volumetric capacitance and coulombic efficiency of each cycle at different applied current densities of symmetric GO-CNT-Ce-Mn-5152 device with TEABF₄/ACN electrolyte. (c) Ragone plot of the fabricated GO-CNT-Ce-Mn-5152 device with TEABF₄/ACN electrolyte compared with commercially available energy storage systems and GO-NiO-imi, GO-imi and GO-CNT-Ce-Mn-5152 symmetric devices with aqueous electrolyte. (d) Capacitance and coulombic efficiency calculated during the float test of the device under study.

Float potential stability tests were also carried out for the assembled device, holding the potential at 2.8 V for 2 h, after sequences of 50 charge/discharge cycles at 0.12 mA cm^{-2} between 0 – 2.8 V. The capacitance and coulombic efficiency are calculated during the charge-discharge step and the results are plotted in Fig. 4.27d. It is important to emphasize that this test conditions are extremely challenging and stressful for the devices, which could cause significant changes in the electrode material. Although the capacitance decreases a 50% after 50 h of operation, the coulombic efficiency remains at almost 100%, indicating no charge losses during operation.

Tests with identical voltage upper limits involving constant voltage hold are more demanding than conventional cycling tests. Additionally, the cycling test typically requires longer times than the float potential test before a clear stability result is defined [273]. Therefore, these results may indicate promising stability results even with the high decrease of the capacitance as the cycling test presented in Fig. 4.24e was concluded after *ca.* 10 hours. However, this float test was not possible to replicate with aqueous electrolyte device due to poor sealing causing premature drying before degradation of the electrodes and/or electrolyte. Swagelok cells could overcome this sealing issue, but aqueous electrolyte cannot be used in this type of cell material as chemical reaction may occur.

4.4 Conclusions

Composites constituted by carbon-based materials and cerium oxides were successfully synthesised using RIMAPLE technique. The rGO-MWCNT-CeO_x composite discloses higher volumetric capacitance as compared to composites containing NiO NPs. The change of composition did not affect the main contribution of surface storage processes. The optimization with the amount of MWCNT was also performed. The results indicated that the aggregation of MWCNT led to the decrease of the storage performance at higher concentration values.

A different route for electrochemical performance enhancement was followed, including simultaneously different metal oxides in the carbon-based composites. For that goal, two different pathways were tested, being the addition of metal acetate to the target dispersions the most promising one. The new composite fabricated with carbon-based material, CeO₂ NPs and manganese acetate in the target dispersion disclosed considerably higher volumetric capacitance as compared to the rGO-MWCNT-CeO_x electrode. Compositional analyses revealed the coexistence of different oxides of the both metals present, enhancing the energy storage capability of the composite through synergistic effects. A symmetric SC was assembled with two GO-CNT-Ce-Mn-5152 electrodes and aqueous electrolyte. The improvement in both energy and power density of this device compared to the previous GO-NiO-imi SC was clear. Although, there was a slight decrease of storage capacity as compared to GO-imi device, the larger thickness and structural stability of the new composite allowed for better scalability to thicker electrodes and better stability upon cycling.

Finally, the GO-CNT-Ce-Mn-5152 electrode and a symmetric SC based on this electrode were tested using an organic electrolyte substituting the aqueous electrolyte. The increase of the voltage window was significant, reaching up to 2.8 V, preserving the device capacitive performance. This voltage window increase led to a considerable gain in energy density, even higher than the optimized GO-imi device. Float potential stability tests were also performed in the symmetric device with organic electrolyte revealing promising results.

Chapter 5

General Conclusions

Reactive inverse MAPLE is a technique with high potential for the fabrication of functional graphene-based composites for supercapacitors. This deposition method was successfully used for the development of composites based on reduced graphene oxide, multiwall carbon nanotubes and nanoparticles of nickel, cerium and manganese oxides.

Electrodes composed of rGO were fabricated and their electrochemical properties were improved with the addition of NiO NPs. The obtained electrodes displayed rGO sheets decorated with NiO nanostructures and disclosed an areal capacitance of $5 \text{ mF cm}^{-2} @ 10 \text{ mV s}^{-1}$, five times higher than rGO only electrodes, and a volumetric capacitance of 5 F cm^{-3} . The energy storage capabilities were further increased with the addition of multiwall carbon nanotubes, to increase mesoporosity. The resulting electrodes showed the carbon nanotubes as well as the rGO sheets decorated with NiO nanostructures and the capacitance boosted up to 20 F cm^{-3} .

The nitrogen-doping of the nanocarbon materials was induced by the incorporation of nitrogen-containing molecules to the RIMAPLE target dispersion. Different N-containing groups were achieved for each of the nitrogen precursor molecules. The capacitance of the electrodes with nitrogen-doped nanocarbon reached *ca.* $120 \text{ F cm}^{-3} @ 10 \text{ mV s}^{-1}$ without using carbon nanotubes, although the submicrometric thickness of the electrodes hinders their practical use. Regarding the electrodes including MWCNT, the capacitance doubled by the inclusion of nitrogen groups in the carbon structures. The structural studies pointed out that the significant increase

of capacitance is associated an increase of porosity in the carbon nanoentities at the nanoscale.

Electrodes composed of rGO, MWCNT and cerium oxide nanoparticles were also fabricated. Similarly to NiO-containing electrodes, rGO and MWCNT were decorated with cerium oxide nanostructures with different sizes. Different oxide species were identified, including CeO_2 and Ce_2O_3 . This composite disclosed superior performance than its counterpart with NiO, reaching *ca.* $70 \text{ F cm}^{-3} @ 10 \text{ mV s}^{-1}$.

The rGO-MWCNT- CeO_x electrodes were further improved with the addition of manganese oxides, obtaining synergistic effects from this combination. The addition of manganese acetate to the target material caused the deposition of different manganese oxide nanostructures decorating both rGO and MWCNT, including MnO , Mn_3O_4 and MnO_2 phases. The volumetric capacitance was incremented up to *ca.* $140 \text{ F cm}^{-3} @ 10 \text{ mV s}^{-1}$, the highest capacitance that we obtained with aqueous electrolyte thus far. The rGO-MWCNT- CeO_x - MnO_x electrodes were scalable to thicker electrodes preserving their electrochemical properties unaltered. Studies using an organic electrolyte with these electrodes tolerated the widening of the voltage window of operation from 0.8 V to 2.8 V , allowing for an energy density increase for the operating devices.

To conclude, several devices were assembled for testing the real application of the deposited electrodes. Successful symmetric systems were fabricated composed of nitrogen-doped rGO with and without NiO nanoparticles using an aqueous electrolyte. Additionally, a symmetric device based on rGO-MWCNT- CeO_x - MnO_x was tested with both aqueous and organic electrolytes revealing a significant increase in energy density with the organic electrolyte, and preserving high power. The good stability of the supercapacitors was validated allowing thousands of cycles and hours of operation under demanding conditions.

RIMAPLE laser technique proved its potential for the versatile fabrication of SC electrodes, as an alternative to conventional methods. The tuning of the initial target dispersion composition allows the development of complex multicomponent films with different structural and functional

properties. Moreover, the myriad of applicable materials has no limitations as both organic and inorganic compounds are usable.

Nonetheless, some limitations emerge from this laser-based technique. Micrometric-thick electrodes are fabricated in a 10 minutes deposition process. These kind of electrodes could be desirable for microsupercapacitor devices. However, prolonged fabrication times are required for the deposition of tens of microns thick electrodes necessary for large commercial SCs, hindering a plausible market development. Additionally, the equipment configuration allows producing homogeneous electrodes up to $2 \times 2 \text{ cm}^2$ in size due to small size of the MAPLE target as well as plasma confinement issues. Nevertheless, larger electrodes, up to several cm^2 , are desirable for commercial applications. To overcome these issues, a different deposition chamber with optimized configuration should be used, as well as a high power high-repetition-rate UV laser source. Moreover, the SCs using aqueous electrolytes could not reach full stability potential due to the drying of the electrolyte. Thus, the effective sealing of the devices needs to be addressed for obtaining better results.

Further research could be focused on the synergistic combination of nanoparticles with metallic acetates in the MAPLE targets for obtaining electrodes with higher performance. Currently, the best combination accomplished uses cerium and manganese oxides. However, different mixing of oxides could be beneficial for achieving better materials. Moreover, more effective nitrogen doping of the carbon-based materials could further increase the performance of the electrodes. Thus far, only symmetric devices have been assembled, although asymmetric devices could benefit from both electrode materials, increasing the voltage window of operation or even combining different storage mechanisms (supercapattery). Finally, the tuning of the electrolyte may enhance the energy storage performance of the final device. Therefore, focus on this field could also contribute with better performances.

Appendix A

COMSOL simulation and material properties

A.1 COMSOL simulation

COMSOL Multiphysics is a powerful interactive and integrated simulation environment used to model and solve different scientific and engineering problems. The analyses can easily be extended from conventional models for one type of physics into multiphysics models that solve coupled physics phenomena.

The description of the laws of physics for space- and time-dependent problems are usually expressed in terms of partial differential equations (PDE). However, for the vast majority of geometries and problems, these PDE cannot be solved with analytical methods. Instead, an approximation of the equations can be constructed, typically based upon different types of discretization. These discretization methods approximate the PDE with numerical model equations, which can be solved using numerical methods. The solutions to the numerical model equations are an approximation of the real solution to the PDE. The finite element method (FEM), used by COMSOL software simulations analyses, is used to compute these approximations. FEM subdivides the system into smaller elements by the discretization of the dimensional space, implemented by the construction of a mesh. Then, the PDE are solved in each of these limited regions taking into consideration the boundary conditions.

The temperature evolution of the materials involved in RIMAPLE deposition process during laser irradiation was simulated considering only thermal mechanisms. All the structures were considered isotropic and solid materials. The simulations were performed by solving the partial equation of a 2D transient heat conduction model

$$\rho C_p \frac{\partial T}{\partial t} - \nabla(k_{th} \nabla T) = Q \quad (\text{A.1})$$

where ρ is the material density, C_p is the specific heat capacity, T is the temperature, t is the time, k_{th} is the thermal conductivity and Q the heat source. This last Q parameter is defined as the energy input in a finite element caused by a laser pulse with Gaussian-like temporal evolution

$$Q = \frac{F}{\tau} e^{-4Ln(2)\left(\frac{t-\tau}{\tau}\right)^2} (1 - R) \alpha e^{-\alpha z} \quad (\text{A.2})$$

where F is the incident laser fluence, τ is the laser pulse duration, z stands for the spatial coordinate (depth in the absorptive material) and finally, R and α are, respectively, the reflectance and optical absorption coefficient of the corresponding compounds [138]. The first exponential term multiplied by $\alpha F/\tau$ describes the Gaussian-like temporal evolution of the pulse laser energy. The $(1 - R)$ term accounts for the percentage of radiation transmitted to the material, disregarding a percentage of absorbed light. Finally, the $e^{-\alpha z}$ describes the attenuation of the laser intensity in depth due to absorption.

The optical and thermophysical properties of the materials are listed in the next section. The heat equation is applied to all materials, in which the solvent material presents absorption $\alpha = 0$ (i.e. $Q = 0$). For a general understanding of the irradiation mechanisms underwent, simple geometries of GO sheets, NiO and CeO₂ NPs and aggregates of CeO₂ NPs were applied. GO was modelled as a continuous film of 10 nm thick. NiO was implemented as a 50 nm size squared NP (Fig. A.1) and CeO₂ as a 25 nm lateral squared size NP. Additionally, CeO₂ were also simulated as an aggregate of squared-shaped NPs. These geometries were placed within a

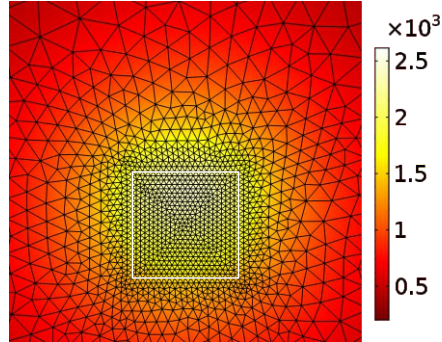


FIGURE A.1: Zoomed region of the 2D temperature map, in K , of single squared NiO NP of 50 nm lateral size (white square) at 5 ns from the start of the laser pulse. The discretization triangular elements where the PDE are solved is also included.

squared H_2O medium of $1\mu\text{m}$ size, transparent to radiation. The defined geometries can be observed in the left images of Fig. A.2.

Once the geometry for simulation is described, the definition of an appropriate mesh is a crucial step as it determines how the model is solved. The mesh establishes geometry divisions by defining shape, type, size, density, number and quality of the elements. In the simulations, free triangular elements were chosen with a maximum size 20 times lower than the main dimension of the material. Outside the material, the same elements were selected with a maximum size of 37 nm . The skewness measure is a suitable measure for most types of meshes. This quality measure is based on the equiangular skew that penalizes elements with large or small angles as compared to the angles in an ideal element. For the quality measures, a quality of 1 is the best possible and it indicates an optimal element. At the other end of the interval, 0 represents a degenerated element. The colour map in Fig. A.2 elucidates the quality of the mesh elements. Additionally, the histograms in Fig. A.2 show the amount of mesh elements for each skewness quality, tending in all simulated geometries to 1.

The simulation results in a 2D map of the temperature at each evaluated time. For the temperature *vs.* time plots, the temperature is calculated in a defined point in the middle of the geometry of each material under study.

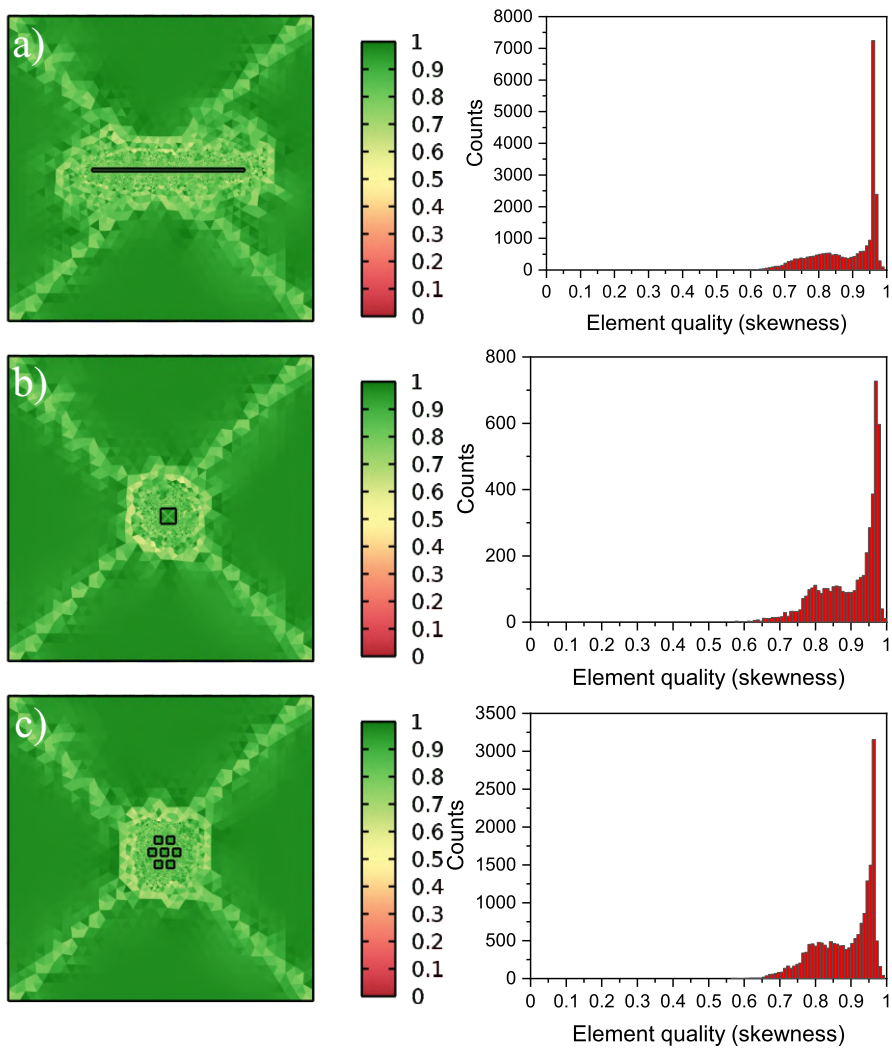


FIGURE A.2: Skewness quality measure 2D map and corresponding histogram of (a) GO, (b) NiONP and (c) CeO₂ NPs aggregate simulations with COMSOL.

A.2 Optical and thermophysical properties

In the following tables, the parameters of the materials implemented in the simulations are listed. The dependence of parameters with temperature is listed in specific tables when needed.

TABLE A.1: Density (ρ), specific heat (C_p), thermal conductivity (k_{th}), reflectance (R) and absorption coefficient (α) of the materials used for simulation.

Material	Parameter	Value
H ₂ O	ρ	917 kg m^{-3}
	C_p	$1400 \text{ J kg}^{-1} \text{ K}^{-1}$
	k_{th}	$3.5 \text{ W m}^{-1} \text{ K}^{-1}$
GO	ρ	917 kg m^{-3}
	C_p	$700 \text{ J kg}^{-1} \text{ K}^{-1}$
	k_{th}	$0.53 \text{ W m}^{-1} \text{ K}^{-1}$
	R	0.08
	α	$5.0 \cdot 10^6 \text{ m}^{-1}$
NiO	ρ	6670 kg m^{-3}
	C_p	see Table A.2
	k_{th}	see Table A.3
	R	0.2
	α	$5.0 \cdot 10^7 \text{ m}^{-1}$
CeO ₂	ρ	see Table A.4
	C_p	see Table A.4
	k_{th}	see Table A.4
	R	0.1
	α	$2.5 \cdot 10^7 \text{ m}^{-1}$

TABLE A.2: Temperature dependence of specific heat (C_p) of NiO used for simulation.

Temperature (K)	Specific heat ($J kg^{-1} K^{-1}$)
200	447.7
300	589.9
400	702.9
500	853.5
505	882.8
510	962.3
545	945.5
550	857.7
560	790.8
580	748.9
600	732.2
700	719.6
800	719.6
900	719.6
1000	719.6

TABLE A.3: Temperature dependence of thermal conductivity (k_{th}) of NiO used for simulation.

Temperature (K)	Thermal conductivity ($W m^{-1} K^{-1}$)
200	64.0
250	33.8
300	20.2
400	11.5
500	7.85
700	4.55
5000	4.5

TABLE A.4: Temperature dependence of thermophysical properties of CeO₂ used for simulation.

Temperature (K)	Density (kg m⁻³)	Specific heat (J kg⁻¹ K⁻¹)	Thermal conductivity (W m⁻¹ K⁻¹)
373	6763	386	6.220
423	6752	398	5.556
473	6740	406	5.164
523	6728	416	4.866
573	6717	425	4.529
623	6705	433	4.127
673	6693	435	3.824
723	6681	436	3.581
773	6669	437	3.397
823	6656	440	3.259
873	6644	442	3.138
923	6632	445	2.995
973	6620	449	2.896
1023	6607	452	2.816
1073	6595	457	2.720
1123	6583	459	2.634
1173	6570	461	2.567
1223	6556	462	2.458
1273	6542	465	2.390
1323	6529	467	2.315
1373	6516	470	2.217
1423	6504	472	2.151
1473	6491	475	2.088
1523	6481	478	2.029
1573	6472	480	1.973
1623	6463	483	1.920
1673	6453	485	1.870
1723	6441	488	1.823

Appendix B

Assignment of FTIR bands

TABLE B.1: Assignments of bands appearing in samples GO-CNT-NiO-515, GO-CNT-NiO-515-A, GO-CNT-NiO-515-U and GO-CNT-NiO-515-M.

	Wavelength (cm^{-1})	Assignment
GO	800	C – O – C or C – H
	890	C – O – C
	980	C = C
	1150	C – OH
	1550	C – C
	1640	C = C
	2900	OH
	3200	OH
MWCNT	1240	$\nu(C - O)$, C – OH
	1560	C – C
Urea	1150	ν_2 (or $2\nu_L$), C – OH
	1450	C – N, CN_2
	1600	C – N, CN_2 , N – H
	1680	O + NH, CO
	3250	NH
	3330	ν_{as} NH_2

Continued on next page

TABLE B.1 – continued from previous page

	Wavelength (cm^{-1})	Assignment
	3420	ν_{as} NH ₂
Melamine	800	δ_{oop} ring, δ_{twist} NH ₂
	1020	δ_{rock} NH ₂ , ν C – N(H ₂), δ_{ip} ring
	1200	δ_{rock} NH ₂
	1420	ν C – N(H ₂), δ_{ip} ring
	1530	δ_{sciss} NH ₂ , δ_{rock} NH ₂ , δ_{ip} ring
	1620	δ_{sciss} NH ₂
	3100	ν_s NH ₂
	3320	ν_{as} NH ₂
	3410	ν_{as} NH ₂
	3460	ν_{as} NH ₂
515	890	C – O – C
	1010	C = C
	1320	C – OH / C – O – C
	1530	C – N, CN ₂ , N – H
	1680	C = O
515-A	750	γ C – O, γ NH ₂ + CO out-of-phase
	950	Second vibrational mode of NH ₃
	1090	ν_2 (or $2\nu_L$) amorphous
	1260	C – OH, C – O – C
	1350	C – OH, C – O – C, $\nu_2 + \nu_L$ crystalline
	1510	C – N, CN ₂ , N – H
	1700	C = O
	1790	H – N – H scissoring
	3100	ν_s NH ₂

Continued on next page

TABLE B.1 – continued from previous page

	Wavelength (cm^{-1})	Assignment
	3530	N – H symmetric stretching
515-U	770	γ C – O, γ NH ₂ + CO out-of-phase
	810	C – O – C or C – H
	890	ν (C – N), CN ₂
	1100	C – O
	1210	NH
	1480	C – N, CN ₂ , N – H
	1600	C – O and NH ₂
	1700	O + NH, C – O
515-M	790	δ_{oop} ring, δ_{twist} NH ₂
	1100	C – O
	1240	δ_{rock} NH ₂
	1490	C – N, CN ₂
	1580	N – H
	1750	C = O

Bibliography

1. Simon, P. & Gogotsi, Y. Materials for electrochemical capacitors. *Nature materials* **7**, 845–854 (2008).
2. Pomerantseva, E., Bonaccorso, F., Feng, X., Cui, Y. & Gogotsi, Y. Energy storage: The future enabled by nanomaterials. *Science (New York, N.Y.)* **366**, 1–12. ISSN: 1095-9203 (2019).
3. Olabi, A. *et al.* Critical review of energy storage systems. *Energy* **214**, 118987. ISSN: 03605442 (2021).
4. Jiang, Y. & Liu, J. Definitions of Pseudocapacitive Materials: A Brief Review. *Energy and Environmental Materials* **2**, 30–37. ISSN: 25750356 (2019).
5. Wang, G., Zhang, L. & Zhang, J. A review of electrode materials for electrochemical supercapacitors. *Chemical Society Reviews* **41**, 797–828. ISSN: 14604744 (2012).
6. Yan, J., Wang, Q., Wei, T. & Fan, Z. Recent advances in design and fabrication of electrochemical supercapacitors with high energy densities. *Advanced Energy Materials* **4**, 1–43. ISSN: 16146832 (2014).
7. Poonam, Sharma, K., Arora, A. & Tripathi, S. K. Review of supercapacitors: Materials and devices. *Journal of Energy Storage* **21**, 801–825. ISSN: 2352152X (2019).
8. Miller, J. R. & Burke, A. Electrochemical Capacitors: Challenges and Opportunities for Real-World Applications. *The Electrochemical Society Interface* **17**, 53–57. ISSN: 1064-8208 (2008).
9. Winter, M. & Brodd, R. J. What are batteries, fuel cells, and supercapacitors? *Chemical Reviews* **104**, 4245–4269. ISSN: 00092665 (2004).

10. Becker, H. I. *US2800616 Low voltage electrolytic capacitor patent* 1957.
11. Conway, B. E. *Electrochemical Supercapacitors Scientific Fundamentals and Technological Applications* 698. ISBN: 978-1-4757-3058-6 (Springer, Boston, MA, 1999).
12. Béguin, F., Presser, V., Balducci, A. & Frackowiak, E. Carbons and electrolytes for advanced supercapacitors. *Advanced Materials* **26**, 2219–2251. ISSN: 15214095 (2014).
13. Sung, J. & Shin, C. Recent studies on supercapacitors with next-generation structures. *Micromachines* **11**, 1–25. ISSN: 2072666X (2020).
14. Trasatti, S. & Buzzanca, G. Ruthenium dioxide: A new interesting electrode material. Solid state structure and electrochemical behaviour. *Journal of Electroanalytical Chemistry* **29**, 1–5. ISSN: 00220728 (1971).
15. Okubo, M. *et al.* Nanosize effect on high-rate Li-ion intercalation in LiCoO₂ electrode. *Journal of the American Chemical Society* **129**, 7444–7452. ISSN: 00027863 (2007).
16. Brezesinski, T., Wang, J., Tolbert, S. H. & Dunn, B. Ordered mesoporous α -MoO₃ with iso-oriented nanocrystalline walls for thin-film pseudocapacitors. *Nature Materials* **9**, 146–151. ISSN: 14764660 (2010).
17. Augustyn, V. *et al.* High-rate electrochemical energy storage through Li + intercalation pseudocapacitance. *Nature Materials* **12**, 518–522. ISSN: 14764660 (2013).
18. Xia, Y. *et al.* Thickness-independent capacitance of vertically aligned liquid-crystalline MXenes. *Nature* **557**, 409–412. ISSN: 14764687 (2018).
19. Aricò, A. S., Bruce, P., Scrosati, B., Tarascon, J.-M. & van Schalkwijk, W. Nanostructured materials for advanced energy conversion and storage devices. *Nature Materials* **4**, 366–377. ISSN: 1476-1122 (2005).
20. Huang, X., Qi, X., Boey, F. & Zhang, H. Graphene-based composites. *Chemical Society Reviews* **41**, 666–686. ISSN: 03060012 (2012).
21. Li, L. *et al.* High-Performance Pseudocapacitive Microsupercapacitors from Laser-Induced Graphene. *Advanced Materials* **28**, 838–845. ISSN: 15214095 (2016).

22. Wuttke, M., Liu, Z., Lu, H., Narita, A. & Müllen, K. Direct Metal-Free Chemical Vapor Deposition of Graphene Films on Insulating Substrates for Micro-Supercapacitors with High Volumetric Capacitance. *Batteries & Supercaps* **2**, 929–933. ISSN: 2566-6223 (2019).
23. Borenstein, A. *et al.* Carbon-based composite materials for supercapacitor electrodes: A review. *Journal of Materials Chemistry A* **5**, 12653–12672. ISSN: 20507496 (2017).
24. Huang, Y. *et al.* A self-healable and highly stretchable supercapacitor based on a dual crosslinked polyelectrolyte. *Nature Communications* **6**, 1–8. ISSN: 20411723 (2015).
25. Wang, L. *et al.* Flexible solid-state supercapacitor based on a metal-organic framework interwoven by electrochemically-deposited PANI. *Journal of the American Chemical Society* **137**, 4920–4923. ISSN: 15205126 (2015).
26. Song, Y. *et al.* Pushing the Cycling Stability Limit of Polypyrrole for Supercapacitors. *Advanced Functional Materials* **25**, 4626–4632. ISSN: 16163028 (2015).
27. Khosrozadeh, A., Darabi, M. A., Xing, M. & Wang, Q. Flexible Electrode Design: Fabrication of Freestanding Polyaniline-Based Composite Films for High-Performance Supercapacitors. *ACS Applied Materials and Interfaces* **8**, 11379–11389. ISSN: 19448252 (2016).
28. Zhu, M. *et al.* Highly Flexible, Freestanding Supercapacitor Electrode with Enhanced Performance Obtained by Hybridizing Polypyrrole Chains with MXene. *Advanced Energy Materials* **6**. ISSN: 16146840 (2016).
29. Augustyn, V., Simon, P. & Dunn, B. Pseudocapacitive oxide materials for high-rate electrochemical energy storage. *Energy & Environmental Science* **7**, 1597. ISSN: 1754-5692 (2014).
30. González, A., Goikolea, E., Barrena, J. A. & Mysyk, R. Review on supercapacitors: Technologies and materials. *Renewable and Sustainable Energy Reviews* **58**, 1189–1206. ISSN: 13640321 (2016).

31. Raza, W. *et al.* Recent advancements in supercapacitor technology. *Nano Energy* **52**, 441–473. ISSN: 22112855 (2018).
32. Pandolfo, A. G. & Hollenkamp, A. F. Carbon properties and their role in supercapacitors. *Journal of Power Sources* **157**, 11–27. ISSN: 03787753 (2006).
33. Wang, Y. *et al.* Recent progress in carbon-based materials for supercapacitor electrodes: a review. *Journal of Materials Science* **56**, 173–200. ISSN: 15734803 (2021).
34. Liu, C., Li, F., Lai-Peng, M. & Cheng, H. M. Advanced materials for energy storage. *Advanced Materials* **22**, 28–62. ISSN: 09359648 (2010).
35. Sevilla, M. & Mokaya, R. Energy storage applications of activated carbons: Supercapacitors and hydrogen storage. *Energy and Environmental Science* **7**, 1250–1280. ISSN: 17545706 (2014).
36. Jurewicz, K. *et al.* Capacitance properties of ordered porous carbon materials prepared by a templating procedure. *Journal of Physics and Chemistry of Solids* **65**, 287–293. ISSN: 00223697 (2004).
37. Portet, C., Taberna, P. L., Simon, P. & Laberty-Robert, C. Modification of Al current collector surface by sol-gel deposit for carbon-carbon supercapacitor applications. *Electrochimica Acta* **49**, 905–912. ISSN: 00134686 (2004).
38. Fernández, J. A. *et al.* Performance of mesoporous carbons derived from poly(vinyl alcohol) in electrochemical capacitors. *Journal of Power Sources* **175**, 675–679. ISSN: 03787753 (2008).
39. Wang, R. *et al.* Hydrothermal synthesis of nanostructured graphene / polyaniline composites as high-capacitance electrode materials for supercapacitors. *Scientific Reports* **7**, 1–9. ISSN: 20452322 (2017).
40. Zhang, W. *et al.* A perylenetetra-carboxylic dianhydride and aniline-assembled supramolecular nanomaterial with multi-color electrochemiluminescence for a highly sensitive label-free immunoassay. *Journal of Materials Chemistry B* **8**, 3676–3682. ISSN: 20507518 (2020).

41. Zhi, M., Xiang, C., Li, J., Li, M. & Wu, N. Nanostructured carbon-metal oxide composite electrodes for supercapacitors: A review. *Nanoscale* **5**, 72–88. ISSN: 20403364 (2013).
42. Dubey, R. & Guruviah, V. Review of carbon-based electrode materials for supercapacitor energy storage. *Ionics* **25**, 1419–1445. ISSN: 18620760 (2019).
43. Yoon, B. J. *et al.* Electrical properties of electrical double layer capacitors with integrated carbon nanotube electrodes. *Chemical Physics Letters* **388**, 170–174. ISSN: 00092614 (2004).
44. Wen, S., Jung, M., Joo, O. S. & il Mho, S. EDLC characteristics with high specific capacitance of the CNT electrodes grown on nanoporous alumina templates. *Current Applied Physics* **6**, 1012–1015. ISSN: 15671-739 (2006).
45. Xu, B. *et al.* Competitive effect of KOH activation on the electrochemical performances of carbon nanotubes for EDLC: Balance between porosity and conductivity. *Electrochimica Acta* **53**, 7730–7735. ISSN: 00134686 (2008).
46. Shah, R., Zhang, X. & Talapatra, S. Electrochemical double layer capacitor electrodes using aligned carbon nanotubes grown directly on metals. *Nanotechnology* **20**. ISSN: 09574484 (2009).
47. Geim, A. K. & Novoselov, K. S. The rise of graphene. *Nature Materials* **6**, 183–191. ISSN: 1476-1122 (2007).
48. Huang, Y., Liang, J. & Chen, Y. An overview of the applications of graphene-based materials in supercapacitors. *Small* **8**, 1805–1834. ISSN: 16136810 (2012).
49. Brownson, D. A., Kampouris, D. K. & Banks, C. E. An overview of graphene in energy production and storage applications. *Journal of Power Sources* **196**, 4873–4885. ISSN: 03787753 (2011).
50. Pumera, M. Graphene-based nanomaterials for energy storage. *Energy and Environmental Science* **4**, 668–674. ISSN: 17545692 (2011).

51. Dreyer, D. R., Park, S., Bielawski, C. W. & Ruoff, R. S. The chemistry of graphene oxide. *Chem. Soc. Rev.* **39**, 228–240. ISSN: 0306-0012 (2010).
52. Ghany, N. A., Elsherif, S. A. & Handal, H. T. Revolution of Graphene for different applications: State-of-the-art. *Surfaces and Interfaces* **9**, 93–106. ISSN: 24680230 (2017).
53. Kumar, N. A. & Baek, J.-B. Doped graphene supercapacitors. *Nanotechnology* **26**, 492001. ISSN: 0957-4484 (2015).
54. Bi, Z. *et al.* Biomass-derived porous carbon materials with different dimensions for supercapacitor electrodes: a review. *Journal of Materials Chemistry A* **7**, 16028–16045. ISSN: 2050-7488 (2019).
55. Liu, L., Zhao, H. & Lei, Y. Advances on three-dimensional electrodes for micro-supercapacitors: A mini-review. *InfoMat* **1**, 74–84. ISSN: 2567-3165 (2019).
56. Kumar, D., Banerjee, A., Patil, S. & Shukla, A. K. A 1 V supercapacitor device with nanostructured graphene oxide/polyaniline composite materials. *Bulletin of Materials Science* **38**, 1507–1517. ISSN: 09737669 (2015).
57. Suematsu, S., Oura, Y., Tsujimoto, H., Kanno, H. & Naoi, K. Conducting polymer films of cross-linked structure and their QCM analysis. *Electrochimica Acta* **45**, 3813–3821. ISSN: 00134686 (2000).
58. Snook, G. A. & Chen, G. Z. The measurement of specific capacitances of conducting polymers using the quartz crystal microbalance. *Journal of Electroanalytical Chemistry* **612**, 140–146. ISSN: 15726657 (2008).
59. Zhao, D. D., Bao, S. J., Zhou, W. J. & Li, H. L. Preparation of hexagonal nanoporous nickel hydroxide film and its application for electrochemical capacitor. *Electrochemistry Communications* **9**, 869–874. ISSN: 13882481 (2007).
60. Sun, Y., Wu, Q. & Shi, G. Graphene based new energy materials. *Energy and Environmental Science* **4**, 1113–1132. ISSN: 17545692 (2011).

61. Fan, X., Phebus, B. D., Li, L. & Chen, S. Graphene-Based Composites for Supercapacitor Electrodes. *Science of Advanced Materials* **7**, 1916–1944. ISSN: 19472935 (2015).
62. Rolison, D. R. *et al.* Multifunctional 3D nanoarchitectures for energy storage and conversion. *Chem. Soc. Rev.* **38**, 226–252. ISSN: 0306-0012 (2009).
63. Chen, Y.-L. *et al.* Zinc Oxide/Reduced Graphene Oxide Composites and Electrochemical Capacitance Enhanced by Homogeneous Incorporation of Reduced Graphene Oxide Sheets in Zinc Oxide Matrix. *The Journal of Physical Chemistry C* **115**, 2563–2571. ISSN: 1932-7447 (2011).
64. Ho, M. Y. *et al.* A review of metal oxide composite electrode materials for electrochemical capacitors. *Nano* **9**, 1–25. ISSN: 17932920 (2014).
65. Chen, T. & Dai, L. Flexible supercapacitors based on carbon nanomaterials. *Journal of Materials Chemistry A* **2**, 10756–10775. ISSN: 20507496 (2014).
66. Kumar, R. *et al.* Microwave-assisted synthesis of void-induced graphene-wrapped nickel oxide hybrids for supercapacitor applications. *RSC Advances* **6**, 26612–26620. ISSN: 2046-2069 (2016).
67. Low, W. H., Khiew, P. S., Lim, S. S., Siong, C. W. & Ezeigwe, E. R. Recent development of mixed transition metal oxide and graphene/mixed transition metal oxide based hybrid nanostructures for advanced supercapacitors. *Journal of Alloys and Compounds* **775**, 1324–1356. ISSN: 09258388 (2019).
68. Tabassum, H. *et al.* Recent advances in confining metal-based nanoparticles into carbon nanotubes for electrochemical energy conversion and storage devices. *Energy & Environmental Science* **12**, 2924–2956. ISSN: 1754-5692 (2019).
69. Lokhande, P. E., Chavan, U. S. & Pandey, A. *Materials and Fabrication Methods for Electrochemical Supercapacitors: Overview* **1**, 155–186. ISBN: 0123456789 (Springer Singapore, 2020).

70. Gao, W. *et al.* Direct laser writing of micro-supercapacitors on hydrated graphite oxide films. *Nature Nanotechnology* **6**, 496–500. ISSN: 1748-3387 (2011).
71. Shen, D. *et al.* Scalable High-Performance Ultraminiature Graphene Micro-Supercapacitors by a Hybrid Technique Combining Direct Writing and Controllable Microdroplet Transfer. *ACS Applied Materials & Interfaces* **10**, 5404–5412. ISSN: 1944-8244 (2018).
72. You, R. *et al.* Laser Fabrication of Graphene-Based Flexible Electronics. *Advanced Materials* **1901981**, 1–22. ISSN: 0935-9648 (2019).
73. Fu, X.-Y. *et al.* Direct laser writing of flexible planar supercapacitors based on GO and black phosphorus quantum dot nanocomposites. *Nanoscale* **11**, 9133–9140. ISSN: 2040-3364 (2019).
74. Trusovas, R. *et al.* Recent Advances in Laser Utilization in the Chemical Modification of Graphene Oxide and Its Applications. *Advanced Optical Materials* **4**, 37–65. ISSN: 2195-1071 (2016).
75. Bäuerle, D. *Laser Processing and Chemistry* ISBN: 978-3-642-17612-8 (Springer Berlin Heidelberg, Berlin, Heidelberg, 2011).
76. Kumar, R. *et al.* Laser-assisted synthesis, reduction and micro-patterning of graphene: Recent progress and applications. *Coordination Chemistry Reviews* **342**, 34–79. ISSN: 00108545 (2017).
77. Smirnov, V. A. *et al.* Photoreduction of graphite oxide. *High Energy Chemistry* **45**, 57–61. ISSN: 00181439 (2011).
78. Fu, X.-Y. *et al.* Laser fabrication of graphene-based supercapacitors. *Photonics Research* **8**, 577. ISSN: 2327-9125 (2020).
79. El-Kady, M. F. & Kaner, R. B. Scalable fabrication of high-power graphene micro-supercapacitors for flexible and on-chip energy storage. *Nature Communications* **4**, 1475. ISSN: 2041-1723 (2013).
80. Tran, T. X. *et al.* Laser-Induced Reduction of Graphene Oxide by Intensity-Modulated Line Beam for Supercapacitor Applications. *ACS Applied Materials and Interfaces* **10**, 39777–39784. ISSN: 19448252 (2018).

81. Oh, J.-S. *et al.* Laser-Assisted Simultaneous Patterning and Transferring of Graphene. *The Journal of Physical Chemistry C* **117**, 663–668. ISSN: 1932-7447 (2013).
82. Van Ngo, T., Moussa, M., Tung, T. T., Coghlan, C. & Losic, D. Hybridization of MOFs and graphene: A new strategy for the synthesis of porous 3D carbon composites for high performing supercapacitors. *Electrochimica Acta* **329**, 135104. ISSN: 00134686 (2020).
83. Hwang, J. Y. *et al.* Direct preparation and processing of graphene/RuO₂ nanocomposite electrodes for high-performance capacitive energy storage. *Nano Energy* **18**, 57–70. ISSN: 22112855 (2015).
84. Chen, Y. *et al.* Enhanced electrochemical performance of laser scribed graphene films decorated with manganese dioxide nanoparticles. *Journal of Materials Science: Materials in Electronics* **27**, 2564–2573. ISSN: 1573482X (2016).
85. Yang, S., Li, Y., Sun, J. & Cao, B. Laser induced oxygen-deficient TiO₂/graphene hybrid for high-performance supercapacitor. *Journal of Power Sources* **431**, 220–225. ISSN: 03787753 (2019).
86. Ibrahim, Y. O. *et al.* Laser-induced anchoring of WO₃ nanoparticles on reduced graphene oxide sheets for photocatalytic water decontamination and energy storage. *Ceramics International* **46**, 444–451. ISSN: 02728842 (2020).
87. Ye, R., James, D. K. & Tour, J. M. Laser-Induced Graphene: From Discovery to Translation. *Advanced Materials* **31**, 1803621. ISSN: 0935-9648 (2019).
88. Eason, R. *Pulsed Laser Deposition of Thin Films: Applications-Led Growth of Functional Materials* (ed Eason, R.) ISBN: 9780470052129 (John Wiley and Sons, Inc., Hoboken, NJ, USA, 2006).
89. Lowndes, D. H., Geohegan, D. B., Puretzky, A. A., Norton, D. P. & Rouleau, C. M. Synthesis of novel thin-film materials by pulsed laser deposition. *Science* **273**, 898–903. ISSN: 00368075 (1996).

90. Fujioka, H. in *Handbook of Crystal Growth: Thin Films and Epitaxy: Second Edition* Second Edi, 365–397 (Elsevier B.V., 2015). ISBN: 97804446-33057.
91. Miotello, A & Ossi, P. M. *Laser-Surface Interactions for New Materials Production* (eds Miotello, A. & Ossi, P. M.) 374. ISBN: 978-3-642-03306-3 (Springer Berlin Heidelberg, Berlin, Heidelberg, 2010).
92. McGill, R. A., Chirsey, D. B. & Pique, A. *Fabrication of Conductive/non-conductive Nanocomposites by Laser Evaporation* 2003.
93. Chrisey, D. B. *et al.* Laser Deposition of Polymer and Biomaterial Films. *Chemical Reviews* **103**, 553–576. ISSN: 0009-2665 (2003).
94. Ossi, P. M. *Advances in the Application of Lasers in Materials Science* (ed Ossi, P. M.) ISBN: 978-3-319-96844-5 (Springer International Publishing, Cham, 2018).
95. Piqué, A. *et al.* Laser processing of polymer thin for chemical sensor applications. *Surface and Coatings Technology* **163-164**, 293–299. ISSN: 02578972 (2003).
96. Fitz-Gerald, J. M., Jennings, G., Johnson, R. & Fraser, C. L. Matrix assisted pulsed laser deposition of light emitting polymer thin films. *Applied Physics A: Materials Science and Processing* **80**, 1109–1113. ISSN: 09478396 (2005).
97. Caricato, A. P., Luches, A., Leggieri, G., Martino, M. & Rella, R. Matrix-assisted pulsed laser deposition of polymer and nanoparticle films. *Vacuum* **86**, 661–666. ISSN: 0042207X (2012).
98. Guo, Y. *et al.* Ultrastable nanostructured polymer glasses. *Nature Materials* **11**, 337–343. ISSN: 1476-1122 (2012).
99. György, E., Pérez del Pino, A., Sauthier, G. & Figueras, A. Biomolecular papain thin films grown by matrix assisted and conventional pulsed laser deposition: A comparative study. *Journal of Applied Physics* **106**, 114702. ISSN: 0021-8979 (2009).

100. György, E., Pérez del Pino, A., Roqueta, J., Sánchez, C. & Oliva, A. G. Processing and immobilization of chondroitin-4-sulphate by UV laser radiation. *Colloids and Surfaces B: Biointerfaces* **104**, 169–173. ISSN: 092-77765 (2013).
101. Caricato, A. P. *et al.* MAPLE deposition and characterization of SnO₂ colloidal nanoparticle thin films. *Journal of Physics D: Applied Physics* **42**, 095105. ISSN: 0022-3727 (2009).
102. György, E. *et al.* Synthesis and laser immobilization onto solid substrates of CdSe/ZnS core-shell quantum dots. *Journal of Physical Chemistry C* **115**, 15210–15216. ISSN: 19327455 (2011).
103. Hunter, C. N., Check, M. H., Bultman, J. E. & Voevodin, A. A. Development of matrix-assisted pulsed laser evaporation (MAPLE) for deposition of disperse films of carbon nanoparticles and gold/nanoparticle composite films. *Surface and Coatings Technology* **203**, 300–306. ISSN: 02578972 (2008).
104. Pérez Del Pino, Á., György, E., Cabana, L., Ballesteros, B. & Tobias, G. Deposition of functionalized single wall carbon nanotubes through matrix assisted pulsed laser evaporation. *Carbon* **50**, 4450–4458. ISSN: 00086223 (2012).
105. György, E. *et al.* Effect of laser radiation on multi-wall carbon nanotubes: Study of shell structure and immobilization process. *Journal of Nanoparticle Research* **15**. ISSN: 1572896X (2013).
106. Cesaria, M. *et al.* Matrix-assisted pulsed laser evaporation deposition of Pd nanoparticles: The role of solvent. *Science of Advanced Materials* **7**, 2388–2400. ISSN: 19472943 (2015).
107. Ajnsztajn, A. *et al.* Transparent MXene-Polymer Supercapacitive Film Deposited Using RIR-MAPLE. *Crystals* **10**, 152. ISSN: 2073-4352 (2020).

108. O'Malley, S. M., Tomko, J., Pérez del Pino, Á., Logofatu, C. & György, E. Resonant infrared and ultraviolet matrix-assisted pulsed laser evaporation of titanium oxide/graphene oxide composites: A comparative study. *Journal of Physical Chemistry C* **118**, 27911–27919. ISSN: 19327455 (2014).
109. Pérez del Pino, Á., György, E., Logofatu, C. & Duta, A. Study of the deposition of graphene oxide by matrix-assisted pulsed laser evaporation. *Journal of Physics D: Applied Physics* **46**, 1–8. ISSN: 00223727 (2013).
110. Kulkarni, S. K. *Nanotechnology: Principles and Practices* Third Edit. ISBN: 978-3-319-09170-9 (Springer International Publishing, Cham, 2015).
111. Goldstein, J. I. *et al. Scanning Electron Microscopy and X-Ray Microanalysis* Fourth, VII –XIV. ISBN: 978-1-4939-6674-5. arXiv: arXiv : 1011 . 1669v3 (Springer New York, New York, NY, 2018).
112. Ayache, J., Beaunier, L., Boumendil, J., Ehret, G. & Laub, D. *Sample Preparation Handbook for Transmission Electron Microscopy* ISBN: 978-0-387-98181-9 (Springer New York, New York, NY, 2010).
113. Zuo, J. M. & Spence, J. C. *Advanced Transmission Electron Microscopy* ISBN: 978-1-4939-6605-9 (Springer New York, New York, NY, 2017).
114. Williams, D. B. & Carter, C. B. *Transmission Electron Microscopes* ISBN: 9780387765006 (2009).
115. Als-Nielsen, J. & McMorrow, D. in *Elements of Modern X-ray Physics* 1–28 (Wiley, 2011). ISBN: 9780470973950.
116. Kučerka, N., Nieh, M.-P. & Katsaras, J. in *Advances in Planar Lipid Bilayers and Liposomes* 1st ed. C, 201–235 (Elsevier Inc., 2010).
117. Wu, Z. & Xing, X. in *Synchrotron Radiation Applications* 225–285 (World Scientific, 2018). ISBN: 9789813227675.
118. Renaud, G., Lazzari, R. & Leroy, F. Probing surface and interface morphology with Grazing Incidence Small Angle X-Ray Scattering. *Surface Science Reports* **64**, 255–380. ISSN: 01675729 (2009).

119. Li, T., Senesi, A. J. & Lee, B. Small Angle X-ray Scattering for Nanoparticle Research. *Chemical Reviews* **116**, 11128–11180. ISSN: 15206890 (2016).
120. Roe, R.-J. *Methods of X-ray and Neutron Scattering in Polymer Science* 331. ISBN: 9780195113211 (Oxford University Press, New York, 2000).
121. Burian, M., Meisenbichler, C., Naumenko, D. & Amenitsch, H. SAXS-DOG : open software for real-time azimuthal integration of 2D scattering images. *Journal of Applied Crystallography* **55**, 677–685. arXiv: 2007.02022 (2022).
122. Amenitsch, H *et al.* First performance assessment of the small-angle X-ray scattering beamline at ELETTRA. *Journal of Synchrotron Radiation* **5**, 506–508. ISSN: 0909-0495 (1998).
123. Moulder, J. F., Stickle, W. F., Sobol, P. E. & Bomben, K. D. *Handbook of X-ray Photoelectron Spectroscopy* 261. ISBN: 9780962702624 (Perkin-Elmer Corporation, 1992).
124. Andrade, J. D. in *Surface and Interfacial Aspects of Biomedical Polymers* 105–195 (Springer US, Boston, MA, 1985).
125. Stevie, F. A. & Donley, C. L. Introduction to x-ray photoelectron spectroscopy. *Journal of Vacuum Science & Technology A* **38**, 063204. ISSN: 0734-2101 (2020).
126. Griffiths, P. R. & de Haseth, J. A. *Fourier Transform Infrared Spectrometry* Second, 529. ISBN: 9780471194040 (John Wiley and Sons, Inc., New Jersey, 2007).
127. Leong, S. S., Ng, W. M., Lim, J. & Yeap, S. P. *Handbook of Materials Characterization* (ed Sharma, S. K.) 77–111. ISBN: 978-3-319-92954-5 (Springer International Publishing, Cham, 2018).
128. Pohlmann, S., Ramirez-Castro, C. & Balducci, A. The Influence of Conductive Salt Ion Selection on EDLC Electrolyte Characteristics and Carbon-Electrolyte Interaction. *Journal of The Electrochemical Society* **162**, A5020–A5030. ISSN: 0013-4651 (2015).

129. Bard, A. J. & Faulkner, L. R. *Electrochemical Methods Fundamentals and Applications* 2nd ed., 864. ISBN: 9780471043720 (John Wiley and Sons, Inc., 2000).
130. Zhang, S. & Pan, N. Supercapacitors Performance Evaluation. *Advanced Energy Materials* **5**, 1401401. ISSN: 16146832 (2015).
131. Lasia, A. *Electrochemical Impedance Spectroscopy and its Applications* ISBN: 978-1-4614-8932-0 (Springer New York, New York, NY, 2014).
132. Dupont, M. F. & Donne, S. W. A Step Potential Electrochemical Spectroscopy Analysis of Electrochemical Capacitor Electrode Performance. *Electrochimica Acta* **167**, 268–277. ISSN: 00134686 (2015).
133. Forghani, M. & Donne, S. W. Method Comparison for Deconvoluting Capacitive and Pseudo-Capacitive Contributions to Electrochemical Capacitor Electrode Behavior. *Journal of The Electrochemical Society* **165**, A664–A673. ISSN: 0013-4651 (2018).
134. Dupont, M. F. & Donne, S. W. Separating Faradaic and Non-Faradaic Charge Storage Contributions in Activated Carbon Electrochemical Capacitors Using Electrochemical Methods: I. Step Potential Electrochemical Spectroscopy. *Journal of The Electrochemical Society* **162**, A1246–A1254. ISSN: 0013-4651 (2015).
135. Queraltó, A. *et al.* Ultrafast Epitaxial Growth Kinetics in Functional Oxide Thin Films Grown by Pulsed Laser Annealing of Chemical Solutions. *Chemistry of Materials* **28**, 6136–6145. ISSN: 15205002 (2016).
136. Wan, Z. *et al.* Laser-Reduced Graphene: Synthesis, Properties, and Applications. *Advanced Materials Technologies* **3**, 1–19. ISSN: 2365709X (2018).
137. Vogel, A. & Venugopalan, V. Mechanisms of pulsed laser ablation of biological tissues. *Chemical Reviews* **103**, 577–644. ISSN: 00092665 (2003).

138. Pérez del Pino, Á., György, E., Cabana, L., Ballesteros, B. & Tobias, G. Ultraviolet pulsed laser irradiation of multi-walled carbon nanotubes in nitrogen atmosphere. *Journal of Applied Physics* **115**, 093501. ISSN: 0021-8979 (2014).
139. Sawatzky, G. A. & Allen, J. W. Magnitude and origin of the band gap in NiO. *Physical Review Letters* **53**, 2339–2342. ISSN: 00319007 (1984).
140. Dean, J. A. & Lange, N. A. *Lange's handbook of chemistry* (McGraw-Hill, New York, 1999).
141. Pérez del Pino, Á. *et al.* Reactive laser synthesis of nitrogen-doped hybrid graphene-based electrodes for energy storage. *Journal of Materials Chemistry A* **6**, 16074–16086. ISSN: 2050-7488 (2018).
142. Powell, R. J. & Spicer, W. E. Optical Properties of NiO and CoO. *Physical Review B* **2**, 2182–2193. ISSN: 0556-2805 (1970).
143. Seetawan, T., Vora-ud, A. & Wattanasarn, H. Theoretical Calculations and Analysis Modeling. **1**, 1–5 (2012).
144. Steiner, M. A. & Fitz-Gerald, J. M. Dynamics of the inverse MAPLE nanoparticle deposition process. *Applied Physics A* **119**, 629–638. ISSN: 0947-8396 (2015).
145. Pérez del Pino, A., György, E., Logofatu, C., Puigmartí-Luis, J. & Gao, W. Laser-induced chemical transformation of graphene oxide–iron oxide nanoparticles composites deposited on polymer substrates. *Carbon* **93**, 373–383. ISSN: 00086223 (2015).
146. Chmiola, J., Celine Largeot, P. L. T., Simon, P. & Gogotsi, Y. Monolithic carbide-derived carbon films for micro-supercapacitors. *Science (New York, N.Y.)* **328**, 480–483. ISSN: 00368075 (2010).
147. Meher, S. K., Justin, P. & Ranga Rao, G. Nanoscale morphology dependent pseudocapacitance of NiO: Influence of intercalating anions during synthesis. *Nanoscale* **3**, 683–692. ISSN: 20403364 (2011).
148. Wang, B., Chen, J. S., Wang, Z., Madhavi, S. & Lou, X. W. Green synthesis of nio nanobelts with exceptional pseudo-capacitive properties. *Advanced Energy Materials* **2**, 1188–1192. ISSN: 16146832 (2012).

149. Zhang, G., Yu, L., Hoster, H. E. & Lou, X. W. Synthesis of one-dimensional hierarchical NiO hollow nanostructures with enhanced supercapacitive performance. *Nanoscale* **5**, 877–881. ISSN: 20403364 (2013).
150. Cheng, G., Yan, Y. & Chen, R. From Ni-based nanoprecursors to NiO nanostructures: Morphology - controlled synthesis and structure - dependent electrochemical behavior. *New Journal of Chemistry* **39**, 676–682. ISSN: 13699261 (2015).
151. Wang, Y., Song, Y. & Xia, Y. Electrochemical capacitors: mechanism, materials, systems, characterization and applications. *Chemical Society reviews* **45**, 5925–5950. ISSN: 1460-4744 (2016).
152. Zhang, L., Peng, X.-M., Damu, G. L. V., Geng, R.-X. & Zhou, C.-H. Comprehensive Review in Current Developments of Imidazole-Based Medicinal Chemistry. *Medicinal Research Reviews* **34**, 340–437. ISSN: 01986325 (2014).
153. Pérez del Pino, A. *et al.* Synthesis of graphene-based photocatalysts for water splitting by laser-induced doping with ionic liquids. *Carbon* **130**, 48–58. ISSN: 00086223 (2018).
154. Vishwakarma, R. *et al.* Structure of nitrogen-doped graphene synthesized by combination of imidazole and melamine solid precursors. *Materials Letters* **177**, 89–93. ISSN: 0167577X (2016).
155. Liu, D., Tao, L., Yan, D., Zou, Y. & Wang, S. Recent Advances on Non-precious Metal Porous Carbon-based Electrocatalysts for Oxygen Reduction Reaction. *ChemElectroChem* **5**, 1775–1785. ISSN: 21960-216 (2018).
156. Wang, Y. *et al.* 3D Carbon Electrocatalysts In Situ Constructed by Defect-Rich Nanosheets and Polyhedrons from NaCl-Sealed Zeolitic Imidazolate Frameworks. *Advanced Functional Materials* **28**. ISSN: 161-63028 (2018).

157. Queraltó, A. *et al.* MAPLE synthesis of reduced graphene oxide/silver nanocomposite electrodes: Influence of target composition and gas ambience. *Journal of Alloys and Compounds* **726**, 1003–1013. ISSN: 09258388 (2017).
158. Lin, Z., Waller, G., Liu, Y., Liu, M. & Wong, C. P. Facile synthesis of nitrogen-doped graphene via pyrolysis of graphene oxide and urea, and its electrocatalytic activity toward the oxygen-reduction reaction. *Advanced Energy Materials* **2**, 884–888. ISSN: 16146832 (2012).
159. Gogotsi, Y. & Penner, R. M. Energy Storage in Nanomaterials - Capacitive, Pseudocapacitive, or Battery-like? *ACS Nano* **12**, 2081–2083. ISSN: 1936086X (2018).
160. Liu, J. *et al.* Advanced Energy Storage Devices: Basic Principles, Analytical Methods, and Rational Materials Design. *Advanced Science* **5**, 1–19. ISSN: 21983844 (2018).
161. Hsieh, C. T. & Teng, H. Influence of oxygen treatment on electric double-layer capacitance of activated carbon fabrics. *Carbon* **40**, 667–674. ISSN: 00086223 (2002).
162. Hulicova-Jurcakova, D., Seredych, M., Lu, G. Q. & Bandosz, T. J. Combined effect of nitrogen- and oxygen-containing functional groups of microporous activated carbon on its electrochemical performance in supercapacitors. *Advanced Functional Materials* **19**, 438–447. ISSN: 1616301X (2009).
163. Shukla, A., Isaacs, E. D., Hamann, D. R. & Platzman, P. M. Hydrogen bonding in urea. *Physical Review B* **64**, 052101. ISSN: 0163-1829 (2001).
164. Seredych, M., Hulicova-Jurcakova, D., Lu, G. Q. & Bandosz, T. J. Surface functional groups of carbons and the effects of their chemical character, density and accessibility to ions on electrochemical performance. *Carbon* **46**, 1475–1488. ISSN: 00086223 (2008).
165. Su, F. *et al.* Nitrogen-containing microporous carbon nanospheres with improved capacitive properties. *Energy and Environmental Science* **4**, 717–724. ISSN: 17545692 (2011).

166. Jones, A. O., Leech, C. K., McIntyre, G. J., Wilson, C. C. & Thomas, L. H. Engineering short, strong hydrogen bonds in urea di-carboxylic acid complexes. *CrystEngComm* **16**, 8177–8184. ISSN: 14668033 (2014).
167. Amiruddin, R. & Santhosh Kumar, M. C. Role of p-NiO electron blocking layers in fabrication of (P-N):ZnO/Al:ZnO UV photodiodes. *Current Applied Physics* **16**, 1052–1061. ISSN: 15671739 (2016).
168. Bardé, F., Taberna, P., Tarascon, J. & Palacín, M. Evidence for electronic and ionic limitations at the origin of the second voltage plateau in nickel electrodes, as deduced from impedance spectroscopy measurements. *Journal of Power Sources* **179**, 830–836. ISSN: 03787753 (2008).
169. Choi, B. G., Yang, M., Hong, W. H., Choi, J. W. & Huh, Y. S. 3D macroporous graphene frameworks for supercapacitors with high energy and power densities. *ACS Nano* **6**, 4020–4028. ISSN: 19360851 (2012).
170. Kim, T., Jung, G., Yoo, S., Suh, K. S. & Ruoff, R. S. Activated graphene-based carbons as supercapacitor electrodes with macro- and mesopores. *ACS Nano* **7**, 6899–6905. ISSN: 19360851 (2013).
171. Pech, D. *et al.* Ultrahigh-power micrometre-sized supercapacitors based on onion-like carbon. *Nature Nanotechnology* **5**, 651–654. ISSN: 17483395 (2010).
172. Frackowiak, E., Lota, G., Machnikowski, J., Vix-Guterl, C. & Béguin, F. Optimisation of supercapacitors using carbons with controlled nanotexture and nitrogen content. *Electrochimica Acta* **51**, 2209–2214. ISSN: 00134686 (2006).
173. Wang, D. W., Li, F., Liu, M., Lu, G. Q. & Cheng, H. M. 3D aperiodic hierarchical porous graphitic carbon material for high-rate electrochemical capacitive energy storage. *Angewandte Chemie - International Edition* **47**, 373–376. ISSN: 14337851 (2008).
174. Zhao, X., Hayner, C. M., Kung, M. C. & Kung, H. H. Flexible holey graphene paper electrodes with enhanced rate capability for energy storage applications. *ACS Nano* **5**, 8739–8749. ISSN: 19360851 (2011).

175. Yu, D. & Dai, L. Self-assembled graphene/carbon nanotube hybrid films for supercapacitors. *Journal of Physical Chemistry Letters* **1**, 467–470. ISSN: 19487185 (2010).
176. Cheng, Q. *et al.* Graphene and carbon nanotube composite electrodes for supercapacitors with ultra-high energy density. *Physical Chemistry Chemical Physics* **13**, 17615–17624. ISSN: 14639076 (2011).
177. Kandasamy, S. K. & Kandasamy, K. Recent Advances in Electrochemical Performances of Graphene Composite (Graphene-Polyaniline / Polypyrrole / Activated Carbon / Carbon Nanotube) Electrode Materials for Supercapacitor: A Review. *Journal of Inorganic and Organometallic Polymers and Materials* **28**, 559–584. ISSN: 15741451 (2018).
178. Díez, N. *et al.* Highly packed graphene-CNT films as electrodes for aqueous supercapacitors with high volumetric performance. *Journal of Materials Chemistry A* **6**, 3667–3673. ISSN: 20507496 (2018).
179. Glatter, O. in *Scattering Methods and their Application in Colloid and Interface Science* Elsevier I, 1–18 (2018). ISBN: 978-0-12-813580-8.
180. Santos, C. *et al.* Pore structure and electrochemical properties of CNT-based electrodes studied by: In situ small/wide angle X-ray scattering. *Journal of Materials Chemistry A* **7**, 5305–5314. ISSN: 20507496 (2019).
181. Sandoval, S. *et al.* Tuning the nature of nitrogen atoms in N-containing reduced graphene oxide. *Carbon* **96**, 594–602. ISSN: 00086223 (2016).
182. Queraltó, A. *et al.* Reduced graphene oxide/iron oxide nanohybrid flexible electrodes grown by laser-based technique for energy storage applications. *Ceramics International* **44**, 20409–20416. ISSN: 02728-842 (2018).
183. Gomathi, A., Reshma, S. & Rao, C. N. A simple urea-based route to ternary metal oxynitride nanoparticles. *Journal of Solid State Chemistry* **182**, 72–76. ISSN: 00224596 (2009).

184. Lin, Z. *et al.* Facile preparation of nitrogen-doped graphene as a metal-free catalyst for oxygen reduction reaction. *Physical Chemistry Chemical Physics* **14**, 3381–3387. ISSN: 14639076 (2012).
185. Guo, H. L., Su, P., Kang, X. & Ning, S. K. Synthesis and characterization of nitrogen-doped graphene hydrogels by hydrothermal route with urea as reducing-doping agents. *Journal of Materials Chemistry A* **1**, 2248–2255. ISSN: 20507496 (2013).
186. Yeh, T. F., Chen, S. J., Yeh, C. S. & Teng, H. Tuning the electronic structure of graphite oxide through ammonia treatment for photocatalytic generation of H₂ and O₂ from water splitting. *Journal of Physical Chemistry C* **117**, 6516–6524. ISSN: 19327447 (2013).
187. Wang, Z. *et al.* Synthesis of nitrogen-doped graphene by chemical vapour deposition using melamine as the sole solid source of carbon and nitrogen. *Journal of Materials Chemistry C* **2**, 7396–7401. ISSN: 20507526 (2014).
188. Biesinger, M. C., Payne, B. P., Lau, L. W., Gerson, A. & Smart, R. S. C. X-ray photoelectron spectroscopic chemical state Quantification of mixed nickel metal, oxide and hydroxide systems. *Surface and Interface Analysis* **41**, 324–332. ISSN: 01422421 (2009).
189. Pérez del Pino, Á. *et al.* Laser-induced nanostructuring of vertically aligned carbon nanotubes coated with nickel oxide nanoparticles. *Journal of Materials Science* **52**, 4002–4015. ISSN: 15734803 (2017).
190. Ferrari, A. C. & Basko, D. M. Raman spectroscopy as a versatile tool for studying the properties of graphene. *Nature Nanotechnology* **8**, 235–246. ISSN: 17483395. arXiv: 1306.5856 (2013).
191. Cançado, L. G. *et al.* Quantifying defects in graphene via Raman spectroscopy at different excitation energies. *Nano Letters* **11**, 3190–3196. ISSN: 15306984. arXiv: 1105.0175 (2011).
192. Cançado, L. G. *et al.* Disentangling contributions of point and line defects in the Raman spectra of graphene-related materials. *2D Materials* **4**. ISSN: 20531583 (2017).

193. Jorio, A., Martins Ferreira, E. H., G., L., A., C. & B., R. in *Physics and Applications of Graphene - Experiments* (InTech, 2011).
194. Venezuela, P., Lazzeri, M. & Mauri, F. Theory of double-resonant Raman spectra in graphene: Intensity and line shape of defect-induced and two-phonon bands. *Physical Review B - Condensed Matter and Materials Physics* **84**, 1–25. ISSN: 10980121. arXiv: 1103.4582 (2011).
195. Eckmann, A. *et al.* Probing the nature of defects in graphene by Raman spectroscopy. *Nano Letters* **12**, 3925–3930. ISSN: 15306984 (2012).
196. Zhang, L. L. & Zhao, X. S. Carbon-based materials as supercapacitor electrodes. *Chemical Society Reviews* **38**, 2520–2531. ISSN: 03060012 (2009).
197. Yu, D., Zhang, Q. & Dai, L. Highly efficient metal-free growth of nitrogen-doped single-walled carbon nanotubes on plasma-etched substrates for oxygen reduction. *Journal of the American Chemical Society* **132**, 15127–15129. ISSN: 00027863 (2010).
198. Yang, S. *et al.* Efficient synthesis of heteroatom (N or S)-doped graphene based on ultrathin graphene oxide-porous silica sheets for oxygen reduction reactions. *Advanced Functional Materials* **22**, 3634–3640. ISSN: 1616301X (2012).
199. Lee, Y. H., Chang, K. H. & Hu, C. C. Differentiate the pseudocapacitance and double-layer capacitance contributions for nitrogen-doped reduced graphene oxide in acidic and alkaline electrolytes. *Journal of Power Sources* **227**, 300–308. ISSN: 03787753 (2013).
200. Liu, T. C., Pell, W. G., Conway, B. E. & Roberson, S. L. Behavior of molybdenum nitrides as materials for electrochemical capacitors comparison with ruthenium oxide. *Journal of the Electrochemical Society* **145**, 1882–1888. ISSN: 00134651 (1998).
201. Barsoukov, E. & Macdonald, J. R. *Impedance Spectroscopy Theory, Experiment, and Applications* ISBN: 9781119381860 (John Wiley & Sons, Inc., Hoboken, New Jersey, 2005).

202. Luo, Z. *et al.* Pyridinic N doped graphene: Synthesis, electronic structure, and electrocatalytic property. *Journal of Materials Chemistry* **21**, 8038–8044. ISSN: 09599428 (2011).
203. Sheng, Z. H. *et al.* Catalyst-free synthesis of nitrogen-doped graphene via thermal annealing graphite oxide with melamine and its excellent electrocatalysis. *ACS Nano* **5**, 4350–4358. ISSN: 19360851 (2011).
204. Wang, H., Maiyalagan, T. & Wang, X. Review on recent progress in nitrogen-doped graphene: Synthesis, characterization, and its potential applications. *ACS Catalysis* **2**, 781–794. ISSN: 21555435 (2012).
205. Wang, X. *et al.* Heteroatom-doped graphene materials: Syntheses, properties and applications. *Chemical Society Reviews* **43**, 7067–7098. ISSN: 14604744 (2014).
206. Akada, K., Terasawa, T. O., Imamura, G., Obata, S. & Saiki, K. Control of work function of graphene by plasma assisted nitrogen doping. *Applied Physics Letters* **104**, 1–5. ISSN: 00036951 (2014).
207. Guo, D. *et al.* Active sites of nitrogen-doped carbon materials for oxygen reduction reaction clarified using model catalysts. *Science* **351**, 361–365. ISSN: 0036-8075 (2016).
208. Śliwak, A., Grzyb, B., Diez, N. & Gryglewicz, G. Nitrogen-doped reduced graphene oxide as electrode material for high rate supercapacitors. *Applied Surface Science* **399**, 265–271. ISSN: 01694332 (2017).
209. Yuan, W. *et al.* The edge- and basal-plane-specific electrochemistry of a single-layer graphene sheet. *Scientific Reports* **3**, 1–7. ISSN: 20452322 (2013).
210. Zheng, F., Yang, Y. & Chen, Q. High lithium anodic performance of highly nitrogen-doped porous carbon prepared from a metal-organic framework. *Nature Communications* **5**, 1–10. ISSN: 20411723 (2014).
211. Wu, X. *et al.* Insight into high areal capacitances of low apparent surface area carbons derived from nitrogen-rich polymers. *Carbon* **94**, 560–567. ISSN: 00086223 (2015).

212. Lin, Y. C. *et al.* Structural and Chemical Dynamics of Pyridinic-Nitrogen Defects in Graphene. *Nano Letters* **15**, 7408–7413. ISSN: 15306992 (2015).
213. Tu, N. D. K. *et al.* Pyridinic-Nitrogen-Containing Carbon Cathode: Efficient Electrocatalyst for Seawater Batteries. *ACS Applied Energy Materials* **3**, 1602–1608. ISSN: 25740962 (2020).
214. Jeong, H. M. *et al.* Nitrogen-doped graphene for high-performance ultracapacitors and the importance of nitrogen-doped sites at basal planes. *Nano Letters* **11**, 2472–2477. ISSN: 15306984 (2011).
215. Padmanathan, N. & Selladurai, S. Shape controlled synthesis of CeO₂ nanostructures for high performance supercapacitor electrodes. *RSC Advances* **4**, 6527–6534. ISSN: 20462069 (2014).
216. Maheswari, N. & Muralidharan, G. Supercapacitor Behavior of Cerium Oxide Nanoparticles in Neutral Aqueous Electrolytes. *Energy and Fuels* **29**, 8246–8253. ISSN: 15205029 (2015).
217. Prasanna, K. *et al.* Highly porous CeO₂ nanostructures prepared via combustion synthesis for supercapacitor applications. *Applied Surface Science* **449**, 454–460. ISSN: 01694332 (2018).
218. Luo, Y., Yang, T., Zhao, Q. & Zhang, M. CeO₂/CNTs hybrid with high performance as electrode materials for supercapacitor. *Journal of Alloys and Compounds* **729**, 64–70. ISSN: 09258388 (2017).
219. Deng, D., Chen, N., Xiao, X., Du, S. & Wang, Y. Electrochemical performance of CeO₂ nanoparticle-decorated graphene oxide as an electrode material for supercapacitor. *Ionics* **23**, 121–129. ISSN: 18620760 (2017).
220. Goharshadi, E. K., Samiee, S. & Nancarrow, P. Fabrication of cerium oxide nanoparticles: Characterization and optical properties. *Journal of Colloid and Interface Science* **356**, 473–480. ISSN: 00219797 (2011).
221. Vasiliu, F., Pârvulescu, V. & Sârbu, C. Trivalent Ce₂O₃ and CeO_{2-x} intermediate oxides induced by laser irradiation of CeO₂ powders. *Journal of Materials Science* **29**, 2095–2101. ISSN: 15734803 (1994).

222. Ma, R., Jahurul Islam, M., Amaranatha Reddy, D. & Kim, T. K. Transformation of CeO₂ into a mixed phase CeO₂/Ce₂O₃ nanohybrid by liquid phase pulsed laser ablation for enhanced photocatalytic activity through Z-scheme pattern. *Ceramics International* **42**, 18495–18502. ISSN: 02728842 (2016).
223. Younis, A., Chu, D. & Li, S. in *Functionalized Nanomaterials* (ed Akhyar Farrukh, M.) 53–68 (IntechOpen, 2016). ISBN: 978-953-51-2856-4.
224. Debnath, S., Islam, M. R. & Khan, M. S. Optical properties of CeO₂ thin films. *Bulletin of Materials Science* **30**, 315–319. ISSN: 02504707 (2007).
225. Nelson, A. T. *et al.* An Evaluation of the Thermophysical Properties of Stoichiometric CeO₂ in Comparison to UO₂ and PuO₂. *Journal of the American Ceramic Society* **97**, 3652–3659. ISSN: 0002-7820 (2014).
226. Barth, C. *et al.* A perfectly stoichiometric and flat CeO₂ (111) surface on a bulk-like ceria film. *Scientific Reports* **6**, 2–7. ISSN: 20452322 (2016).
227. Wu, Y. *et al.* Oxygen vacancies regulated microwave absorption properties of reduced graphene oxide/multi-walled carbon nanotubes/cerium oxide ternary nanocomposite. *Journal of Alloys and Compounds* **819**, 152944. ISSN: 09258388 (2020).
228. Qiu, L., Liu, F., Zhao, L., Ma, Y. & Yao, J. Comparative XPS study of surface reduction for nanocrystalline and microcrystalline ceria powder. *Applied Surface Science* **252**, 4931–4935. ISSN: 01694332 (2006).
229. Yu, X. & Li, G. XPS study of cerium conversion coating on the anodized 2024 aluminum alloy. *Journal of Alloys and Compounds* **364**, 193–198. ISSN: 09258388 (2004).
230. Plata, J. J., Márquez, A. M. & Sanz, J. F. Electron Mobility via Polaron Hopping in Bulk Ceria: A First-Principles Study. *The Journal of Physical Chemistry C* **117**, 14502–14509. ISSN: 1932-7447 (2013).

231. Mao, X. *et al.* All-solid-state flexible microsupercapacitors based on reduced graphene oxide/multi-walled carbon nanotube composite electrodes. *Applied Surface Science* **435**, 1228–1236. ISSN: 01694332 (2018).
232. Chen, C. S., Chen, X. H., Xu, L. S., Yang, Z. & Li, W. H. Modification of multi-walled carbon nanotubes with fatty acid and their tribological properties as lubricant additive. *Carbon* **43**, 1660–1666. ISSN: 00086223 (2005).
233. Kaniyoor, A., Baby, T. T. & Ramaprabhu, S. Graphene synthesis via hydrogen induced low temperature exfoliation of graphite oxide. *Journal of Materials Chemistry* **20**, 8467–8469. ISSN: 09599428 (2010).
234. Shateri-Khalilabad, M. & Yazdanshenas, M. E. Preparation of superhydrophobic electroconductive graphene-coated cotton cellulose. *Cellulose* **20**, 963–972. ISSN: 09690239 (2013).
235. Zhao, G. *et al.* Alkylated graphene nanosheets for supercapacitor electrodes: High performance and chain length effect. *Carbon* **94**, 114–119. ISSN: 00086223 (2015).
236. Cui, X., Lv, R., Sagar, R. U. R., Liu, C. & Zhang, Z. Reduced graphene oxide/carbon nanotube hybrid film as high performance negative electrode for supercapacitor. *Electrochimica Acta* **169**, 342–350. ISSN: 00134686 (2015).
237. Singh, A. K., Sarkar, D., Karmakar, K., Mandal, K. & Khan, G. G. High-Performance Supercapacitor Electrode Based on Cobalt Oxide-Manganese Dioxide-Nickel Oxide Ternary 1D Hybrid Nanotubes. *ACS Applied Materials and Interfaces* **8**, 20786–20792. ISSN: 19448252 (2016).
238. Wang, Y. *et al.* Highly Stable Three-Dimensional Nickel-Cobalt Hydroxide Hierarchical Heterostructures Hybridized with Carbon Nanotubes for High-Performance Energy Storage Devices. *ACS Nano* **13**, 11235–11248. ISSN: 1936086X (2019).

239. Bélanger, D., Brousse, T. & Long, J. Manganese Oxides: Battery Materials Make the Leap to Electrochemical Capacitors. *The Electrochemical Society Interface* **17**, 49–52. ISSN: 1064-8208 (2008).
240. Wu, Z.-S. *et al.* High-Energy MnO₂ Nanowire/Graphene and Graphene Asymmetric Electrochemical Capacitors. *ACS Nano* **4**, 5835–5842. ISSN: 1936-0851 (2010).
241. Jia, H. *et al.* Mesostructured Carbon Nanotube-on-MnO₂ Nanosheet Composite for High-Performance Supercapacitors. *ACS Applied Materials and Interfaces* **10**, 38963–38969. ISSN: 19448252 (2018).
242. Nagamuthu, S., Vijayakumar, S. & Muralidharan, G. Synthesis of Mn₃O₄/amorphous carbon nanoparticles as electrode material for high performance supercapacitor applications. *Energy and Fuels* **27**, 3508–3515. ISSN: 08870624 (2013).
243. Lee, G. *et al.* High-performance all-solid-state flexible micro-supercapacitor arrays with layer-by-layer assembled MWNT/MnO_x nanocomposite electrodes. *Nanoscale* **6**, 9655–9664. ISSN: 20403372 (2014).
244. Chen, S. *et al.* Reduced graphene oxide/Mn₃O₄ nanocrystals hybrid fiber for flexible all-solid-state supercapacitor with excellent volumetric energy density. *Electrochimica Acta* **242**, 10–18. ISSN: 00134686 (2017).
245. Xiong, T., Lee, W. S. V., Huang, X. & Xue, J. M. Mn₃O₄/reduced graphene oxide based supercapacitor with ultra-long cycling performance. *Journal of Materials Chemistry A* **5**, 12762–12768. ISSN: 20507496 (2017).
246. Murugan, R. *et al.* Pure and Co doped CeO₂ nanostructure electrodes with enhanced electrochemical performance for energy storage applications. *Ceramics International* **43**, 10494–10501. ISSN: 02728842 (2017).
247. He, G. *et al.* Dumbbell-like ZnO nanoparticles-CeO₂ nanorods composite by one-pot hydrothermal route and their electrochemical charge storage. *Applied Surface Science* **366**, 129–138. ISSN: 01694332 (2016).

248. Liu, J. *et al.* Co₃O₄ nanowire@MnO₂ ultrathin nanosheet core/shell arrays: A new class of high-performance pseudocapacitive materials. *Advanced Materials* **23**, 2076–2081. ISSN: 09359648 (2011).
249. Sun, X., Li, Q., Lü, Y. & Mao, Y. Three-dimensional ZnO@MnO₂ core@shell nanostructures for electrochemical energy storage. *Chemical Communications* **49**, 4456–4458. ISSN: 13597345 (2013).
250. Sarkar, D., Khan, G. G., Singh, A. K. & Mandal, K. High-performance pseudocapacitor electrodes based on α -Fe₂O₃/MnO₂ core-shell nanowire heterostructure arrays. *Journal of Physical Chemistry C* **117**, 15523–15531. ISSN: 19327447 (2013).
251. Gu, Y. *et al.* Preparation and capacitance behavior of manganese oxide hollow structures with different morphologies via template-engaged redox etching. *Journal of Power Sources* **239**, 347–355. ISSN: 03787753 (2013).
252. Dong, R. *et al.* Enhanced supercapacitor performance of Mn₃O₄ nanocrystals by doping transition-metal ions. *ACS Applied Materials and Interfaces* **5**, 9508–9516. ISSN: 19448244 (2013).
253. Li, F. *et al.* Morphology and crystallinity-controlled synthesis of manganese cobalt oxide/manganese dioxides hierarchical nanostructures for high-performance supercapacitors. *Journal of Power Sources* **296**, 86–91. ISSN: 03787753 (2015).
254. Wang, G., Ma, Z., Zhang, G., Li, C. & Shao, G. Cerium-doped porous K-birnessite manganese oxides microspheres as pseudocapacitor electrode material with improved electrochemical capacitance. *Electrochimica Acta* **182**, 1070–1077. ISSN: 00134686 (2015).
255. Zhang, H. *et al.* Hierarchical porous MnO₂/CeO₂ with high performance for supercapacitor electrodes. *Chemical Engineering Journal* **286**, 139–149. ISSN: 13858947 (2016).

256. Ojha, G. P., Pant, B., Park, S. J., Park, M. & Kim, H. Y. Synthesis and characterization of reduced graphene oxide decorated with CeO₂-doped MnO₂ nanorods for supercapacitor applications. *Journal of Colloid and Interface Science* **494**, 338–344. ISSN: 10957103 (2017).
257. Rajagopal, R. & Ryu, K. S. Synthesis of La and Ce Mixed MnO₂ Nanostructure/rGO Composite for Supercapacitor Applications. *Chem-ElectroChem* **5**, 2218–2227. ISSN: 21960216 (2018).
258. Peng, R. *et al.* Construction of 0D CeO₂/2D MnO₂ heterostructure with high electrochemical performance. *Electrochimica Acta* **319**, 95–100. ISSN: 00134686 (2019).
259. Liu, C. *et al.* Ultrafine Mn₃O₄/CeO₂ nanorods grown on reduced graphene oxide sheets as high-performance supercapacitor electrodes. *Journal of Alloys and Compounds* **722**, 54–59. ISSN: 09258388 (2017).
260. Wekesa, M. & Ni, Y. Further understanding of the chemistry of manganese-induced peroxide decomposition. *Canadian Journal of Chemical Engineering* **81**, 968–972. ISSN: 00084034 (2003).
261. Banerjee, D. & Nesbitt, H. W. XPS study of reductive dissolution of birnessite by oxalate: Rates and mechanistic aspects of dissolution and redox processes. *Geochimica et Cosmochimica Acta* **63**, 3025–3038. ISSN: 00167037 (1999).
262. Zeng, Z. *et al.* On-chip interdigitated supercapacitor based on nanoporous gold/manganese oxide nanowires hybrid electrode. *Electrochimica Acta* **163**, 107–115. ISSN: 00134686 (2015).
263. Wang, X. *et al.* The insight into the role of CeO₂ in improving low-temperature catalytic performance and SO₂ tolerance of MnCoCeOx microflowers for the NH₃-SCR of NO_x. *Applied Surface Science* **510**. ISSN: 01694332 (2020).
264. He, C., Chen, Y., Guo, L., Yin, R. & Qiu, T. Catalytic ozonation of NH₄⁺-N in wastewater over composite metal oxide catalyst. *Journal of Rare Earths* **40**, 73–84. ISSN: 10020721 (2022).

265. Nesbitt, H. W. & Banerjee, D. Interpretation of XPS Mn(2p) spectra of Mn oxyhydroxides and constraints on the mechanism of MnO₂ precipitation. *American Mineralogist* **83**, 305–315. ISSN: 0003004X (1998).
266. Qi, G. & Yang, R. T. Characterization and FTIR studies of MnO x-CeO₂ catalyst for low-temperature selective catalytic reduction of NO with NH₃. *Journal of Physical Chemistry B* **108**, 15738–15747. ISSN: 15206106 (2004).
267. Gruet, D., Delobel, B., Sicsic, D., Lucas, I. T. & Vivier, V. On the electrochemical impedance response of composite insertion electrodes – Toward a better understanding of porous electrodes. *Electrochimica Acta* **295**, 787–800. ISSN: 00134686 (2019).
268. Edwards, D. A. & Hayward, R. N. Transition metal acetates. *Canadian Journal of Chemistry* **46**, 3443–3446. ISSN: 0008-4042 (1968).
269. Mohamed, M. A. & Halawy, S. A. Kinetic and mechanistic study of the non-isothermal decomposition of manganese(II) acetate tetrahydrate. *Thermochimica Acta* **242**, 173–186. ISSN: 00406031 (1994).
270. Barakat, N. A. *et al.* Preparation of nanofibers consisting of MnO/Mn₃O₄ by using the electrospinning technique: The nanofibers have two band-gap energies. *Applied Physics A: Materials Science and Processing* **95**, 769–776. ISSN: 09478396 (2009).
271. Lang, X., Hirata, A., Fujita, T. & Chen, M. Nanoporous metal/oxide hybrid electrodes for electrochemical supercapacitors. *Nature Nanotechnology* **6**, 232–236. ISSN: 17483395 (2011).
272. Yu, G. *et al.* Solution-processed graphene/MnO₂ nanostructured textiles for high-performance electrochemical capacitors. *Nano Letters* **11**, 2905–2911. ISSN: 15306984 (2011).
273. Weingarth, D., Foelske-Schmitz, A. & Kötz, R. Cycle versus voltage hold - Which is the better stability test for electrochemical double layer capacitors? *Journal of Power Sources* **225**, 84–88. ISSN: 03787753 (2013).